Numerical Modeling of Interface Dynamics and Transport Phenomena in Transport-Limited Electrolysis Processes

by

Wanida Pongsaksawad

B.S., Materials Science and Engineering
Case Western Reserve University 2001

Submitted to the Department of Materials Science and Engineering
in partial fulfillment of the requirements for the degree of

Doctor of Philosophy in Materials Science and Engineering

at the

MASSACHUSETTS INSTITUTE OF TECHNOLOGY

June 2006

Author .....
Department of Materials Science and Engineering
May 22, 2006

Certified by .....
Adam C. Powell, IV
Assistant Professor of Materials Engineering
Thesis Supervisor

Accepted by .....
Samuel M. Allen
POSCO Professor of Physical Metallurgy
Chair, Department Committee on Graduate Students

Numerical Modeling of Interface Dynamics and Transport Phenomena in Transport-Limited Electrolysis Processes

by

Wanida Pongsaksawad

Submitted to the Department of Materials Science and Engineering
on May 22, 2006, in partial fulfillment of the
requirements for the degree of
Doctor of Philosophy in Materials Science and Engineering

Abstract

Electrochemical reactions in materials and processes induce morphological instability on the cathode, which can lead to porous deposits or system failure. The growth of the protrusion is a complex phenomenon which involves chemical, electrical, and momentum driving forces in the system. Thus, it is important to understand the effect of electrochemistry in phase boundary evolution in order to optimize the performance of such processes. This thesis contributes to predicting and controlling such interface instability phenomena by developing a computational model that captures them. Successful application of the model to emerging metal extraction processes demonstrates its usefulness.

A phase field model of electrochemical interface is developed for transport-limited electrolysis with rapid charge redistribution. This new Cahn-Hillard phase field formulation includes a model electrostatic free energy term, which captures the behavior of the diffuse interface under the applied electric field, in addition to transport by free energy gradient and convection. The model agrees with published stability criterion for a solid cathode. When the electrodes and electrolyte are low-viscosity fluids, flow stabilizes the interface. A new stability criterion for metal reduction in a liquid-liquid system is derived and agrees well with the model results. Next, the phase field model is extended for a ternary system to model titanium reduction in a supported electrolyte system. The model can simulate phase boundaries migration depending on the composition of the electrolyte and also electronically mediated reactions. Finally, Solid Oxide Membrane Electrolytic Smelting with Rotating Cathode (SOMERC), an emerging technology to electrolytically reduce titanium oxide from molten salt, is investigated. In the SOMERC process, rotational flow is introduced to create shear force that is expected to stabilize the interface. Computational fluid dynamics models of rotational flow are carried out to estimate the relationship between cathode rotational speed, shear strain rate, and boundary layer thicknesses.

The phase field model presented in this thesis can be applied to any electrochemical reduction processes that are in the mass-transport controlled regime. Stability criteria and detailed morphology in two and three dimensions can be explored.

Thesis Supervisor: Adam C. Powell, IV
Title: Assistant Professor of Materials Engineering

Acknowledgments

First and foremost, I would like to express my gratitude to my thesis advisor, Professor Adam Powell, for giving me an opportunity to work on this project and guiding me through this research. His endless patience, encouragement, and optimism have leveled up the motivation in this work. I highly respect his in-depth knowledge on computational modeling and parallel computing, his commitments in teaching, as well as his language skill in giving a technical presentation in Japanese at the University of Tokyo.

I would like to acknowledge Prof. Samuel Allen and Prof. Ain Sonin for their invaluable time and supports as the thesis committee. I would also like to thank Prof. Donald Sadoway for insightful discussion on the direction of our publication in the field of electrochemistry.

Our experimental collaborators, Prof. Uday Pal and Prof. Toru Okabe, have also enforced the motivation in this modeling work. Their research groups have performed excellent experimental works on the new titanium production technologies. Especially, I would like to thank all members at Prof. Okabe's lab for their hard work and friendship during my summer visit at the University of Tokyo.

I am also greatly appreciated Powell group members: David Dussault, Dr. Bo Zhou, Dr. Albert Lok, and Jorge. Thanks to David Dussault for teaching Bo and I on finite different method during the first summer in the group. David's thesis has become my resourceful guide for this work. I would also like to thank Bo for her bright and energetic working style that gave a positive force to the group. Albert attracted more than 15 students to our office during his office hours due to his good sense of humor that came with tough problem sets. Jorge who speaks the same computer language as Prof. Powell helped teaching me many tricks on the Linux system.

I would like to acknowledge National Science Foundation for research funds during 2005-2006 (Award DMI-0457381) and the Royal thai Government for financial support of my education in the U.S.

I must acknowledge the suggestions and supports from DMSE Thai friends: Dr. Pimpa Limthongkul, Dr. Ariya Akthakul, Dr. Yot Boontongkong, Dr. Nuwong Chollacoop, Dr. Jessada Wannasin, and Panitarn (Naan) Wanakamol. Without their tremendous help and experiences, I would not have passed through the written-oral qualifying exams or survived my graduate study. The younger DMSE friends, Dr. Yutthanant Boonyongmaneerat and Puye Nonglak Meethong have shown their high potentials in research that surpass my level. The DMSE gang, Nok Samerkhae Jongthammanurak, Ae Ratchatee Techapiesarncharoenkij, Dr. Preston Li, and Dr. Albert Lok has also been supportive academically and socially from qualification exam to badminton games and several get-together dinners through out these years. Special thanks to Dr. Pimpa, P'Naan, and Nok for their true kindness and for various delicious dessert that they baked.

Furthermore, I would like to extend my appreciation to Thai Students at MIT. Everyone has made my experience at MIT a memorable one. All activities, parties, and trips have been the most enjoyable. Especially, P'Bo Jaturada Chollacoop, P'Jazz Rungrawee Wannasin, P'Yong Waty Lilaonikul, N'Jane Kalaya Kovidvisith, N'Gift Piyatida Hoisungwan have constantly given me cheerful encouragements. I am highly impressed with N'Jane Kalaya's effort on understanding this thesis by studying every page of my presentation note. I would also like to thank her for showing me several useful Photoshop tips to improve the clarity of some figures.

My Thai Scholar friends, especially Gift Aranee Techawiboonwong, Khim Siraprapa Rungpry, Por Paweena Kreunin, and Tang Napat Triroj, have been through this long journey together since the day we left Thailand for our education in the U.S. Thanks all for sharing the up and down moments.

The greatest inspiration of all comes from my family. This thesis is dedicated to them. To Papa, who often reminds me to have healthy food and tells me homemade recipe, but I always miss those food he has cooked at home. To Mama, who gives me strength to go on. To auntie (Yeekow), who believes in me and gives our family endless supports. To Roj, Ju, and Yui, who are my most genuine life-long friends.

Contents

List of Figures

List of Tables

Chapter 1

Introduction

1.1 Morphological Instability in Electrochemical Reactions

During electrochemical processes, the cathode deposit commonly propagates as a rough surface which leads to formation of electrochemical dendrite. For instance, battery technology [1, 2, 3], copper electrodeposition [4], and iron oxide reduction under applied electric field [5] develop dendritic deposits on the cathodes. Representative electrochemical dendrite topologies are illustrated in Figure 1-1. Such dendrite propagation is induced by Mullins-Sekerka instability [6]. Near the cathode, electrons are consumed by ions in the reduction reaction as the deposit is formed, while at the dissolving anode, electrons and ions are generated from the oxidation reaction. Consequently, there exists an ion depleted layer near the cathode and ion rich layer near the anode. The reaction rate is controlled by electron transfer, mass transport, or mixed, depending on temperature. For high-temperature electrolysis processes, the electrochemical reaction is in the mass transport-limited regime, thus, mass transport plays an important role in the growth phenomena.

There are three mass-transport mechanisms in the electrolyte: diffusion, convection, and electromigration. Diffusion is the mass transport driven by local chemical potential gradient. In the presence of the cation depleted layer near the cathode,

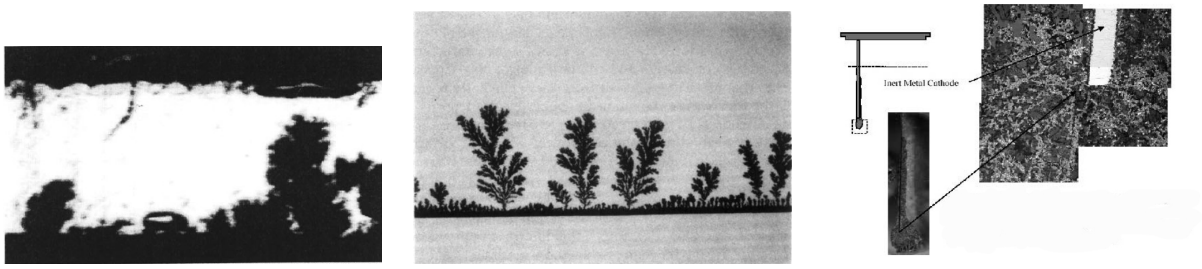

(a) (b) (c)

Figure 1-1: (a) Dendrite formation on lithium and polymer electrolyte interface [3]. (b) Dendrite structure observed in electrodeposition of copper on glass substrate [4]. (c) Metal streamers on the cathode during electric field enhanced iron reduction process [5].

more ions are drawn to the surface partly by the concentration gradient. Convection is mass transport by hydrodynamic flow, which can be induced by forced convection (stirring by magnetic field, impellers other motion) or free convection (due to temperature or density differences). Electromigration is ion transport due to electrical potential gradient. At the tip of a dendrite, the electric field is stronger, thereby causing faster ion migration and higher deposition rate. This effect is dominant under a high current density for an unsupported binary electrolyte [7]. In a supporting electrolyte with presence of spectator ions [8, 9, 10], this becomes less significant, but diffusion concentrates deposition at dendrite tips.

In order to maximize the performance of these materials and systems, one must understand the role of electrochemistry in the migration of phase boundaries. The complexity of interface shape and topology changes and coupled chemical and electrical driving forces makes these systems very difficult to comprehend. Toward this end, it is necessary to be able to model coupling of electrochemical reactions with fluid flow to understand interface morphology development in general.

1.2 Numerical Modeling of Electrochemical Interface

As mentioned in the previous section, the cathodic reduction of ions to metal exhibits a Mullins-Sekerka instability due to an ion-depleted layer at the cathode/electrolyte interface. Any perturbation on the cathode surface leads to the formation of solid dendrites or liquid streamers, affecting the process efficiency as well as resulting in a rough surface or porous deposit.

The governing equations which describe this process are well understood, such as the Poisson equation for electrical potential, charge conservation, ion diffusion driven by electric and chemical potential gradients, and the Navier-Stokes equations. Many investigators have used these equations in the limit of small perturbations in order to study the stability of cathodic interfaces [9, 10]. Haataja *et al.* classify previous works on linear stability analysis into unsupported [11, 12] and fully supported electrolytes [8, 9, 13], then extend this analysis to arbitrary supporting electrolytes [10]. These analyses demonstrate that the interface perturbation growth is faster with increasing deposition rates, increasing spectator ion concentrations, increasing perturbation wavelengths and amplitudes, and decreasing ohmic resistances due to charge transfer. Qualitatively, these predictions correlate well with experimental observation.

The shape and topology of the interface, however, cannot be captured by linear stability analysis. In practice, an electrochemical process involves complex geometries and interacts with other physical phenomena such as fluid flow, solidification, stress state, etc. For these reasons, more general numerical models are required to investigate interface growth mechanisms. Methods which explicitly track the interface work sufficiently well under some circumstances [14] but break down when the interface topology changes. One particle-based numerical method that can accommodate interface topology changes is the kinetic Monte Carlo method. Martin has investigated the morphological stability of ion-conducting oxides and halides by kinetic Monte Carlo simulation [15]. Pricer *et al.* also use this method to model a copper electrodeposition process [16]. The limitation of kinetic Monte Carlo model

is that it is mainly based on phenomenological parameters in the probability density function, which must be carefully fitted to experimental data.

On the continuum side, one mean-field approach used to study electrochemical interfaces is the level set method, which tracks interface propagation over time based on the curvature-dependent speed [17]. This method has been used to model the roughness evolution during superconformal electrodeposition with additives and catalysts in the electrolyte [18, 19]. With the level set method, the interface is considered to be sharp and is tracked and evolved based on its physical interactions, some of which relate to curvature. This method requires that the interface dynamics be understood a priori, making it difficult to extend to complex systems with many components.

Thermodynamically, the interface advances such that its free energy is minimized. One particular model for tracking an interface based on its free energy is the phase field model. The phase field approach uses one or more field variables to determine the phase of material at any location and time. The governing equation, derived from a thermodynamic statement of free energy or entropy, is coupled to the relevant transport equations of the system. Therefore, this model takes into account important physical phenomena during electrochemical interface shape evolution. It is also easily extended to complex multi-component systems, and even interactions driven by stress state, as long as the thermodynamic free energy function, surface energy, and diffusivity data are available. All phases are represented by one set of variables; thus, this method can easily handle a complex interface. Guyer *et al.* have developed a general formulation for phase field modeling of electrodeposition and electrodissolution [20]. Although their approach includes the detail of charge distribution at the interface, it is currently limited in two ways: it requires discretization of the electrochemical double layer, limiting its use to nanometer-scale systems, and it is a numerically challenging technique, such that it has to date only been solved in one dimension.

When limited by mass transfer, the effect of charge transfer resistance at the interfacial double layer is negligible, removing the need to discretize the double layer, and permitting simulation of larger systems. Dussault and Powell [21] have reported

two-dimensional results from phase field calculation of interfacial dynamics in an electrolytic steel refining process in which transport-limited reactions occur. In addition, the model can be coupled with fluid dynamics using an extension of Jacqmin's phase field formulation of two-phase incompressible Navier-Stokes flows [22]. The simulation results can thus capture anode and cathode perturbation responses to an electric field for a solid or liquid system. However, the previous model requires further development in order to capture the detailed morphology. This thesis starts with the modification of the previous model and extends it to a multi-component system.

1.3 Plan of Study and Thesis Overview

The main purpose of this thesis is to model the cathode/electrolyte interface dynamics for multi-component system coupled with fluid dynamics under transport-limited conditions. The phase field method is used to simulate the diffuse interface shape and topology evolution in the high-temperature electrochemical reaction with unsupported or supported electrolyte. We apply our models to the processes invented by our experimental collaborators [5, 23, 24]. The structure of the thesis is described below:

Chapter 2 presents the interface dynamics study to capture the shape and topological evolution in the Electric-Field Enhanced Smelting and Refining Process [5]. A simple phase field model of a two-component system (unsupported electrolyte) is extended from Dussault [25] for solid-solid and liquid-liquid interfaces. In each case, stability analyses are performed, and presented as dimensionless plots of stability criteria.

Chapter 3 includes an extension of the phase field model to a ternary system with supporting electrolyte. A model Ti-Mg-F system is used to represent the electrolytic smelting of titanium in a mixture of MgF_2 and TiF_2 molten salt. Solid-solid interface evolution is investigated along with the stability criteria as a function of molten salt composition. In addition, the model is applied to the Subhalide Reduction Process [23] to demonstrate the titanium formation by magnesiothermic reduction and

electronically mediated reaction in the Ti-Mg-Cl ternary system.

Chapter 4 introduces a new titanium process called Solid Oxide Membrane Electrolytic with Rotating Cathode (SOMERC) [24]. This study focuses on macroscopic flow in the SOMERC process. Computational fluid dynamics models for flow under vertical and horizontal rotation are carried out. These models incorporate momentum and ion diffusion in the molten salt. Mass transfer boundary layer thicknesses and shear strain rates are plotted as a function of rotation speed. The results from flow models are prepared for a phase field model of a solid-liquid interface system with cross-flow to discuss the possibility of dendrite suppression by shear force.

Chapter 5 summarizes the contributions of this thesis. The limitations of these models and future expansions are also described.

Chapter 2

Cathode Interface Dynamics in a Binary System

The phase field formulation for coupled fluid flow, diffusion, interfacial energy, electromigration, and electrochemical reactions was first developed by Dussault [25]. Building on that, this chapter presents two- and three-dimensional results for cathode shape and topology evolution under conditions of transport-limited electrolysis and rapid charge redistribution, including results for both all-solid and all-liquid binary systems (unsupported electrolyte). Stability analyses for the diffuse interface systems are carried out for each case and compared to linear stability theory for a sharp interface.

2.1 Introduction

The Electric-Field-Enhanced Smelting and Refining (EFESR) process [5] motivates the phase field model in this chapter. The goal is to develop a fundamental understanding of the system under transport-limited conditions. The EFESR process operating in a steelmaking vessel accelerates the reaction between iron oxide in the slag and carbon in the steel by applying an electric field across the slag layer as illustrated in Figure 2-1a. Molten slag contains FeO_x and other oxides such as CaO, SiO_2, etc. The products of this process are pure iron at the cathode, purified iron at

the anode, and CO bubbles at the anode/electrolyte interface. In the experiment, the iron cathode forms streamers (liquid dendrite) as shown in Figure 1-1c. The growth is accelerated by the applied field, resulting in high deposition rate. Nevertheless, long streamers either short circuit when they reach anode or breakup into droplet and slowdown the reaction rate.

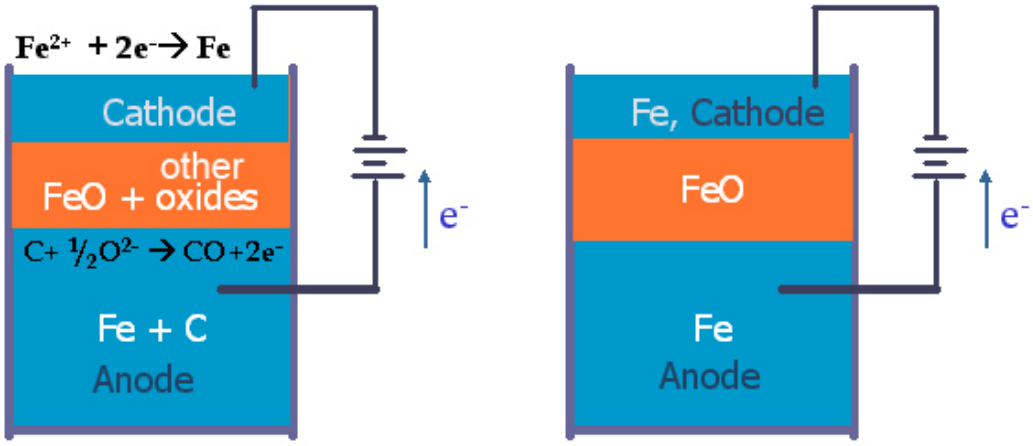

(a) EFESR process (b) Simplified diagram for simulation

Figure 2-1: Schematic drawing of the Electric Field Enhanced Smelting and Refining Process.

For simplicity, we assume that the slag only contains FeO and both metal electrodes are pure iron. Therefore, a simplified three layer structure in the binary system (Fe-FeO-Fe) is used (see Figure 2-1b).

Previous results display interface motion under applied electric field, non-complex perturbation growth of the cathode, the decay of the anode, and the effect of surface tension driven flow [26]. The contours showing the growth of the cathode are illustrated in Figure 2-2. Nonetheless, the simulations did not capture the streamer development observed in experiments. The new formulations and more systematic solver tools developed in this chapter improve on the earlier model by illustrating complex interface topology evolution of the phenomena in the physical EFESR model.

The differences between each model are listed in Table 2.1.

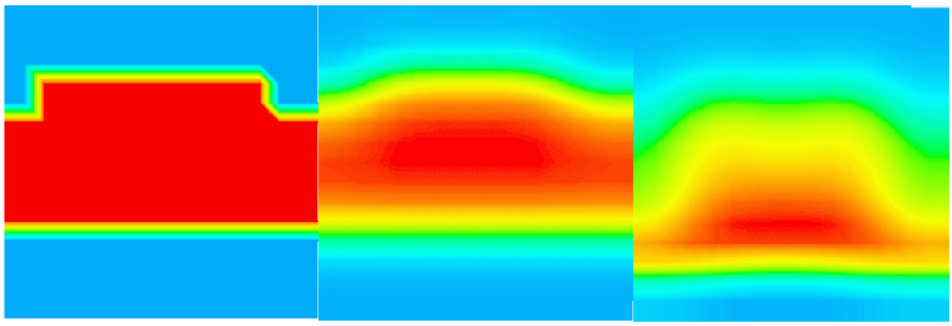

Figure 2-2: Cathode interface growth from the previous Fe-FeO-Fe simulation with 16×16 grid resolution [26]. The model shows a thick diffuse interface.

Table 2.1: Modifications from previous model.

Dussault's model	Present model
• Standard free energy functional	• Electrostatic term in the free energy functional
• Velocity-pressure form of Navier-Stokes equations	• Velocity-vorticity form of Navier-Stokes equations
• Strong variation of interface thickness due to insufficient resolution	• Better solvers produce results at higher resolution
• Simple square perturbation initial condition	• Sinusoidal initial condition for linear stability analysis

Each modification is discussed in the following section.

2.2 Phase Field Formulation for Binary System

Thermodynamics

The major improvement on Dussault's formulation is to take into account the electrostatic contribution in the free energy term. In this study, the proposed free energy functional $\mathcal{F}$, includes terms for homogeneous chemical free energy $\Psi(C)$, gradient energy $|\nabla C|^2$, and electrostatic energy $z_i F c_i \Phi$ as presented in the model of Guyer *et*

al. [20, 27]:

$$\mathcal{F} = \int \left[\beta\Psi(C) + \left(\frac{\alpha}{2}\right) |\nabla C|^2 + \sum z_i F c_i \Phi \right] \, dV, \tag{2.1}$$

where α and β are phase field parameters which can be adjusted to provide reasonable interface thickness ($\varepsilon \sim \sqrt{\alpha/\beta}$) and true interfacial energy ($\gamma \sim \sqrt{\alpha\beta}$). The gradient penalty term is added to create a diffuse interface. The electrostatic term includes the sum of electrostatic energy of each ionic species, where z_i represents the number of electron charges per ion, c_i is the molar concentration of each species, and Φ is the electrical potential.

For a two-phase system, the homogeneous free energy (Ψ) has two minima at the equilibrium. A simplified homogeneous free energy expression can be represented by a polynomial function of dimensionless composition C:

$$\Psi = C^2(1-C)^2. \tag{2.2}$$

The two minima are at $C = 0$, here representing the electrolyte, and $C = 1$, representing the metal; thus, the metal/electrolyte interface has C varying from 0 to 1. To write Equation (2.1) in terms of C, the molar concentrations c_i can be replaced by:

$$c_{Fe} = \frac{\rho X_{Fe}}{X_{Fe}M_{Fe} + X_O M_O} \tag{2.3}$$

$$c_O = \frac{\rho X_O}{X_{Fe}M_{Fe} + X_O M_O}, \tag{2.4}$$

where X_i is the mole fraction: $X_{Fe} = 0.5(1+C)$ and $X_O = 0.5(1-C)$, ρ is the overall density, and M_i is the molar mass. For simplicity, total molar density $\rho/M = \rho/(X_{Fe}M_{Fe} + X_O M_O)$ is assumed to be uniform in this model, as is approximately the case in the Fe-FeO system. Then the free energy functional becomes:

$$\mathcal{F} = \int \left[\beta\Psi(C) + \left(\frac{\alpha}{2}\right) |\nabla C|^2 + z_{Fe} F \frac{\rho}{M}(1+C)\Phi + z_O F \frac{\rho}{M}(1-C)\Phi \right] dV. \tag{2.5}$$

The variable z_i depends on C across the interface; therefore, the chemical potential can be derived by fitting the charge neutrality condition as the electrolyte approaches the metal phase. In the electrolyte, $z_{Fe} = +2 = z$ and $z_O = -2 = -z$, and the above equation is reduced to

$$\mathcal{F} = \int \left[\beta\Psi(C) + \left(\frac{\alpha}{2}\right) |\nabla C|^2 + \frac{2zF\rho}{M}\Phi C \right] dV. \tag{2.6}$$

The total electrochemical potential of iron is the variational derivative of the free energy functional:

$$\mu_{Fe} = \frac{\delta\mathcal{F}}{\delta C} = -\alpha\nabla^2 C + \beta\Psi'(C) + \frac{2zF\rho}{M}\Phi. \tag{2.7}$$

In the metal, z_{Fe} is zero. Assuming oxygen exhibits uniform charge ($z_O = -2$) everywhere and negligible solubility in metallic iron, charge neutrality requires that the iron charge be given by

$$z_{Fe}(C) = \frac{z(1-C)}{(1+C)}. \tag{2.8}$$

Replacing z in Equation 2.7 with $z_{Fe}(C)$ makes it applicable to both electrolyte and metal. Then let μ'_{Fe} be the chemical potential of Fe without the electrostatic term ($\mu'_{Fe} = -\alpha\nabla^2 C + \beta\Psi'(C)$), the overall electrochemical chemical potential is:

$$\mu_{Fe} = -\alpha\nabla^2 C + \beta\Psi'(C) + \frac{2zF\rho}{M}\frac{(1-C)}{(1+C)}\Phi\cdot = \mu'_{Fe} + \frac{2zF\rho}{M}\frac{(1-C)}{(1+C)}\Phi\cdot \tag{2.9}$$

This electrochemical potential function is used to describe the flux of iron in the system.

2.2.1 Governing Equations for the Model

Conservation of Species

The transport equation for conservation of iron in a fluid with velocity field $\overrightarrow{U}$ is

$$\frac{DC}{Dt} = \frac{\partial C}{\partial t} + \nabla \cdot (\overrightarrow{U} C) = -\nabla \cdot (\overrightarrow{J}_{Fe}), \tag{2.10}$$

where $\overrightarrow{J}_{Fe}$ is the molar flux of iron and $\frac{D}{Dt}$ represents the substantial derivative in the frame of reference moving with velocity $\vec{U}$. In this system, the molar flux includes a diffusional term driven by the gradient in chemical potential $\nabla \mu'_{Fe}$ and a migration term driven by the gradient in electrical potential $\nabla \Phi$

$$\overrightarrow{J}_{Fe} = -\kappa_{Fe} \nabla \mu_{Fe} = -\kappa_{Fe} \left(\nabla \mu'_{Fe} + 2zF \frac{(1-C)}{(1+C)} \nabla (\frac{\rho}{M} \Phi) \right), \tag{2.11}$$

where κ_{Fe} is the iron mobility. For iron and ferrous oxide, the molar density are roughly the same, so this term can be taken outside the gradient. Therefore the complete conservation equation is given by,

$$\frac{DC}{Dt} = \nabla \cdot \left(\kappa_{Fe} \nabla \mu'_{Fe} + 2z\kappa_{Fe} F \frac{\rho}{M} \frac{(1-C)}{(1+C)} \nabla (\Phi) \right). \tag{2.12}$$

Mobility κ_{Fe}, is assumed to be uniform and related to diffusivity D_{Fe} according to:

$$D_{Fe} = \frac{\kappa_{Fe} \beta \left(\frac{d^2 \Psi}{dC^2} \right)}{(c_{metal} - c_{slag})}. \tag{2.13}$$

Equation (2.12) can be compared to that of Dussault's model [21] which is expressed as:

$$\frac{DC}{Dt} = \nabla \cdot (\kappa_{Fe} \nabla \mu'_{Fe}) + \nabla \cdot \left(\frac{\sigma_{Fe}(C)}{z_{Fe}(C) F (\rho/M)} \nabla \Phi \right). \tag{2.14}$$

such that σ_i is ionic conductivity defined as

$$\sigma_i = \sigma_{Fe}(C) = 2z\kappa_{Fe} F^2 (\frac{\rho}{M})^2 \frac{(1-C)}{(1+C)}. \tag{2.15}$$

The conservation of species equation (See Equation (2.14) is normalized by defining $\tilde{t} = \frac{t}{\lambda^2/\overline{D}} = \frac{t}{\lambda^2/\overline{\kappa}_{Fe}\beta<\Psi''>}$, where $\langle \Psi'' \rangle$ is the characteristic value of Ψ'', $\tilde{\kappa}_{Fe} = 1$, $\tilde{\mu} = \frac{\mu}{\beta}$, $\tilde{L} = \frac{L}{\lambda}$, $\tilde{\sigma}_{Fe} = \frac{\sigma_{Fe}}{2z\overline{\kappa}_{Fe} F^2 (\rho/M)^2}$, and $\tilde{\Phi} = \frac{\Phi - \Phi_{cathode}}{\Phi_{anode} - \Phi_{cathode}} = \frac{\Phi - \Phi_{cathode}}{\triangle \Phi}$. The dimensionless equation is expressed as:

$$\frac{DC}{D\widetilde{t}} = \frac{1}{<\Psi''>}\widetilde{\nabla}\cdot(\widetilde{\nabla}\widetilde{\mu}_{Fe}) + Pe\frac{L}{\lambda}\widetilde{\nabla}\cdot\left(\widetilde{\sigma}_{Fe}\frac{1-C}{1+C}\widetilde{\nabla}\widetilde{\Phi}\right), \tag{2.16}$$

where

$$Pe = \frac{\overline{\sigma}_{Fe}\overline{\Phi}\lambda}{zF(\rho/M)L\overline{D}} = \frac{\overline{\Phi}zF(\rho/M)\varepsilon\lambda}{2\sqrt{18}\cdot 3.1\gamma L}. \tag{2.17}$$

This Peclet number represents the advance of the interface due to metal reduction compared to the smoothing of the interface due to diffusion. It is usually expressed as $\frac{U_{int}\lambda}{\overline{D}}$, where U_{int} is the interface velocity due to plating.

Conservation of Charge

The equation for conservation charge can be expressed by

$$\frac{D\rho_f}{Dt} = -\nabla\cdot(\overrightarrow{J}_{Fe}z_{Fe}(C)F\frac{\rho}{M} + \overrightarrow{J}_{O}z_{O}F\frac{\rho}{M} - \sigma_e(C)\nabla\Phi), \tag{2.18}$$

where ρ_f is the charge density $[C/m^3]$ and $\sigma_e(C)$ is the electronic conductivity. $\sigma_e(C)$ is estimated by linear interpolation between $\sigma_{e,metal}$ and $\sigma_{e,slag} \cong 0$. Then from the definition of mole-weighted velocity, oxygen and iron fluxes are equal and opposite, and $\overrightarrow{J}_{O} = -\overrightarrow{J}_{Fe}$. Thus, the conservation of charge equation reduces to:

$$\frac{D\rho_f}{Dt} = -\nabla\cdot(\overrightarrow{J}_{Fe}(z_{Fe}(C) - z_O)F\frac{\rho}{M} - \sigma_e(C)\nabla\Phi). \tag{2.19}$$

Defining $\widetilde{z}(C) = z_{Fe}(C) - z_O$ with $z_{Fe}(C)$ given by Equation (2.8) and substituting $\overrightarrow{J}_{Fe}$ with Equation (2.11), the above equation becomes

$$\begin{aligned}\frac{\partial\rho_f}{\partial t} + \overrightarrow{U}\cdot\nabla\rho_f \;=\; & \nabla\cdot(\widetilde{z}(C)F\tfrac{\rho}{M}\kappa_{Fe}\nabla\mu'_{Fe}) + \\ & \nabla\cdot(2z\kappa_{Fe}F^2(\tfrac{\rho}{M})^2\tfrac{(1-C)}{(1+C)}\nabla(\Phi)) + \\ & \nabla\cdot(\sigma_e(C)\nabla\Phi).\end{aligned} \tag{2.20}$$

Based on the scaling analysis done by Dussault [25], Equation 2.20 can be simplified by the following assumptions:

- Current driven by diffusion is negligible because chemical potential is zero for this binary system.

- Transport of charge by electric field is more dominant compared to that by convection.

- Charge buildup timescale is rapid compared to the diffusion time. Thus the conservation of charge equation is effectively at steady state.

The conditions described above are referred to as rapid charge redistribution: steady state charge transport and no convection. Finally, the conservation of charge equation becomes

$$0 = \nabla \cdot (2z\kappa_{Fe}F^2(\frac{\rho}{M})^2\frac{(1-C)}{(1+C)}\nabla(\Phi)) + \nabla \cdot (\sigma_e(C)\nabla\Phi), \tag{2.21}$$

where $\sigma_e(C)$ is expressed as $(3C^2 - 2C^3)\sigma_{e_0}$ and σ_{e_0} is the electronic conductivity of iron. The value of σ_e is zero in the slag, unity in the metal, and dependent on C in the diffuse interface. Next, we can define an effective electrical conductivity the sum of the ionic and electronic conductivity as

$$\sigma_{eff} = 2z\kappa_{Fe}F^2(\frac{\rho}{M})^2\frac{(1-C)}{(1+C)} + \sigma_e(C). \tag{2.22}$$

Thus, the conservation of charge equation is simplified to

$$0 = \nabla \cdot (\sigma_{eff}(C)\nabla\Phi). \tag{2.23}$$

Note that the charge redistribution in an aqueous system is a diffusive process, in which the simplification derived above may not be valid, particularly when the electric field fluctuates rapidly. In the ternary system, the concentration boundary layer is large and the transport of charge due to chemical potential gradient must be taken into account.

The charge balance equation is normalized by defining $\tilde{\sigma}_{Fe} = \frac{\sigma_{Fe}}{\widetilde{z}(C)2z\kappa_{Fe}F^2(\frac{\rho}{M})^2}$ and $\tilde{\sigma}_e = \frac{\sigma_e}{\sigma_{e,slag}}$. The dimensionless equation becomes:

$$0 = \widetilde{\nabla} \cdot \left[\left(\frac{(1-C)}{(1+C)} + \tilde{\sigma}_e(C) \right) \widetilde{\nabla} \widetilde{\Phi} \right]. \tag{2.24}$$

Fluid Dynamics for Liquid-Liquid System

In the EFESR process, the reaction occurs between liquid phases, thus it is necessary to include the effect of fluid flow. The Navier-Stokes equations describe conservation of mass and momentum in a fluid system. The velocity-pressure form of Navier-Stokes equation is difficult to solve since it requires staggered mesh in order get accurate results. One way to avoid this problem is by converting it to a velocity-vorticity form. Thus, the phase field model in the present work is coupled with the velocity-vorticity Navier-Stokes equations. The dimensionless velocity-vorticity formulation using the same time and length scales as the previous section can be expressed as:

$$\begin{aligned} \widetilde{\nabla}^2 \widetilde{u} + \frac{\partial \widetilde{\omega}}{\partial \widetilde{y}} &= 0 \\ \widetilde{\nabla}^2 \widetilde{v} - \frac{\partial \widetilde{\omega}}{\partial \widetilde{x}} &= 0 \\ \frac{\partial \widetilde{\omega}}{\partial \widetilde{t}} + \overrightarrow{u} \cdot \widetilde{\nabla} \widetilde{\omega} &= Sc \widetilde{\nabla}^2 \widetilde{\omega} - N \widetilde{\nabla} \times (C \widetilde{\nabla} \widetilde{\mu}) \end{aligned} \quad , \tag{2.25}$$

where $\widetilde{u}$ and $\widetilde{v}$ are dimensionless velocity components in the x and y directions, $\widetilde{\omega}$ is the dimensionless vorticity, Sc is the Schmidt number $\left(\frac{\eta}{\rho D}\right)$, η is viscosity, and N is the force parameter $\left(\frac{\gamma}{\rho u^2 \varepsilon}\right)$. The vorticity transport equation includes the curl of the surface tension forcing term $(-C \widetilde{\nabla} \widetilde{\mu})$ given by Jacqmin [22], which describes driving force due to interfacial curvature. We assume uniform fluid properties (viscosity and density), and neglect gravitational force.

2.2.2 Simulation Setup and Parameters

The 2-D and 3-D formulations were discretized using finite difference method. Time derivatives were modeled using the Crank-Nicholson semi-implicit timestepping algorithm in RheoPlast, the free software developed by Powell research group [28]. More details are included in Appendix B.

The initial condition is a three layer system as described earlier, with $C = 0$ in the

iron oxide slag and $C = 1$ in the iron metal. Periodic boundary conditions are applied in the x direction. In the y direction, symmetry boundary conditions are applied for C and $\overrightarrow{U} - \omega$, whereas electrical potential Φ is fixed at zero at the upper boundary (cathode) and one at the lower boundary (anode). Table 2.2 displays physical and numerical parameters used in the binary system simulations. A smaller value of σ_{e_0} than that of iron is used to improve convergence, while still keeping it relatively much greater than that of the slag.

Table 2.2: Physical and Simulation Parameters

Parameters	Physical	Simulation
$\frac{\rho}{M}$	1.31×10^5 mol/m^3	1.31×10^5 mol/m^3
$\sigma_{e,slag}$	12.0 Ω^{-1} m^{-1}	12.0 Ω^{-1} m^{-1}
σ_{e_0}	10^5 Ω^{-1} m^{-1}	10^3 Ω^{-1} m^{-1}

2.3 Binary Solid-Solid Interface Motion Results

2.3.1 Effects of Electrical Potential and Surface Tension on the Small Perturbations on the Electrodes (2D)

To study the interface shape and topology changes due to electrical potential relative to the interfacial energy, a system without convection is investigated first. This system is regarded as a solid-solid case, that is, with solid electrode and electrolyte. One small box perturbation is introduced to each electrode interface (the cathode on the top and anode on the bottom). Some random fluctuations ($\sim$0.001) are also added through out the domain. With constant applied electrical potential, a low surface energy interface develops dendrites at the cathode which may short circuit the system or break into droplets, as commonly observed in the experiments [5]. Under such a condition, electromigration is dominant. At a larger surface energy, the cathode interface is stable. In this case, diffusion overcomes electromigration, stabilizing the cathode interface. The perturbation on the anode always disappears

because that interface is unconditionally stable. These results with low and high interfacial energy are shown in Figure 2-3a and 2-3b, respectively.

A preliminary result of two-dimensional evolution of emerging dendrite in electrodeposition simulated by the Electrochemical Mean-Field Kinetic lattice model [29] is shown here for comparison in Figure 2-4. That model employed unrealistic simulation parameters due to lengthscale limitation. In the real systems, the lengthscale of the aggregation is in an order of micron, but the lattice model lengthscale is in angstrom, Å. However, our model neglects the charge double layer effect and allows us to simulate at much larger scales up to millimeters. As shown in the comparison of topology evolution, our phase field model can also capture the interface in more detail.

2.3.2 Cathode Instability in Three Dimensions

A three-dimensional simulation without fluid flow under unstable conditions is carried out. Contour surfaces describing the diffuse interface are shown in Figure 2-5. The initial perturbation is a cubic shape on the electrode surfaces. Like the two-dimensional cases, the perturbation on the cathode grows into a long streamer. On the anode, the perturbation dissolves and then the interface rapidly moves downward. When the streamer arm reaches the anode, a short circuit occurs; that short circuit later breaks due to a Rayleigh instability. Finally, the whole cathode interface breaks down. These three-dimensional results can qualitatively capture important features in the growth of an electrochemical dendrite.

2.3.3 Stability Analysis Results

According to the sharp interface model by Barkey *et al.* [30], stability of a sinusoidal perturbation on electrochemical interface depends on the electric field, the fraction of limiting current, and the surface energy. The interface is stable when the sum of electric field and the fraction of limiting current is less than the surface energy term.

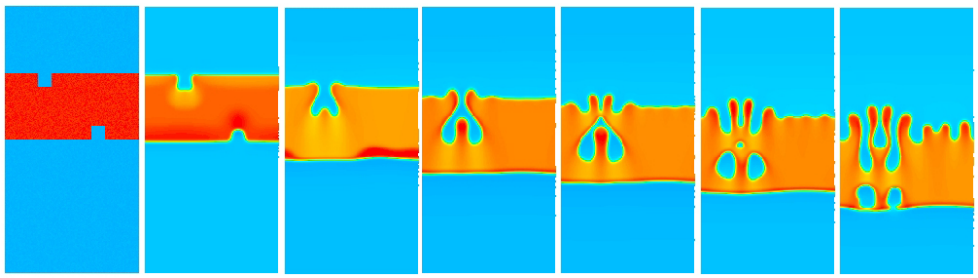

(a) Cathode shape evolution under high electric field on a 150×300 grid: The perturbed cathode interface is unstable.

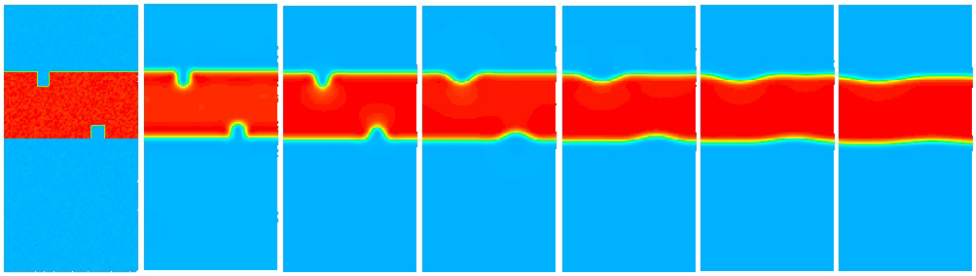

(b) Cathode shape evolution under high surface tension on an 80×160 grid: The perturbed cathode interface is stable.

Figure 2-3: Interface dynamics without convection. The left most contour represents the initial condition with three layer structure: metal/electrolyte/metal. Higher interfacial energy stabilized the interface.

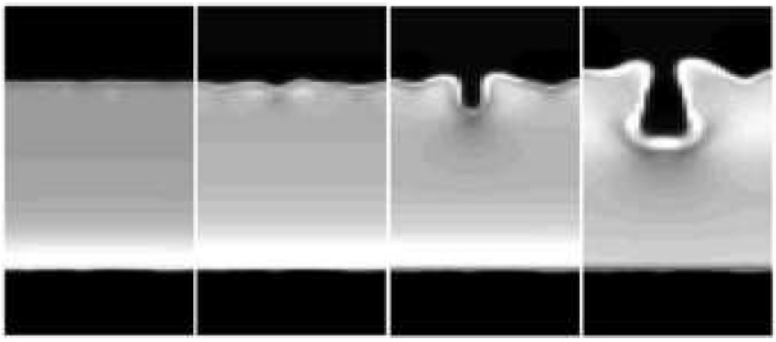

Figure 2-4: Two-dimensional simulation results based on Electrochemical Mean-Field Kinetic Equations by Bernard *et al.* [29] The cell is re-centered during the simulation. Gray indicates ion depleted region. White indicates the charge double layer.

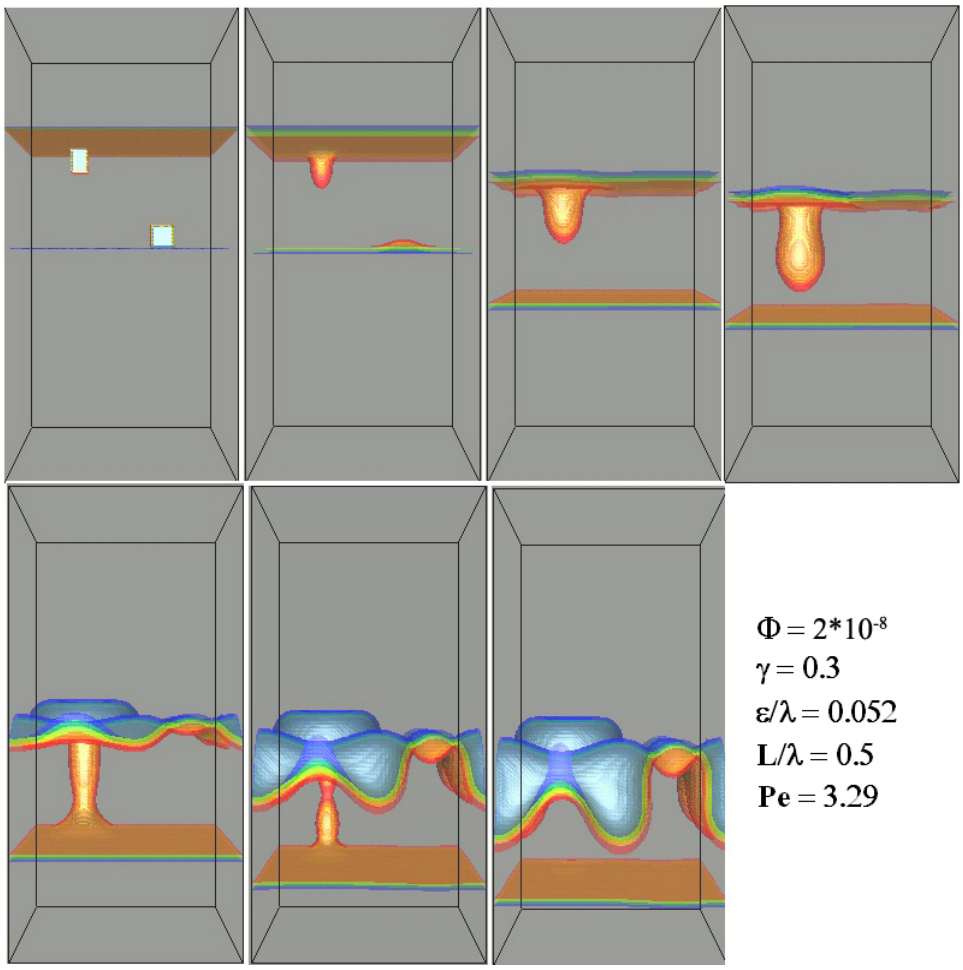

Figure 2-5: Three dimensional results of the cathode topology under electric field with no convection on the domain size of 60x120x60. The bump on the cathode grows and shorts circuits when it reaches the anode.

$$\frac{i_A}{\sigma_e} + \frac{RT\frac{i}{i_L}}{\delta nF(1-\frac{i}{i_L})} - \frac{2\gamma(\frac{2\pi}{\lambda})^2}{zF(\rho/M)} < 0, \tag{2.26}$$

where i_A is the current density for a flat interface, R is the gas constant, T is the operating temperature, i_L is the diffusion limiting current density, δ is the Nernst diffusion layer thickness, and λ is the wavelength of the sinusoidal perturbation. The first term represents the perturbation growth rate due to the electric field. The second term represents growth due to diffusion in the boundary layer, which does not exist in an unsupported electrolyte such as this case. The last term is the flattening of the interface due to surface tension. For this study with an unsupported electrolyte, the

stability criterion reduces to

$$\frac{i_A}{\sigma_e} < \frac{2\gamma(\frac{2\pi}{\lambda})^2}{zF(\rho/M)}. \tag{2.27}$$

Rearranging this equation by replacing the current/conductivity ratio in the electric field term with the potential gradient yields

$$\frac{\Delta\Phi}{L} < \frac{8\pi^2\gamma}{zF\lambda^2(\rho/M)}. \tag{2.28}$$

The potential can be plotted as a function of surface energy as:

$$\Delta\Phi = \frac{8\pi^2 L\gamma}{zF\lambda^2(\rho/M)}. \tag{2.29}$$

To verify our phase field model, we perform a series of simulations with sinusoidal perturbation on the cathode at varying applied potential, interfacial energy, electrode separations, and electronic conductivity. A sample of simulation domain is shown in Figure 2-6. It is noted that the cathode is located on the bottom in these simulations for convenience.

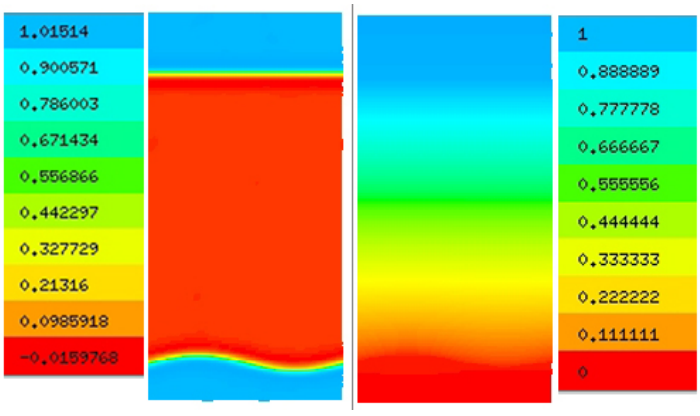

Figure 2-6: (Left) Phase field with a sinusoidal perturbation with wavelength λ on the cathode. (Right) Voltage contour with $\Phi = 1$ at the anode, top layer, and $\Phi = 0$ at the cathode, bottom layer.

The growth rate of the cathode roughness is estimated from the change in amplitude with time, where negative growth rate indicates stability and positive growth rate shows instability. The critical magnitude of the electric field and interfacial en-

ergy at the dimensionless scales are recorded. Figure 2-7 shows the critical the electric field as a function of the interfacial tension for an Fe-FeO solid-solid system. A series of linear plots from the phase field simulations, labeled as (B)-(D), are compared to the analytical result from Barkey's stability theory of a sharp interface [30], labeled as (A).

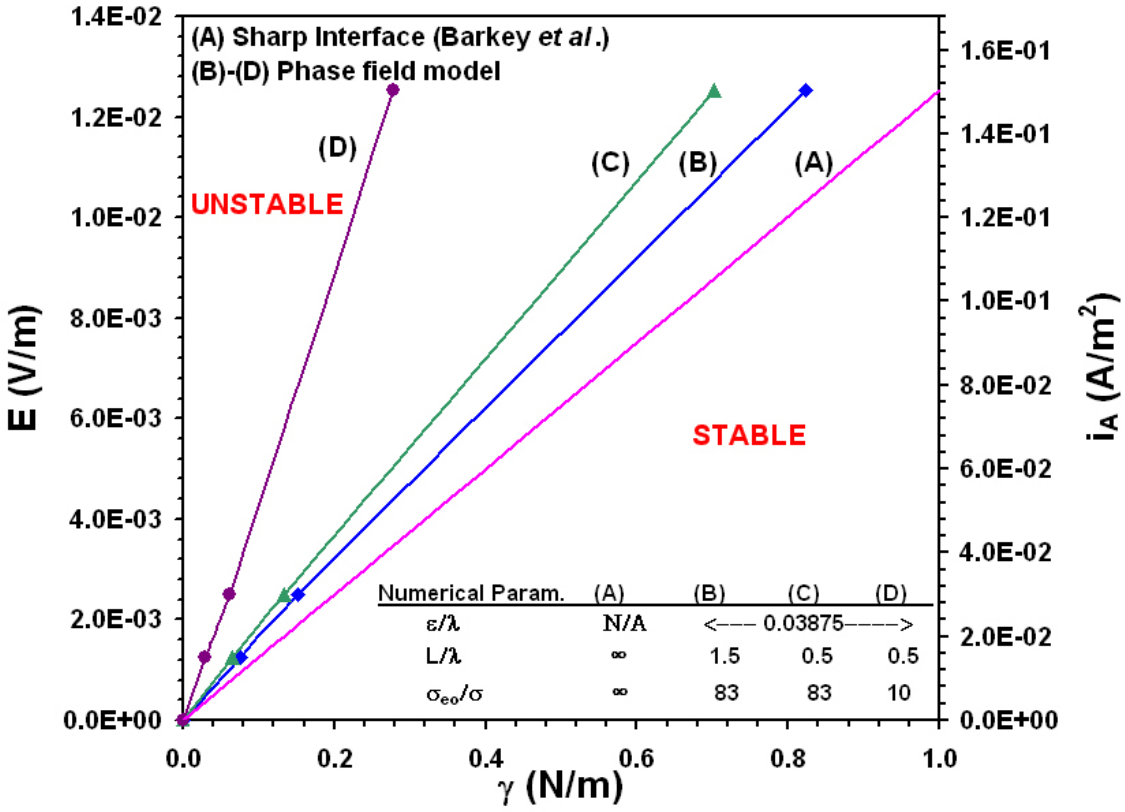

Figure 2-7: Comparison with linear stability analysis.

The results suggest that the cathode interface is more stable in the low electric field and high interfacial energy region. The deviation from the sharp interface model is slightly larger as the separation between electrodes (L/λ) decreases and much larger as the electronic conductivity ratio (σ_e/σ_i) decreases. Differences between this model and Barkey's results arise from three differences between the analytical and numerical models. The first difference is the diffuse interface introduced by the phase field model, for which results show that a more diffuse interface slightly enhances stability. The second is the finite cathode conductivity used in phase field model,

which also enhances stability. The third is the finite separation between electrodes, which is expected to reduce stability.

The stability criterion can also be expressed in terms of the dimensionless parameter Pe (Equation 2.17), for large values of which the interface is unstable. Other dimensionless parameters which characterize the system without convection are ε/λ, L/λ, and σ_e/σ_i. To study the effect of different parameters on the interface instability, the critical value of Pe is plotted as a function of these parameters as shown in Figure 2-8.

Based on the results in Figure 2-8a, the interface stability criterion remains almost unchanged at diffuse interface thickness less than 0.08λ. Referring to Section 2.1, the interface thickness is $\varepsilon \sim \sqrt{\alpha/\beta}$ and the interfacial energy is $\gamma \sim \sqrt{\alpha\beta}$. Decreasing β and increasing α while keeping the interfacial energy the same as the physical value will exaggerate the interface thickness for the simulation. This plot confirms that a diffuse interface thickness in the phase field model below 8% of the cathode wavelength can represent the sharp interface thickness since the stability behavior is not affected.

The next plot shown in Figure 2-8b illustrates the change in the critical Peclet number as a function of the distance between the two electrodes under a constant electric field conditions. The result from the phase field model with diffuse interface shows more stability than Barkey's model, which assumes infinite separation L. As mentioned above, smaller L is expected to lead to instability because of greater concentration of field lines, thus, the negative slope of this plot is not well-understood.

Figure 2-8c shows the critical Peclet number as a function of dimensionless electronic conductivity of the metal. It is observed that at high electronic conductivity, the interface is less stable. As the electronic conductivity of the metal approaches that of the slag ($\sigma_e/\sigma_i = 1$), Pe approaches infinity where the interface is always stable, because the electric field is uniform and there is no electrical driving force to cause the instability (see Equation 2.21).

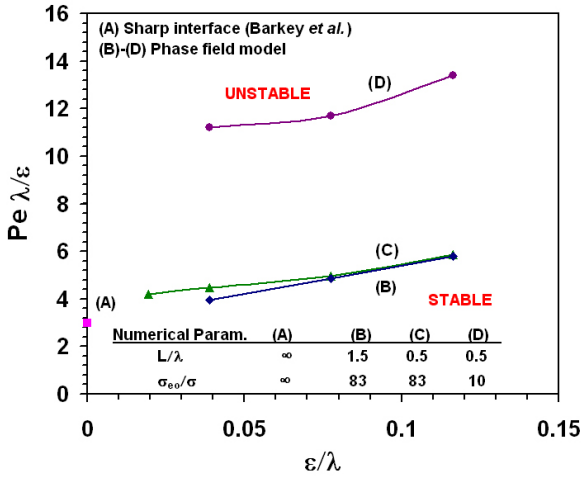

(a) Varying interface thickness

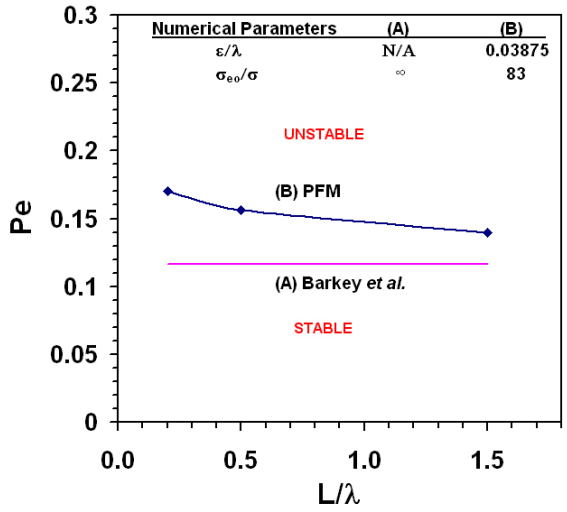

(b) Varying separation between electrodes

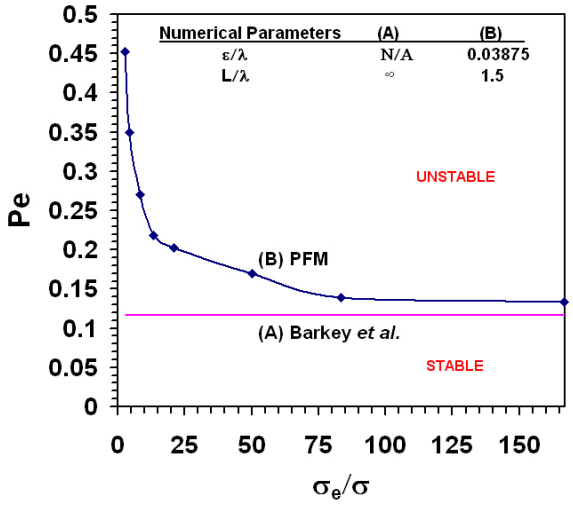

(c) Varying electronic conductivities

Figure 2-8: Stability Criteria with varying dimensionless parameters.

2.4 Binary Liquid-liquid Interface Motion Results

2.4.1 Effect of Convection on the Electrodes (2D)

To further investigate cathode interface stability, convection is included in the phase field simulation by coupling with the Navier-Stokes equations (Equation 2.25). In the liquid Fe-FeO system, interface stability is also influenced by the fluid viscosity. Here, the electrical potential and surface energy for an unstable solid condition are used, while the viscosity is varied. In the limit of high viscosity, the system behaves like the solid system such that the perturbation on the cathode is unstable. But as the fluid viscosity is reduced, flow provides a second mechanism, in addition to diffusion, to stabilize the interface as shown in Figure 2-9.

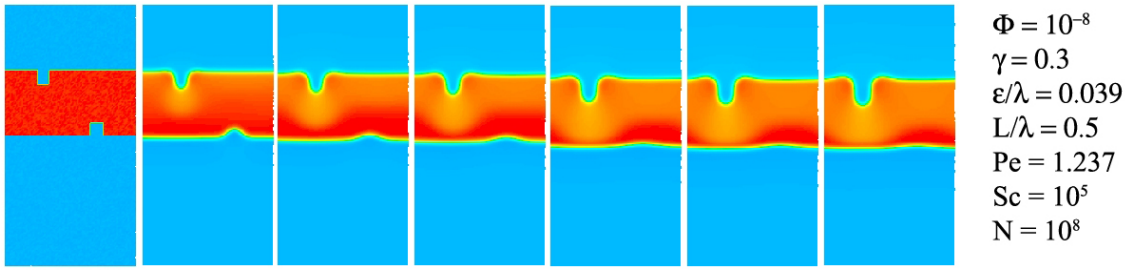

(a) Cathode shape evolution under high viscosity fluid. The perturbed cathode interface is unstable.

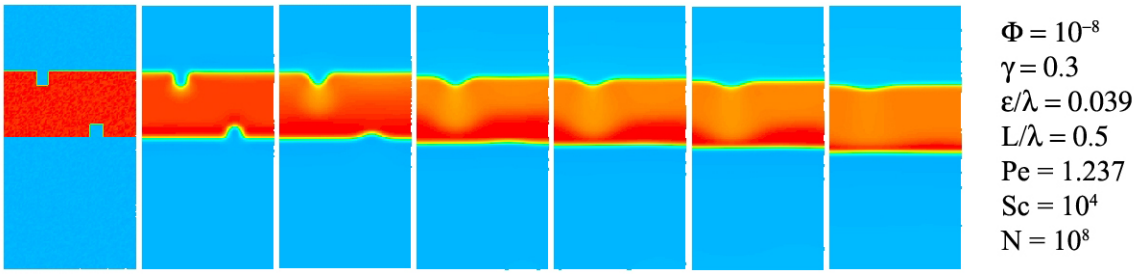

(b) Cathode shape evolution under low viscosity fluid. The perturbed cathode interface is stable.

Figure 2-9: Interface shape evolution with fluid flow on a domain size of 80x160. The left most plot shows the three layer initial condition: metal/electrolyte/metal.

2.4.2 Stability Analysis with Flow

Linear Stability Analysis To incorporate the effect of viscosity, consider a critically-stable perturbed liquid-liquid cathode-electrolyte interface. In the frame of reference of that interface, the momentum equation in velocity-pressure form scales as follows

$$0 = -\nabla P + \eta \nabla^2 \overrightarrow{U} \sim \frac{\Delta P}{\lambda} + \frac{\eta u}{\lambda^2}, \tag{2.30}$$

where P is pressure which scales as the second derivative of curvature $\Delta P = \frac{\gamma A}{\lambda^2}$. Substituting this for P and solving for u(m/s) leads to a velocity scale given by:

$$u \sim \frac{\gamma A}{\lambda \eta}. \tag{2.31}$$

This scaled velocity is equal to the rate at which the perturbation amplitude would shrink in the absence of other phenomena ($-\partial A/\partial t$). In the limit of low Schmidt number (Sc), the flow has a larger effect on the interface stability than the diffusive term, which can therefore be neglected. Adding this flow term to amplitude growth rate gives:

$$\frac{1}{A}\frac{\partial A}{\partial t} = \frac{\sigma_e(\frac{2\pi}{\lambda})}{zF(\rho/M)} \frac{\left(\frac{i_A}{\sigma_e}\right)}{\frac{1}{\sqrt{2}} + \frac{RT}{azFi_A}\sigma_e(\frac{2\pi}{\lambda})} - \frac{k_f \gamma}{\lambda \eta}. \tag{2.32}$$

where k_f is a flow scaling constant. When the right side is negative, the interface is stable. Therefore the stability criterion becomes:

$$\frac{\sigma_e(\frac{2\pi}{\lambda})}{zF(\rho/M)} \frac{\left(\frac{i_A}{\sigma_e}\right)}{\frac{1}{\sqrt{2}} + \frac{RT}{azFi_A}\sigma_e(\frac{2\pi}{\lambda})} < \frac{k_f \gamma}{\lambda \eta} \tag{2.33}$$

$$\frac{i_A}{\sigma_e} = \frac{\Delta\Phi}{L} = \frac{zF(\rho/M)k_f\gamma}{\sigma_e(\frac{2\pi}{\lambda})\lambda\eta}\left(\frac{1}{\sqrt{2}} + \frac{RT(\frac{2\pi}{\lambda})L}{azF\Delta\Phi}\right). \tag{2.34}$$

Multiplying both sides by $\frac{zF(\rho/M)\lambda}{\beta}$, the left hand side reduces to the Peclet number Pe :

$$Pe = \frac{\Delta\Phi zF(\rho/M)\lambda}{\beta L} < \frac{\rho}{\eta}\left(\frac{z^2F^2\rho k_f\gamma}{\sigma_e(\frac{2\pi}{\lambda})M^2}\right)\left(\frac{1}{\sqrt{2}} + \frac{RT(\frac{2\pi}{\lambda})L}{azF\Delta\Phi}\right). \tag{2.35}$$

On the right hand side, the first term can be written in terms of Sc given by $\frac{\eta}{\rho D}$:

$$Pe < \frac{1}{Sc}\left(\frac{z^2F^2\rho k_f\gamma}{\sigma_e(\frac{2\pi}{\lambda})M^2D}\right)\left(\frac{1}{\sqrt{2}} - \frac{RT(\frac{2\pi}{\lambda})L}{azF\Delta\Phi}\right). \tag{2.36}$$

Therefore, the critical value of Pe scales as $1/Sc$.

Simulation Results The result from our diffuse interface model shown in Figure 2-10 indicates that less viscous fluid (low Sc) introduces stronger flow and stabilizes the interface, whereas highly viscous flow (high Sc) does not. At low Sc on a log scale plot, the relationship between Pe and Sc is approximately linear with a slope of -1.10, which agrees well with the stability analysis described above.

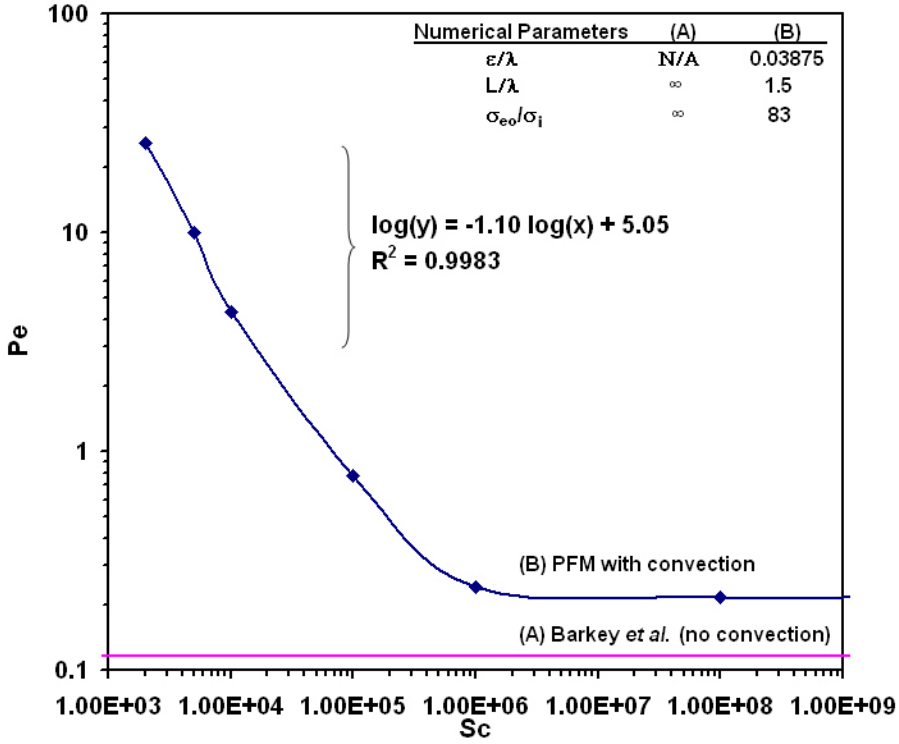

Figure 2-10: Log Pe vs. log Sc. The slope of -1.10 in the low Sc regime ($Sc < 10^6$) shows that the critical Pe is inversely proportional to Sc as expected.

At T=1773 K, liquid FeO has the following properties: viscosity $\eta_{FeO} = 0.20$ Pa·s [31], diffusivity $D_{FeO} = 4.20 \times 10^{-7}$ m^2/s [32], density $\rho_{FeO} = 3.50 \times 10^3$ kg/m^3, and interfacial tension $\gamma_{FeO} = 6.45 \times 10^{-1}$ N/m [33]. The value of Sc is 1.40×10^2. The

extrapolated critical Peclet number is therefore approximately 2.35×10^2, which is much larger than the critical value of Pe in the solid ($Pe_{solid} = 0.116$).

In the experiment of EFESR, a voltage of 2 V was applied across the electrodes separated by 10 cm. The diameter of a quenched cathode streamer was 0.2 mm [5], which corresponds to the primary dendrite spacing ∼0.4 mm. With electric field of 20 V/m and Equation 2.17, the corresponding critical wavelength for liquid-liquid system is approximately 0.46 mm. This result agrees well with the experimental observation.

In fact, the viscosity of electrolyte may be different from that of the metal electrodes. Future work of the binary model should take into account the variation of fluid properties with composition.

2.5 Summary

In this chapter, the phase field method is modified to include the electrostatic free energy term for modeling the electrochemical interface morphological evolution. This model can be applied to transport-limited electrolytic processes, satisfying rapid charge redistribution condition. For a binary model (unsupported electrolyte), our work presents two- and three-dimensional results showing the instability on the cathode interface in the Electric Field Enhanced Smelting and Refining process (Fe-FeO system). Our simulations indicate that the phase field model can capture the diffuse interface and complex interface shape and topology evolution successfully in two and three dimensions for transport-limited electrochemical reactions.

The cathode/electrolyte interface with small perturbation forms dendrites under a high voltage and low surface tension system. These dendrite arms grow faster at the tips, where the electrical potential gradient is steepest. Some longer-length dendrites reach the anode and short circuit the system, or some break due to Rayleigh instability. Three-dimensional results illustrate the interface in greater detail and correlate well with the two-dimensional unstable solid-solid interface. In contrast, under high interfacial tension or low viscous flow, the cathode/electrolyte interface

perturbation decays.

We perform a series of simulations with a small amplitude sinusoidal perturbation to determine the stability criteria. The critical electrical potential, surface tension and viscosity for a fixed wavelength and amplitude are calculated. The stability criteria can be represented in terms of the dimensionless numbers: Peclet and Schmidt numbers. As expected, the interface is unstable under high voltage, low surface tension and high viscosity, which correspond to high Peclet number and high Schmidt number. The two-dimensional solid-solid models approach the linear stability theory. The results from liquid-liquid system agrees well with the linear stability analysis derived in this thesis.

Chapter 3

Electrochemical Interface Dynamics in a Ternary System

Most high-temperature electrolytic processes employ a molten salt or molten oxide electrolyte which contains multiple species. The advantage of using more than one chemical species in the electrolyte is to form a eutectic system, allowing operation at lower temperature than the melting point of the pure salt or oxide (e.g., 1850 °C for TiO_2). The cation(s) in the electrolyte which does not participate in the reaction is referred to as a supporting electrolyte or a spectator agent. Thus, it is necessary to incorporate this multi-component feature into the phase field model of electrochemistry. This chapter addresses the derivation of the model and shows the simulations of interface dynamics as a function of the electrolyte composition. The motivating applications are titanium extraction processes. First, our work is focused on the effect of the spectator ions on the cathode evolution in the electrolytic smelting of titanium in general. Then, the phase field model is used to capture the formation mechanisms of titanium in a metallothermic reduction process as well, here using Subhalide reduction of titanium as an example.

3.1 Titanium Production

Titanium and its alloys have superior properties such as high strength, low density, great biocompatibility, and excellent corrosion resistance. These desirable properties make titanium an ideal material for aerospace, recreation, medical, and architectural purposes. Current technologies are able to process titanium into various parts for high-end applications such as jet engines, aircraft frames, golf clubs, tennis racquets, orthopedic implants, and exterior cladding of the Guggenheim Museum (Bilbao, Spain). However, the high cost of smelting and processing has prevented more extensive utilization of titanium. For over 50 years, the thermochemical Kroll process has served as the dominant extraction process for mass production of titanium [34], such that the cost of producing titanium ingot ($15,000/tons [35]) has remained many times higher than that of its free energy of dissociation ($\triangle G_{TiO_2}$ = 652 kJ/mol at 1,227 °C). In contrast, the cost of production for other commodity materials such as steel ingot is $600/tons [35].

3.2 Reviews of Titanium Extraction Processes

The titanium extraction process is an important cause of its high price. To reduce the production cost and compete with the Kroll process, emerging reduction processes have been invented such as the electrolytic processes with solid or liquid titanium cathode [36, 37, 38], calcium reduction [39] or magnesium reduction from subhalide [23].

Electrochemical extraction [36, 37] could be a crucial technology to significantly reduce the production cost because it would allow semi-continuous processing from less energy and lower-cost raw materials (TiO_2). Nonetheless, the scale-up of electrolytic process is limited by the mechanisms involved in the titanium formation such as diffusion and electronic conduction of the electrolyte, and the tendency to form dendrites.

A more practical development is the alternative reduction reactants. Examples

include the calciothermic reduction of TiO_2 [39] and magnesiothermic reduction of $TiCl_2$ [23]. The former involves no chlorine gas in the production. The latter can speed up the existing Kroll process without constructing a new plant facility.

A description of each process is given below, starting with the currently dominant Kroll Process.

Kroll Process

The conventional Kroll reduction process is a technique to produce titanium via a reaction of titanium tetrachloride ($TiCl_4$) with magnesium. In a steel reactor, $TiCl_4$ is fed into molten magnesium at temperature of 800-900°C to form titanium sponge and magnesium chloride ($MgCl_2$). The post-processing steps include electrolysis of $MgCl_2$ to yield magnesium for reuse and removal of $MgCl_2$ and magnesium from titanium sponge by vacuum distillation or acid leaching [34]. The reaction between $TiCl_4$ and magnesium is

$$TiCl_4(g) + Mg(l) \rightarrow Ti(s) + MgCl_2(l)$$

Even though this process has been in practice for many decades, it has several disadvantages. First, it requires pure $TiCl_4$ as a raw material, which in turn requires the toxic chlorine gas in the reaction. The electrolysis of $MgCl_2$ also produces chlorine gas, increasing the environmental concerns. Second, production may take more than 100 hours for the initial steps–spraying $TiCl_4$ into magnesium, introducing inert gas, cooling slowly to prevent nitriding and oxidation. Of these 100 hours, only 20-30 are used for reduction of $TiCl_4$ to titanium. Thus, this process has very high capital cost. Finally, the sponge titanium product needs subsequent processing to achieve full density and acceptable purity level, which further increases the overall cost.

FFC Cambridge Process

FFC is named after the investigators Fray, Farthing, and Chen [36]. It uses an electrochemical method to reduce solid TiO_2 cathode to titanium sponge or powder in molten calcium chloride. The experimental setup is shown in Figure 3-1.

The inventors suggest that the reduction mechanism is simply by oxygen ionization from TiO_2 by cathodic reduction:

$$TiO_x + 2xe^- \rightarrow Ti + xO^{2-}$$

However, the overall process is limited by diffusion of oxygen out of the pellet and by increased electronic conductivity of the electrolyte when TiO_{2-x} formed. Since this discovery in 2000, there have been extensive studies to understand and improve this process. Examples are a construction of electrical potential-partial pressure of oxygen diagram for Ti-Ca-O-Cl system [40] and a mathematical model of FFC process to test the pilot scale development [41].

MER

MER Corporation has developed an electrolytic process to produce powder or porous solid deposit by using TiO_2-C as an anode [37], which is significantly different from other electrolytic processes described in this sections. To make the anode, a mixture of rutile, binder, and carbonate is pressed and heat treated. The cathode can be made of steel or titanium. Mixed fused halides are used as an electrolyte. During the process, Ti^{3+} ions leave the anode and plate out at the cathode as CO/CO_2 bubbles out at the anode. According to the technical review of emerging titanium technology, production of titanium billets containing 300-500 ppm oxygen is under investigation, however more studies are required to analyze scale-up, impurity, and economic issues [42].

Electrolytic Extraction in Liquid State (Ginatta Process)

Electrolytic reduction of titanium in liquid state was invented by Marco Ginatta [38]. The system includes a copper cathode crucible containing a pool of liquid titanium in a skull of solidified titanium, a bath of lower density liquid electrolyte, a non-consumable anode, and a feeding system to resupply $TiCl_4$ and electrolyte, which is illustrated in Figure 3-2. The process takes place inside an air-tight container. As the current is passed through the system, cathodic reduction produces liquid titanium,

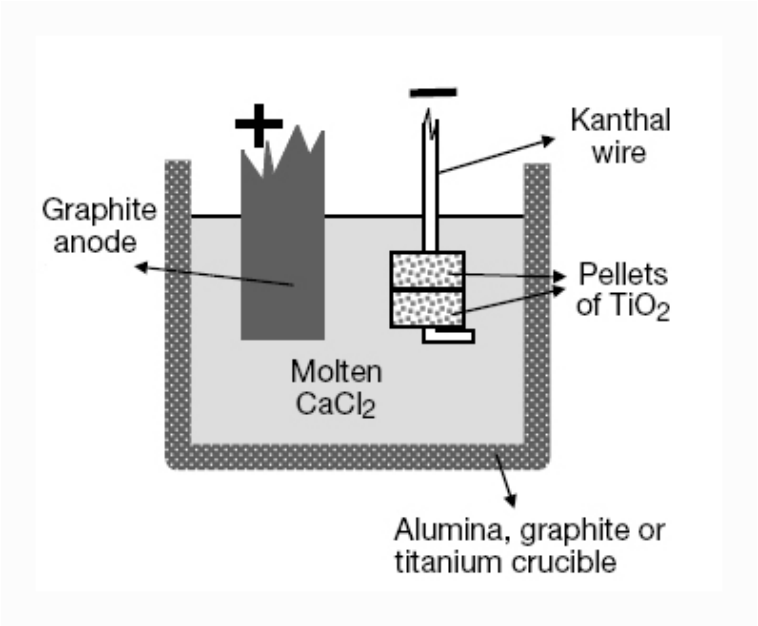

Figure 3-1: A schematic representation of FFC Cambridge process [36].

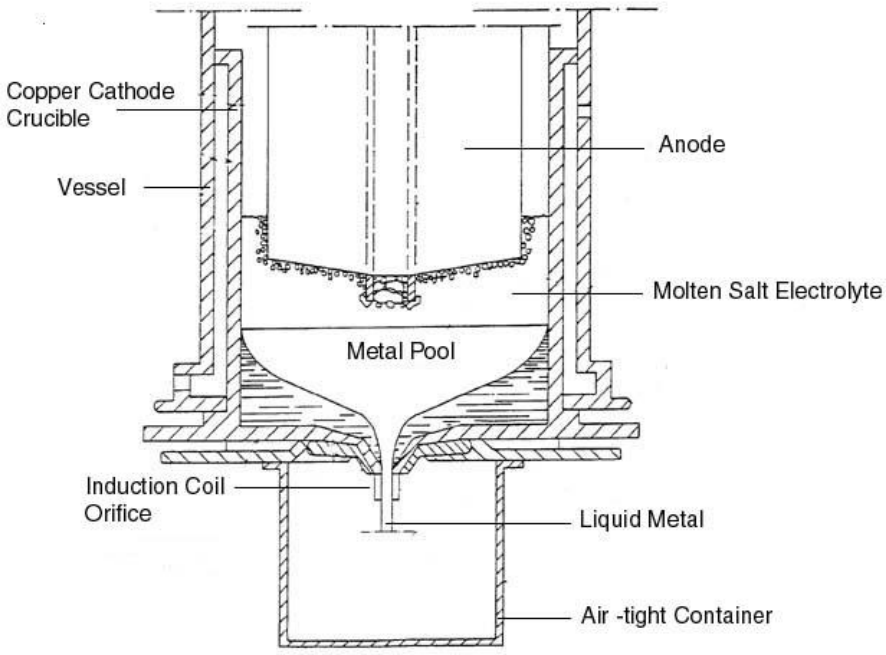

Figure 3-2: The configuration of Electrolytic extraction in liquid state [38].

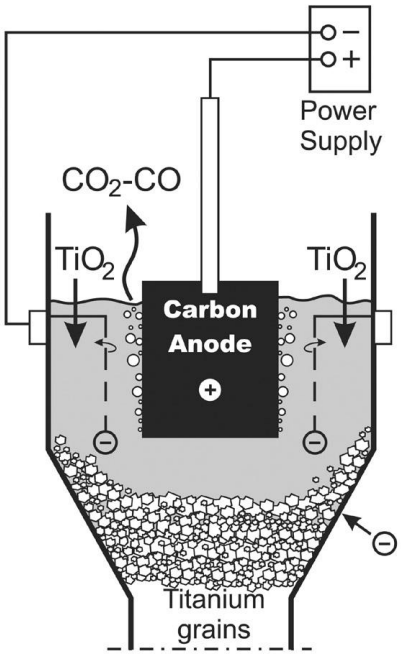

Figure 3-3: A schematic illustration of Calciothermic reduction process [39].

which is continuously collected by the induction orifice. The significant benefit of this technique is that the liquid titanium can be made into plates, slabs, or billet directly. However, as with the Kroll process the raw material is expensive and involves chlorine gas in the synthesis.

OS process

A calciothermic reduction process has been invented by Ono and Suzuki of Kyoto University [39] for continuous processing of titanium sponge via the reaction of TiO_2 with Ca. A schematic illustration is shown in Figure 3-3. The reduction cell consists of an iron vessel cathode containing molten Ca-$CaCl_2$ and a consumable carbon anode. The voltage between anode and cathode is set at 3 V to prevent decomposition of $CaCl_2$; therefore, no chlorine gas is involved in the process. When the raw material, TiO_2 powder, is fed near the cathode, it reacts with liquid Ca droplets by the following reactions:

$$Ca^{2+} + 2e^- \rightarrow Ca$$

$$TiO_2 + 2Ca \rightarrow Ti + 2CaO$$

It is noted that the reaction pathway in OS process is different from that of FFC process. Here, Ono and Suzuki suggest that removal of oxygen from titanium ore is via the secondary reduction step where TiO_2 is reduced by calcium. The sponge titanium is precipitated with the morphology of granules. To recover the sponge, the titanium granules are continuously removed from the bottom, making it a continuous process. The byproduct CaO reacts with carbon anode where CO_2 gas is emitted.

According to Suzuki's experiment, the calciothermic process consumes 50% less electrical power than the Kroll process. However, the sponge titanium product contains impurities, which requires post-processing to transform the sponge into usable form. In addition, the problem of heat released from the reaction and the heat supplied to maintain the molten salt can damage the carbon anode. More experimental work is required to make this process commercially feasible.

Subhalide Reduction Process

The subhalide reduction process has recently been developed by Okabe and Takeda [23]. The process concept is modified from the conventional Kroll process. Since $TiCl_4$ undergoes subchlorides cycling during the Kroll process, the production speed is slow. A practical approach proposed by Okabe and Takeda to speed up the titanium production is to start the magnesiothermic reduction by using the subchlorides of titanium ($TiCl_3$ or $TiCl_2$). The vapor pressure of these subchlorides are significantly lower than that of $TiCl_4$. Thereby, the reduction can be carried out in condensed phase, leading to higher production rate. Operating temperature is 1073 K. Figure 3-4 illustrates the high-speed, semi-continuous reduction process.

To improve the production rate in this process, one must understand the reaction pathways and locations occurred in the process. From the electrochemical reaction, titanium is produced via reduction of $TiCl_2$ by Mg. As discussed earlier in Section 1.1, a high-temperature electrochemical reaction is a mass-transport limited process. Nonetheless, the electron transport between metals also has a significant effect on

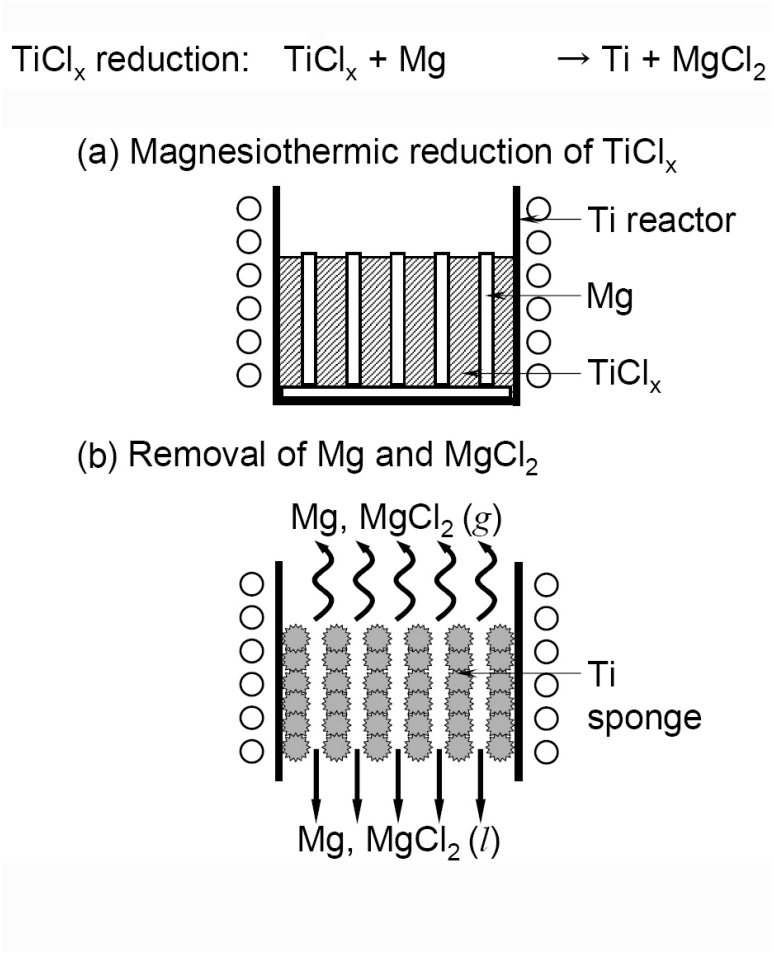

Figure 3-4: A schematic diagram of production steps in the subhalide reduction process (a) magnesiothermic reduction of $TiCl_x$, and (b) removal of by-products ($MgCl_2$) and excess magnesium by vacuum distillation and draining [23].

the product morphology as claimed by Okabe and Sadoway [43] in the tantalum reduction process. Their experiments show that tantalum can be formed even when the reactants are not in physical contact as long as there is an electron conducting medium to transfer electrons. The formation of product phase via this mechanism is referred to as electronically mediated reaction (EMR). Uda *et al.* [44] have applied the mechanism of EMR to develop a contactless electrochemical reduction of $TiCl_2$ with aluminum. When the formation of titanium is by EMR, the morphology and location of the deposit can be controlled.

All of the current researches mentioned above require a better understanding of the titanium formation mechanisms. In this study, a phase field model for ternary system is developed. For the electrolytic process, the goal is to investigate the growth of the cathode interface in the presence of spectator ion and to determine the stability criteria. For the Subhalide reduction model, the goal is to study the formation and structure of Ti produced via magnesiothermic reduction of $TiCl_2$ and the electronically mediated reaction (EMR). For simplicity, all simulations in this chapter are done without convection.

3.3 Phase Field Formulation for Ternary System

The governing equation derivation in this section is based on a model Ti-Mg-F ternary system. The molten salt electrolyte contains MgF_2 and TiF_2, which serve as generic components for the purpose of model development. Under an applied voltage, titanium fluoride is electrolytically reduced. The half cell reaction is written as:

$$Ti^{2+} + 2e^- \rightarrow Ti.$$

To parameterize the phase variables for Mg, Ti, MgF_2, TiF_2, we define C_2 as the fraction of titanium metal or fluoride, and C_3 as the fraction of metal (vs. fluoride). Thus C_2 is zero for Mg and MgF_2, and unity in Ti and TiF_2, whereas C_3 is zero in fluoride phases and unity in pure metal phases.

Based on thermodynamics of the multi-component system, the free energy functional $\mathcal{F}$, as a function of phase parameters can be expressed as a volume integral of

the sum of all free energy terms:

$$\begin{aligned} \mathcal{F} &= \int[\Psi + \sum K_{ij}\nabla C_i \cdot \nabla C_j + F\Phi \sum_i^n z_i c_i]dV, \\ &= \int[\Psi + K_{22}|\nabla C_2|^2 + K_{33}|\nabla C_3|^2 + F\Phi \sum_i^n z_i c_i]dV, \end{aligned} \tag{3.1}$$

where Ψ is the homogeneous free energy density function, K_{22} and K_{33} are the gradient penalty coefficients (corresponding to α in the binary system). The system is assumed to be isotropic, thus the cross terms (i.e., K_{23} and K_{32}) are zero. The final term in equation (3.1), $F\Phi \sum_i^n z_i c_i$, is the electrostatic free energy contributed by charge on ions. The molar concentration of species i, c_i, in this system can be represented by molar density and mole fraction as:

$$\begin{aligned} c_{Ti^{2+}} &= \frac{\rho}{M}\left(\frac{1}{3} + \frac{2}{3}C_3\right)C_2 \\ c_{Mg^{2+}} &= \frac{\rho}{M}\left(\frac{1}{3} + \frac{2}{3}C_3\right)(1 - C_2) \\ c_{F^-} &= \frac{\rho}{M}\left(\frac{2}{3}\right)(1 - C_3). \end{aligned} \tag{3.2}$$

In this model, density, ρ, is assumed to be uniform. Molar mass M is $X_{Ti}M_{Ti} + X_{Mg}M_{Mg} + X_F M_F$. Then the $\sum_i^n z_i c_i$ term in the free energy functional is simplified to zC_3, where $z_{Ti} = z_{Mg} = z$ and $z_F = -z/2$.

A homogeneous free energy model is derived from simple binary free energy models. At T=1100 K, it is assumed that magnesium and titanium chlorides form an ideal solution. The mixing of metal-chlorides and metal-metal phases are assumed to be regular solutions with miscibility gaps. The dimensionless homogeneous free energy density is

$$\begin{aligned} \Psi_0 &= C_2 ln C_2 + (1 - C_2)ln(1 - C_2) + \Omega_{12}C_2C_3(1 - C_2) + \\ &\quad C_3 ln C_3 + (1 - C_3)ln(1 - C_3) + \Omega_{13}C_3(1 - C_3) - \\ &\quad (C_2 - 0.5)(C_3 - 0.5). \end{aligned} \tag{3.3}$$

The first two terms are entropic terms in the Ti-Mg and TiF_2-MgF_2 systems. The third term forms the miscibility gap between metallic titanium and magnesium, scaled by C_3 so that it is zero in the fluorides. The fourth and fifth terms are entropic terms

in metal-fluoride systems. The sixth term introduces the miscibility gap between metals and fluorides. The final term is the chemical driving force for the reaction of TiF_2+Mg→ Ti+MgF_2. In our simulation, the interaction term between metals, Ω_{12}, is 3.3, and that between metal fluorides, Ω_{13}, is 2.5. The three-dimensional plot of free energy function is shown in Figure 3-5

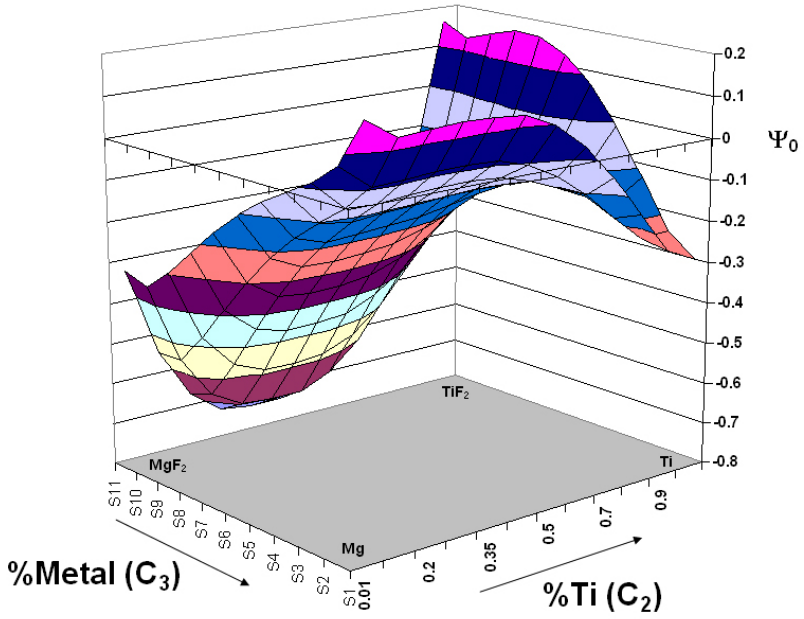

Figure 3-5: Free energy function of Ti-Mg-F ternary system. Metal-metal and metal-fluoride mixtures form regular solution with miscibility gap. Fluorides form ideal solution. Product phases (Ti and MgF_2) have lower free energy than the reactant phases (Mg and TiF_2)

The chemical potential for each phase μ_i is derived by taking the variational derivative of the free energy functional.

$$\mu_2 = \frac{\partial \Psi_0}{\partial C_2} - K_{22}\nabla^2 C_2 \tag{3.4}$$

$$\mu_3 = \frac{\partial \Psi_0}{\partial C_3} - K_{33}\nabla^2 C_3 + \frac{z\rho F}{M}\frac{(1-C_3)}{(1+C_3)}\Phi = \mu_3' + \frac{z\rho F}{M}\frac{(1-C_3)}{(1+C_3)}\Phi. \tag{3.5}$$

Like the binary model, μ_3' is the chemical potential of metal ions. Again, the electrostatic term is multiplied by $(1-C_3)/(1+C_3)$ to make it valid in metal and electrolyte

phases. The flux of C_2 and C_3 is driven by the gradients of these potentials (μ_2 and μ_3).

3.3.1 Governing Equations for Ternary System

Conservation of Species

The conservation equations of each parameter can thus be written in terms of mobility M_{ij} driven by electrochemical potential gradient $\nabla\mu_j$) as:

$$\frac{\partial C_2}{\partial t} + \overrightarrow{U} \cdot \nabla C_2 = M_{22}\nabla^2\mu_2 \tag{3.6}$$

$$\frac{\partial C_3}{\partial t} + \overrightarrow{U} \cdot \nabla C_3 = M_{33}\nabla^2\mu_3' + M_{33}\frac{zF\rho}{M}\nabla\cdot\left(\frac{1-C_3}{1+C_3}\nabla\Phi\right), \tag{3.7}$$

It is noted that electromigration only appears in the electrolyte. The mobilities of species driven by their chemical potential are assumed to be the same magnitude ($M_{22} = M_{33}$). The mobilities of species driven by other chemical potential (M_{23} and M_{32}) are assumed to be zero. Mobility can be expressed in terms of diffusivity D_{ij} according to Fick's law of diffusivity as:

$$M_{ij} = \frac{D_{ij}}{\frac{\partial^2\Psi}{\partial C_j^2}} \tag{3.8}$$

Dimensionless parameters are defined as $\tilde{t} = \frac{t}{\lambda^2/\overline{D}} = \frac{t}{\lambda^2/M_{33}<\Psi''>}$, where $<\Psi''>$ is the characteristic value of Ψ'', $\tilde{\mu} = \frac{\mu}{<\Psi''>}$, $\tilde{\nabla} = \lambda\nabla$, and $\tilde{\Phi} = \frac{\Phi-\Phi_{cathode}}{\Phi_{anode}-\Phi_{cathode}} = \frac{\Phi-\Phi_{cathode}}{\triangle\Phi}$. Thus the dimensionless equations are expressed as:

$$\frac{DC_2}{D\tilde{t}} = \tilde{\nabla}^2\tilde{\mu_2} \tag{3.9}$$

$$\frac{DC_3}{D\tilde{t}} = \tilde{\nabla}^2\tilde{\mu}_3' + \mathcal{B}\tilde{\nabla}\cdot\left(\frac{1-C_3}{1+C_3}\tilde{\nabla}\tilde{\Phi}\right). \tag{3.10}$$

The dimensionless parameter $\mathcal{B}$ is the ratio of the electrostatic free energy density to the diffusive free energy density, $\frac{zF(\rho/M)\triangle\Phi}{<\Psi''>}$. In the simulation, $\mathcal{B}$ is set to one.

Conservation of Charge

In a supporting electrolyte, transport of charge due to diffusion needs to be considered as well. Thus, the conservation of charge equation is

$$0 = \nabla \cdot (zFM_{33}\nabla\mu_3') + \nabla \cdot (\sigma_{eff}\nabla\Phi), \tag{3.11}$$

where $\sigma_{eff} = \frac{(1-C_3)}{(1+C_3)} + \frac{\sigma_e}{\sigma_{electrolyte}}$. Here, we define σ_e as $\sigma_{e_0}(3C_3^2 - 2C_3^3)\left(1 - \frac{1}{2}C_2\right)$. Thereby σ_e is zero in the fluoride phases, and σ_e of titanium is half of that of magnesium. Rapid charge redistribution condition is still applicable to this ternary system.

3.4 Solid-Solid Cathode Interface Motion

3.4.1 Simulation Setup and Parameters

A simple two-layer structure is used throughout the study in this ternary model. It is noted that the free energy includes logarithmic functions, such that values of zero and unity of phase variables are not allowed. Thus, it is important to set the initial concentrations that correspond to the desired phase based on the phase diagram shown in Figure 3-6.

Initial Conditions and Boundary Conditions

The cathode is titanium (C_2, C_3 close to 1). The electrolyte contains a mixture of MgF_2 and TiF_2. To investigate the concentration-dependent system in this ternary case, we look at four tie lines in the two-phase region (Ti-XF_2). These tie lines are obtained by letting two-layer structure with at each initial concentrations go toward equilibrium and recording their concentrations. The compositions of two-phase tie lines are summarized in Table 3.1.

In the x direction, periodic boundary conditions are applied. In the y direction, different boundary conditions are applied. For composition, C_i are fixed such that the cathode is in Ti phase (second column of Table 3.1) and the anode is supplying

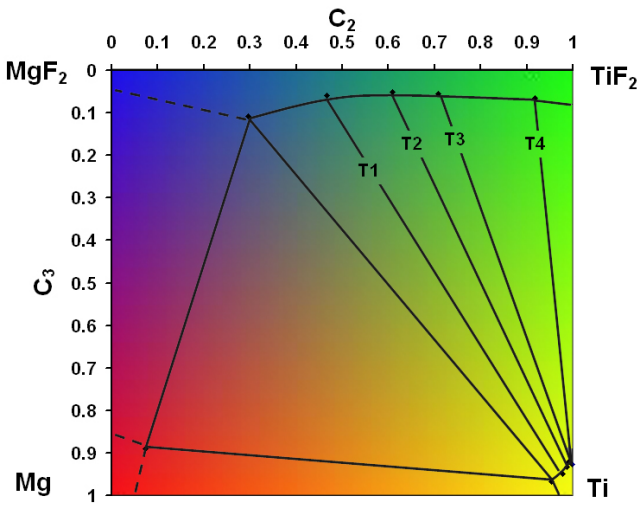

Figure 3-6: Ternary phase diagram showing a three-phase region with $\Omega_{12} = 3.3$ and $\Omega_{13} = 2.5$. Note that the phase color notation is only used in the result presentation in Section 3.5 Subhalide Reduction Process.

Table 3.1: Equilibrium compositions for the two-phase region (Ti-XF_2)

Case	Titanium (C_2, C_3)	XCl_2 (C_2, C_3)
T1	(0.9768, 0.9498)	(0.4657, 0.0587)
T2	(0.9862, 0.9332)	(0.6077, 0.0519)
T3	(0.9906, 0.9215)	(0.7085, 0.0554)
T4	(0.9978, 0.9274)	(0.9170, 0.0645)

constant amount of TiF_2 (0.9, 0.05). For voltage, Φ is zero at the cathode and fixed to the applied voltage at the anode.

Parameters Study

The gradient energy coefficients, K_{22} and K_{33}, in Equation 3.1 affect the interface thickness and surface tension. Both interface thickness and surface tension increase with K_{ii}. The value of K_{ii} is selected such that the interface thickness is smaller than the diffusion lengthscale, but larger than the grid spacing. We choose $K_{22} = K_{33} = 5 \times 10^{-4}$.

Interfacial energy depends on composition, and is calculated by simulating steady-state behavior of a two-layer structure with half titanium and half electrolyte. First

the total free energy is calculated from Equation 3.1 by integrating the free energy over the volume (area for 2D). Then the homogeneous free energy of each phase is subtracted from the total free energy. Finally, dividing the value by the interfacial area yields the interfacial energy as shown in Figure 3-7.

$$\gamma A_{int} = \mathcal{F} - \Psi_{Ti} A_{Ti} - \Psi_{XF_2} A_{XF_2} \tag{3.12}$$

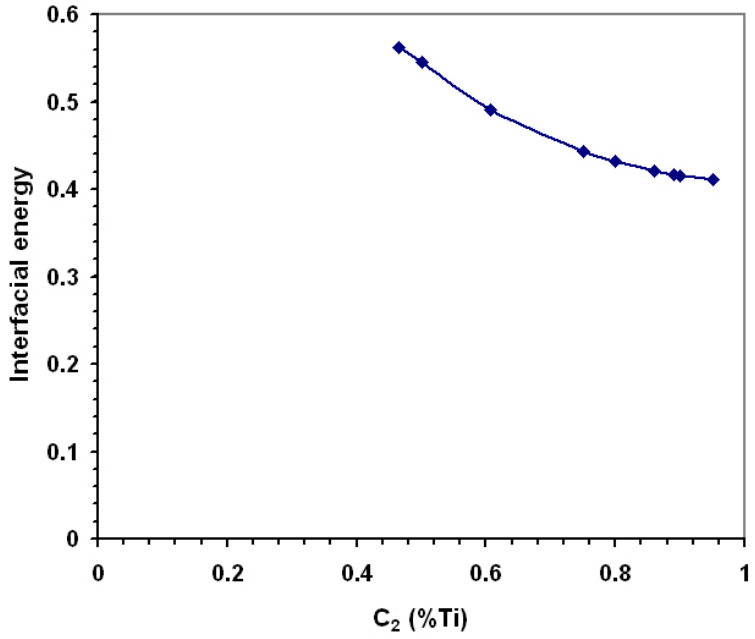

Figure 3-7: Interfacial energy as a function of C_2 for $K_{22} = K_{33} = 5 \times 10^{-4}$

In this system, the more supporting electrolyte the higher the surface tension.

3.4.2 Effect of Electrolyte Composition

First, the composition-dependence of interface evolution is studied by exploring the solid-solid system. Again, a small box perturbation is added to the cathode, which locates on the bottom layer through out the ternary simulations in this chapter. The phase field result of an unstable interface for case T2 with $E = \triangle\Phi/\triangle y = 16.0$ is displayed in Figure 3-8. The result shows that the perturbation grows faster than the

flat surface as expected. In Figure 3-8a, the concentration gradient of C_2 at the peak is also shown to be steeper than that in front of a flat surface. Thus the titanium ion depleted layer is thinner at the dendrite front, leading to larger driving force ($\nabla\mu_2$ or ∇C_2) for mass transport. Whereas in the binary case, this concentration boundary layer does not exist, which is similar to what is observed on the C_3 field shown in Figure 3-8b.

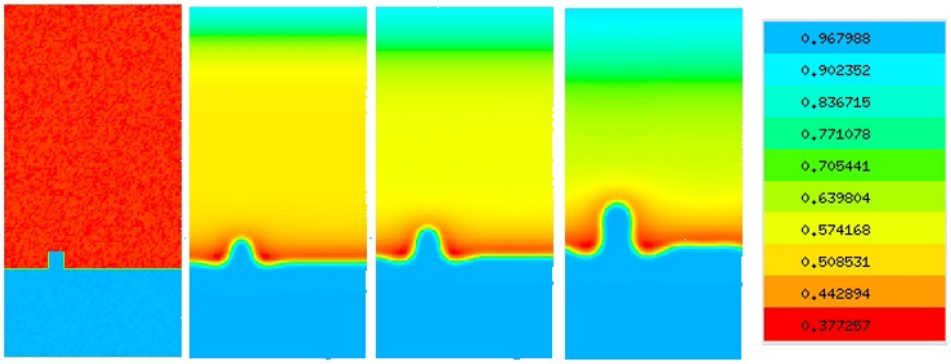

(a) C_2 contour shows thinner concentration boundary layer thickness at the peak of the perturbation.

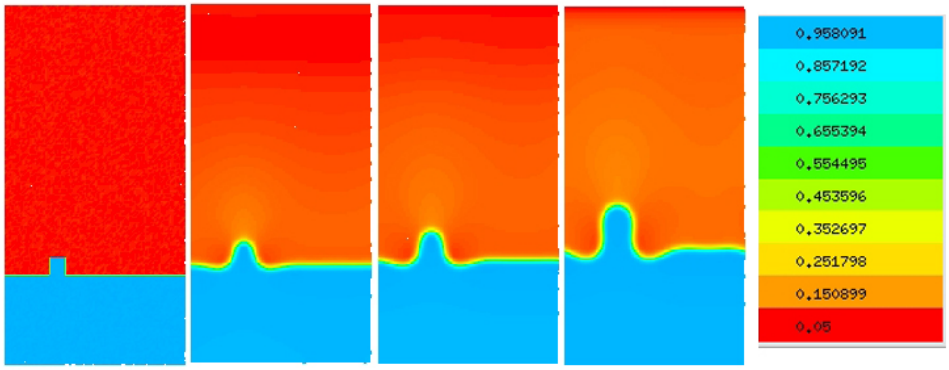

(b) C_3 is roughly uniform in each phase.

Figure 3-8: A representative result of an unstable interface for an electrolyte with initial composition T2 and without convection. Note that the voltage contour is not shown.

Another way to examine the driving force in detail is by plotting the composition gradient at different locations on the interface. To emphasize the difference, we plot the gradients of cation C_2 and the electric field at the dendrite tip ($\tilde{x}$=0.3) and the flat surface ($\tilde{x}$=0.6) at time $\tilde{t}$=0.014 shown in Figure 3-9.

It is noted that the concentration profile has not reached the steady-state ($\tilde{t}$ =

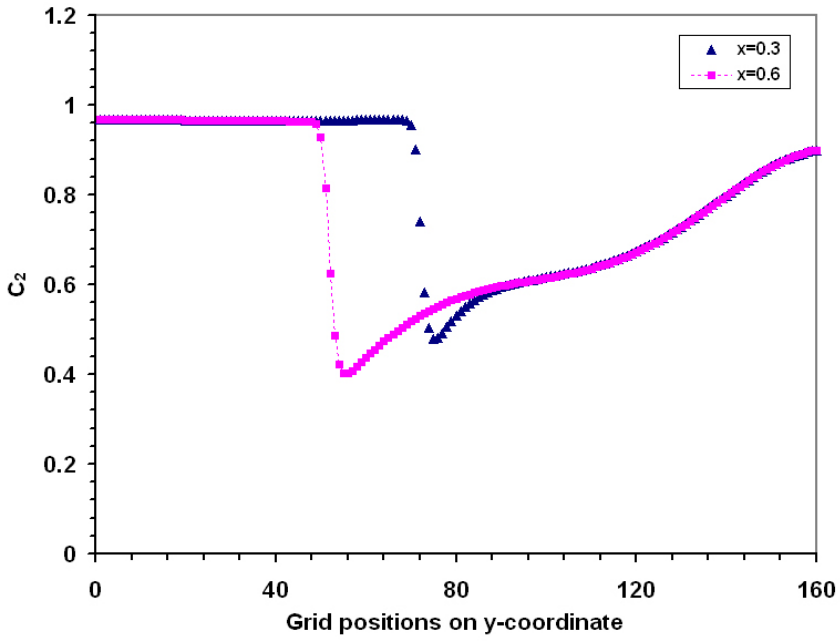

(a) Titanium ion concentration C_2 along the y coordinate at the peak of the perturbation ($\tilde{x}$=0.3) and at the flat interface ($\tilde{x}$=0.6).

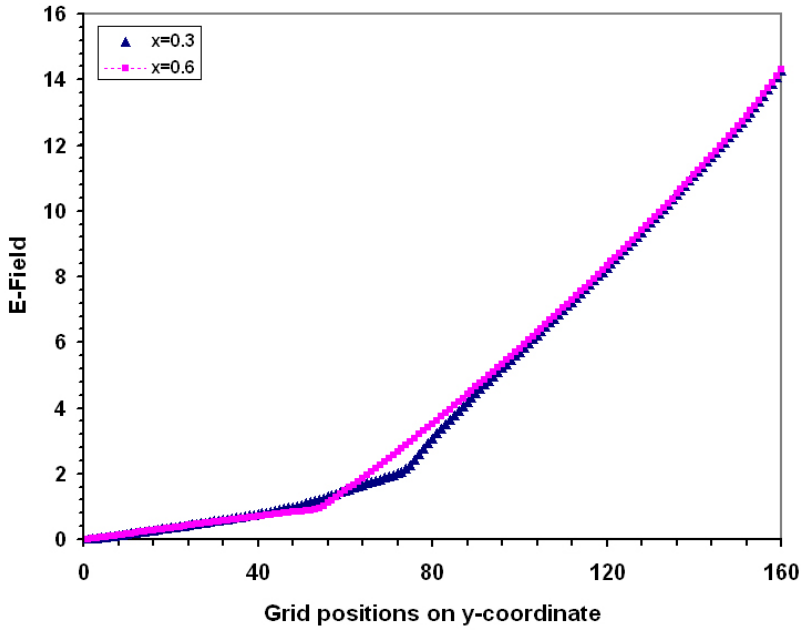

(b) Electrical potential Φ along the y coordinate at the peak of the perturbation ($\tilde{x}$=0.3) and at the flat interface ($\tilde{x}$=0.6).

Figure 3-9: Gradient plots along the y direction. The gradients ahead of the protrusion (triangle-blue) are greater than that of the flat interface (square-pink).

1.0). However, the purpose here is to convey a more quantitative comparison of the gradients at the cathode/electrolyte interface. Both C_2 and electric field gradient are steeper at the peak of the perturbation.

Next, more simulations with the same perturbation configuration and applied electric field as shown in Figure 3-8 are carried out for case T1 and case T4. The amount of spectator ion (Mg^{2+}) is T1 > T2 > T4. In each case, the interface morphology is compared to the C_2 concentration gradient ahead of the growing dendrite. The results are plotted as shown in Figure 3-10. Plot 3-10a and 3-10b are the cation gradient at $\tilde{t} = 0.007$ and $\tilde{t} = 0.014$, respectively. At the beginning, case T1 shows smaller gradient compared to T2. At later time, the gradient of case T1 increases, but still slightly less than that of case T2. The morphology shows that deposition rate of case T4 is greater than T2 and T1 as observed by the protrusion distance. Moreover, some early stage stabilization of the interface is observed in case T1 which has more supported electrolyte with higher interfacial energy. However, these results shown here are far from steady-state. Long-time simulations on these cases are performed. The result shows that under this applied electric field, the perturbation in any concentrations of spectator ions are unstable.

Finally, a more perturbed cathode interface simulation is conducted. Complex topology changes can be captured by this phase field model. Shown in Figure 3-11 are the C_2 map for case T2. As expected again, the dendrite tips protrude in direction of the largest titanium ion gradient.

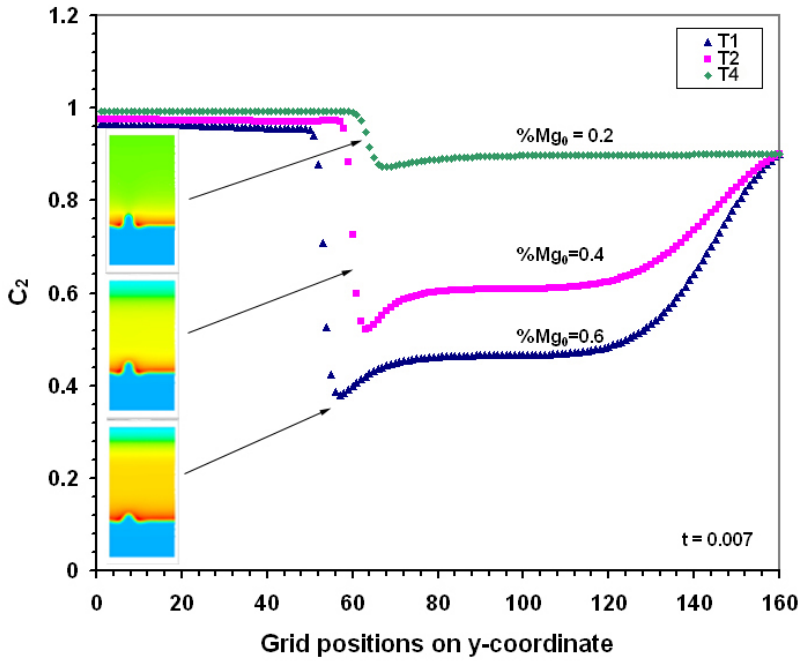

(a) Titanium ion concentration C_2 along y-coordinate at the peak of the perturbation ($\tilde{x}$=0.3) for three cases at $\tilde{t} = 0.007$.

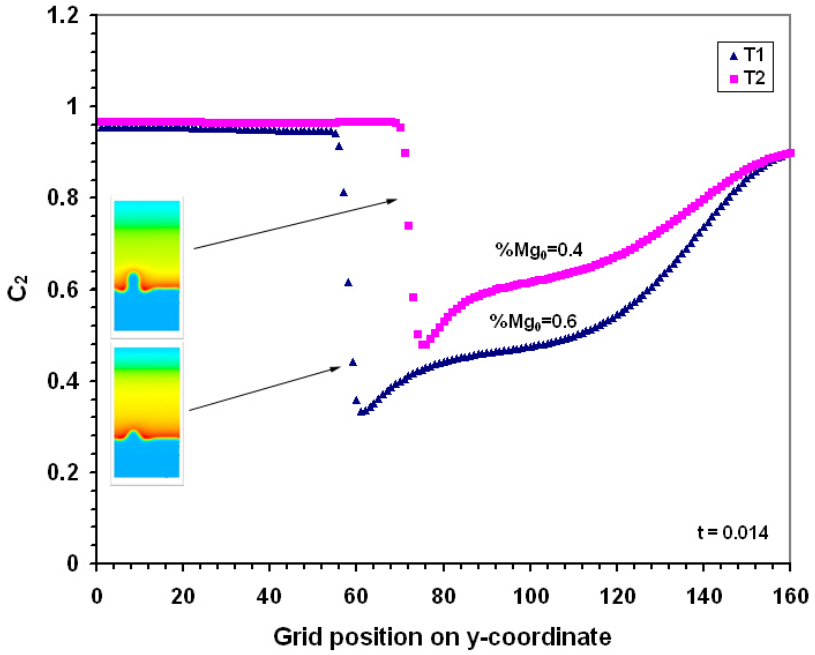

(b) Titanium ion concentration C_2 along y-coordinate at the peak of the perturbation ($\tilde{x}$=0.3) for three cases at $\tilde{t}$=0.014.

Figure 3-10: Titanium ion concentration gradients for case T1, T2, and T4. At later time, C_2 gradient increases with increasing spectator ion concentration.

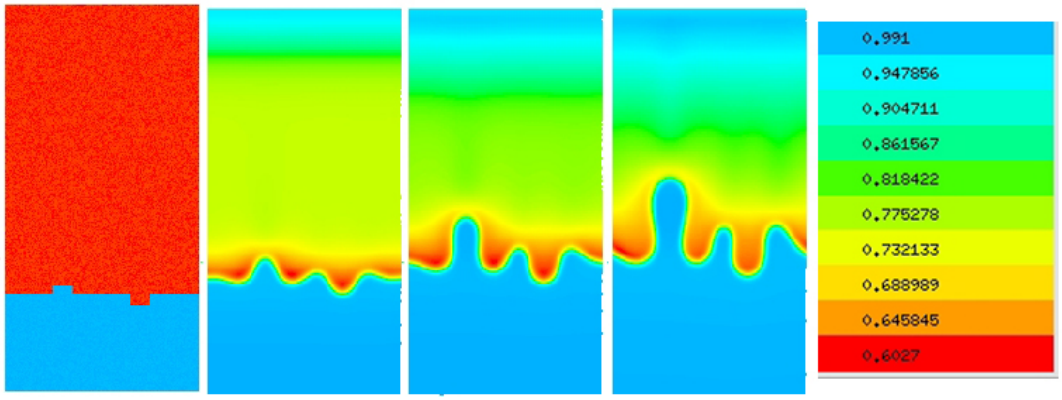

(a) C_2 contours show thinnest concentration boundary layer at the highest peak.

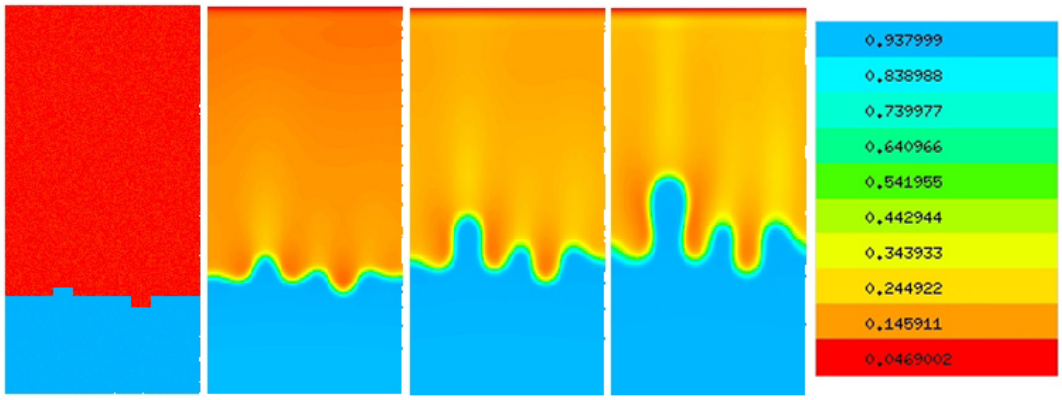

(b) C_3 contours

Figure 3-11: Highly perturbed cathode interface develops into dendrites. (150×300)

3.4.3 Stability Criteria

Previous simulations are mostly for qualitative representation of the topology evolution under different cation concentration gradient. To gain quantitative results of these phenomena, a linear stability analysis of the diffuse interface is carried out for a small sinusoidal perturbation.

The simulations are re-centered in order to allow longer run time to steady-state. The re-centering speeds are calculated from the interface growth velocities in the one dimensional simulations for each case. In this model, the interface growth velocity is a linear function of the applied electric field (u_{int}=$mE + n$). Thus the re-centering speed is equal to this linear function in the downward direction. In this system, the porpotional factors and interception are listed in Table 3.2. It is noted that our

Table 3.2: Interfacial velocity function u_{int}=$mE + n$

Case	m	n
T1	0.9026	-0.3262
T2	0.9488	-0.2255
T3	1.0194	-0.2513
T4	1.0702	-0.0558

simulations are carried out with the rough estimation of $u_{re-center} = -mE$ as the recentering velocity.

For a solid-solid ternary system, a stability map as a function of spectator ion concentration is plotted as shown in Figure 3-12. This plot is an asymtotic curve. In the limit of high spectator ion concentration, it is shown that the interface becomes more unstable with increasing spectator ion concentration. In the limit of an unsupported electrolyte, the interface is stable below a critical Peclet number. Above this value, the interface is always unstable against any perturbation with or without a supporting electrolyte.

This phenomena can be explained by the role of supporting electrolyte. Here, the metal ion concentration gradients ahead of the protrusion at the same applied electric field are plotted. Figure 3-13 shows that the titanium ion concentration gradient increases with increasing spectator ion. The result agrees with Haataja's work on arbitrarily supporting electrolyte [10].

Thus the results without convection reported here predict the correct behaviors as those in the literature. Further investigation on a solid-liquid system will better represent the physical phenomena involving flow. More discussions on the solid-liquid feature and fluid flow will be covered in chapter 4.

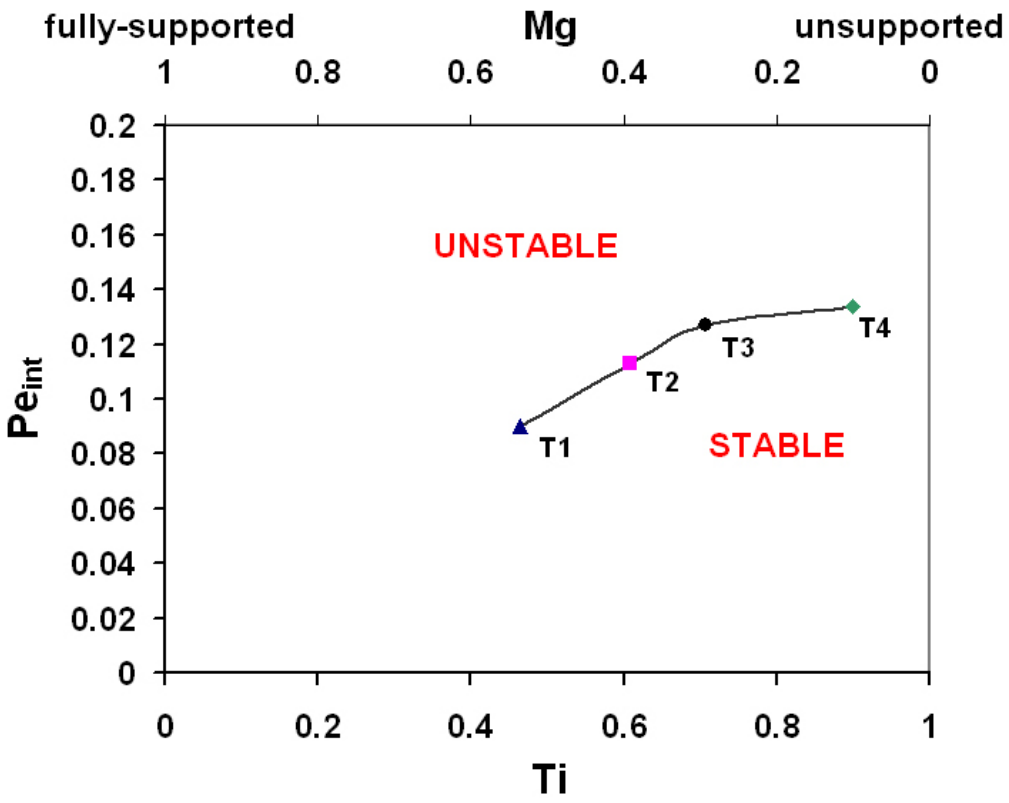

Figure 3-12: Stability plot as a function of composition.

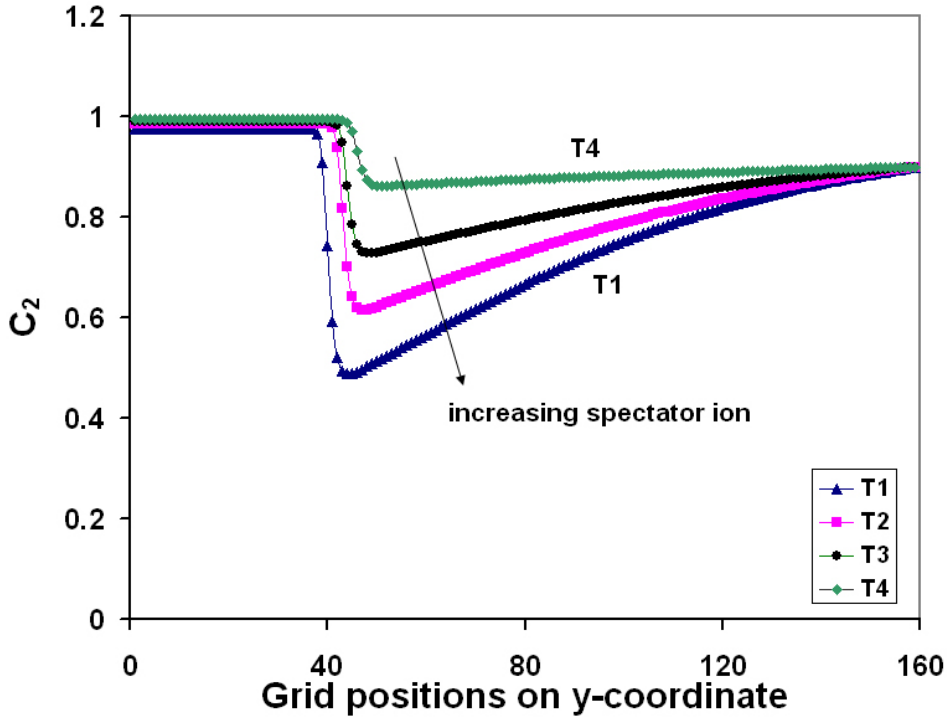

Figure 3-13: Titanium ion concentration gradient at x=0.3.

3.5 Subhalide Reduction Process

To demonstrate the use of the phase field model with electrochemistry on a metallothermic reduction process with an electrical potential map, showing the path of electrons, we study the titanium formation in the subhalide reduction process. The same governing equations as in Section 3.3 are applied to the subhalide reduction process, except that there is no applied voltage and the chemical reactants are $MgCl_2$ and $TiCl_2$.

3.5.1 Simulation Setup and Parameters

Three sets of simulations were carried out to test the consistency of our ternary model: (1) one dimensional model (open-circuit structure), (2) two-dimensional model with metals in physical contact, and (3) two-dimensional model with reactants in physical contact. The initial conditions (C_2, C_3) were set as follows: Mg(0.02, 0.98), $MgCl_2$(0.02, 0.02), $TiCl_2$(0.98,0.02), Ti (0.98, 0.98). The voltage was set to zero at the lower left pixel to couple with the electrochemical equation without imposing electrical voltage at the boundaries. The model parameters are shown in Table 3.3. These values are chosen to promote fast convergence to the solution in each iteration.

Table 3.3: Numerical parameters used in the Ti-Mg-Cl ternary system

Parameter	Numeric value
$K_{22} = K_{33}$	5×10^{-4}
$M_{22} = M_{33}$	20
σ	200 $\Omega^{-1} \cdot$ m^{-1}
σ_{e_0}	100 $\Omega^{-1} \cdot$ m^{-1}

3.5.2 Open Circuit Configuration (1D)

A one dimensional model is carried out to observe the formation of titanium by magnesiothermic reduction. The simulation domain is 5×100. The configuration is an open circuit structure where Mg is on the left and Ti is on the right separated by

$MgCl_2$ and $TiCl_2$. There is no electronic connection between metal phases. Symmetric boundary conditions are applied on the left and the right ends. Based on the free energy function of this Ti-Mg-Cl system shown in Section 3.3, two stable phases are $MgCl_2$ and Ti. Thereby, the reaction proceeds by the diffusion of reactant ions with the following half-cell reactions:

$$Mg \rightarrow Mg^{2+} + 2Cl^{-}$$

$$Ti^{2+} + 2e^{-} \rightarrow Ti.$$

Dissolution of magnesium at the $Mg/MgCl_2$ interface generates two electrons per mole of magnesium. On the $TiCl_2/Ti$ interface, formation of Ti occurs as Ti^{2+} consumes electrons. Accumulation of electrons at the $Mg/MgCl_2$ interface and positive charges at the $TiCl_2/Ti$ interface cause an electrical potential gradient across the chloride solution. As a result, this gradient eventually stops the formation of titanium since there is no medium to facilitate electron transfer from anode to cathode interface.

The results of one-dimension simulation capture the distribution of XCl_2 in the molten salt as well as electrons/cations accumulations. Figure 3-14 shows the contours of phases and voltage fields. In the beginning, diffusion in the electrolyte occurs as observed by the gradient in the concentration field. Later, the electrolyte contains more $MgCl_2$ as shown in dark blue region. The magnesium layer (red) moves left as it is dissolved, whereas the titanium layer (yellow) increases as it is formed. The steady-state concentration and electrical potential plots are shown in Figure 3-14c. The voltage on the magnesium interface is low because of electron accumulation, while that on the titanium interface is high due to excess Ti^{2+} ions.

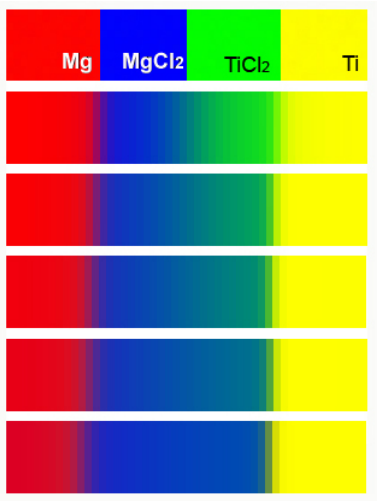

(a) Concentration contours as time increases (top to bottom).

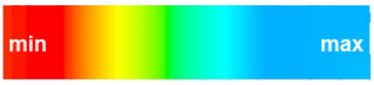

(b) Voltage contour at the final time step.

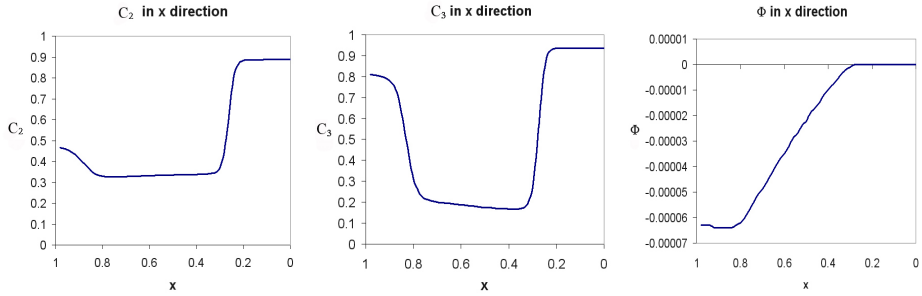

(c) Gradient plots

Figure 3-14: Steady-state solution in 1D test model. A voltage gradient is caused by electron accumulation on $Mg/MgCl_2$ interface and electron depletion on $TiCl_2/Ti$ interface.

3.5.3 Closed Circuit Configuration (2D)

Metals in Physical Contact

For two-dimensional models, the simulations are done on a 50×50 grid. Symmetric boundary conditions are applied in x and y directions. From one-dimensional configuration, connecting Mg and Ti closes the circuit. The direct contact between reactants is avoided to focus on the formation of titanium by EMR. The initial condition and outcome are shown in Figure 3-15. The reaction simulated from the ternary phase field model proceed correctly as expected. At the beginning, it is noticed that metal chloride diffusion occurs in the electrolyte. Moreover electrons from $Mg/MgCl_2$ interface can be conducted through the metal phases to $TiCl_2/Ti$ interface allowing more titanium deposition by EMR.

The evidence of EMR is observed from the voltage gradient across the metal phases: voltage is high (blue) where positive charge is produced at the $TiCl_2/Ti$ interface and low (red) where electrons are generated at the $Mg/MgCl_2$ interface. Thus electrons move from low to high potential through metal phases, allowing the reaction to proceed toward completion. Magnesium is dissolved and titanium is deposited. Not directly shown on the contour map is the diffusion of chloride ions from $TiCl_2/Ti$ interface to $Mg/MgCl_2$ interface through the molten salt due to chemical potential gradient.

Reactants in Physical Contact

To further demonstrate the mechanism of titanium formation, magnesium and $TiCl_2$ are set up to be in direct contact (see Figure 3-16). As expected, the reaction proceeds and forms titanium product at the contact interface. This titanium layer also serves as an electronic conducting path for EMR. The voltage gradient across the Ti product confirms the titanium formation by EMR after the direct contact between reactants is replaced by the deposit. On the same contour map, it is indicated that small amount of titanium formation at the lower right corner is caused by diffusion of anions and cations in the electrolyte similar to the one-dimensional case.

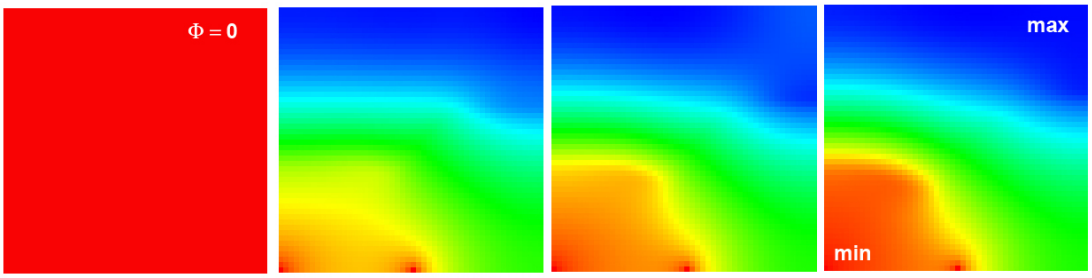

(a) Voltage field

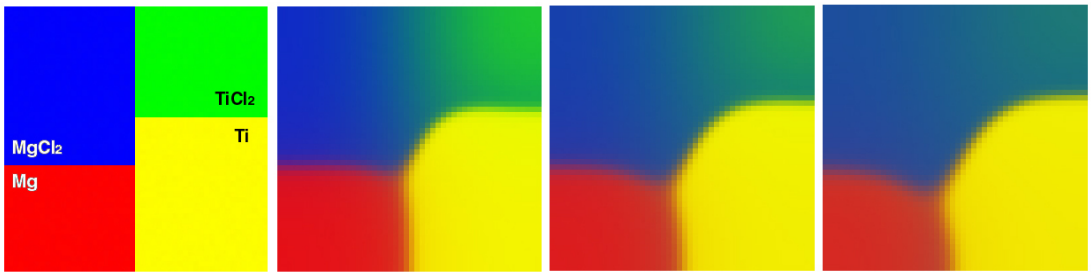

(b) Phase field

Figure 3-15: Closed circuit configuration with Ti and Mg in contact. In the voltage contour, red indicates low and blue indicates high value of voltage. Titanium formation is by reduction and by EMR. The resolution is 50×50.

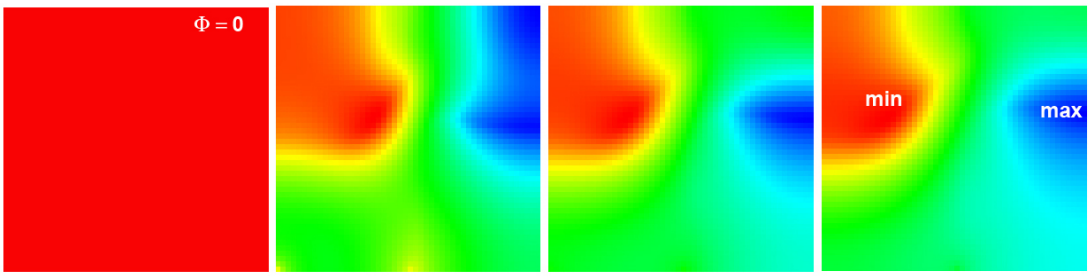

(a) Voltage field

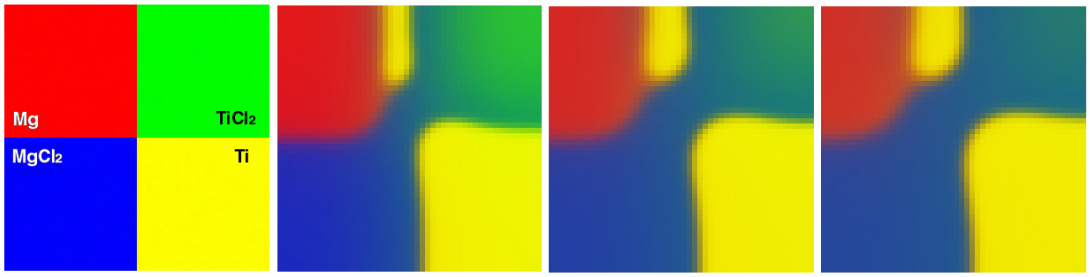

(b) Phase field

Figure 3-16: Two dimensional model with Mg and $TiCl_2$ in contact. Titanium is first formed at the Mg/$TiCl_2$ interface. More titanium plating may also proceed by EMR as indicated by the change in voltage across the titanium. The resolution is 50x50.

3.5.4 Blocking Chemical Reduction and Promoting EMR

To enhance the formation of titanium by EMR, the direct physical contact between Mg and $TiCl_2$ has to be minimized or eliminated. A test run is done on a simple configuration of a three-layer structure (top: $TiCl_2$-$MgCl_2$-Mg: bottom) and a small titanium seed on one side. Figure 3-17 displays the phase field evolution (first, third, and fifth rows) and the diffusion path (second, fourth, and sixth rows). From these results, three mechanisms are observed. First, titanium formation occurs by EMR due to movement of electrons from Mg-$MgCl_2$ interface through titanium to Ti-$TiCl_2$ interface. Later, diffusion of $TiCl_2$ reaches the magnesium layer and titanium nuclei form on the magnesium/electrolyte layer. These nuclei continue to grow. Until magnesium is all reacted, the system enters a two phase region (electrolyte/titanium tieline). Finally, the small particles become coarsen.

These simulations suggest that magnesiothermic reduction is delayed when the direct contact between the reactants is blocked. However, since $TiCl_2$ can diffuse into the blocking layer, titanium particles still form spontaneously. All of these observation can be used to understand the basic phenomena that occur in this system and to help design the experimental study.

3.6 Summary

The binary phase field model for electrochemistry has been extended to a ternary system with focus on the solid-solid interface. The simulation models are applied to study the morphology and mechanisms of titanium formation in two classes of extraction process, which are electrolysis and metallothermic reduction. In the Ti-Mg-halide ternary system, surface tension depends on metal and electrolyte composition and increases with magnesium content.

First, two dimensional results of a perturbed interface without convection for a titanium electrolytic system demonstrate that there exists a titanium ion concentration gradient at the cathode front. This gradient is steeper at the tip of the dendrite. Moreover, the metal ion concentration gradient depends on the amount of supporting

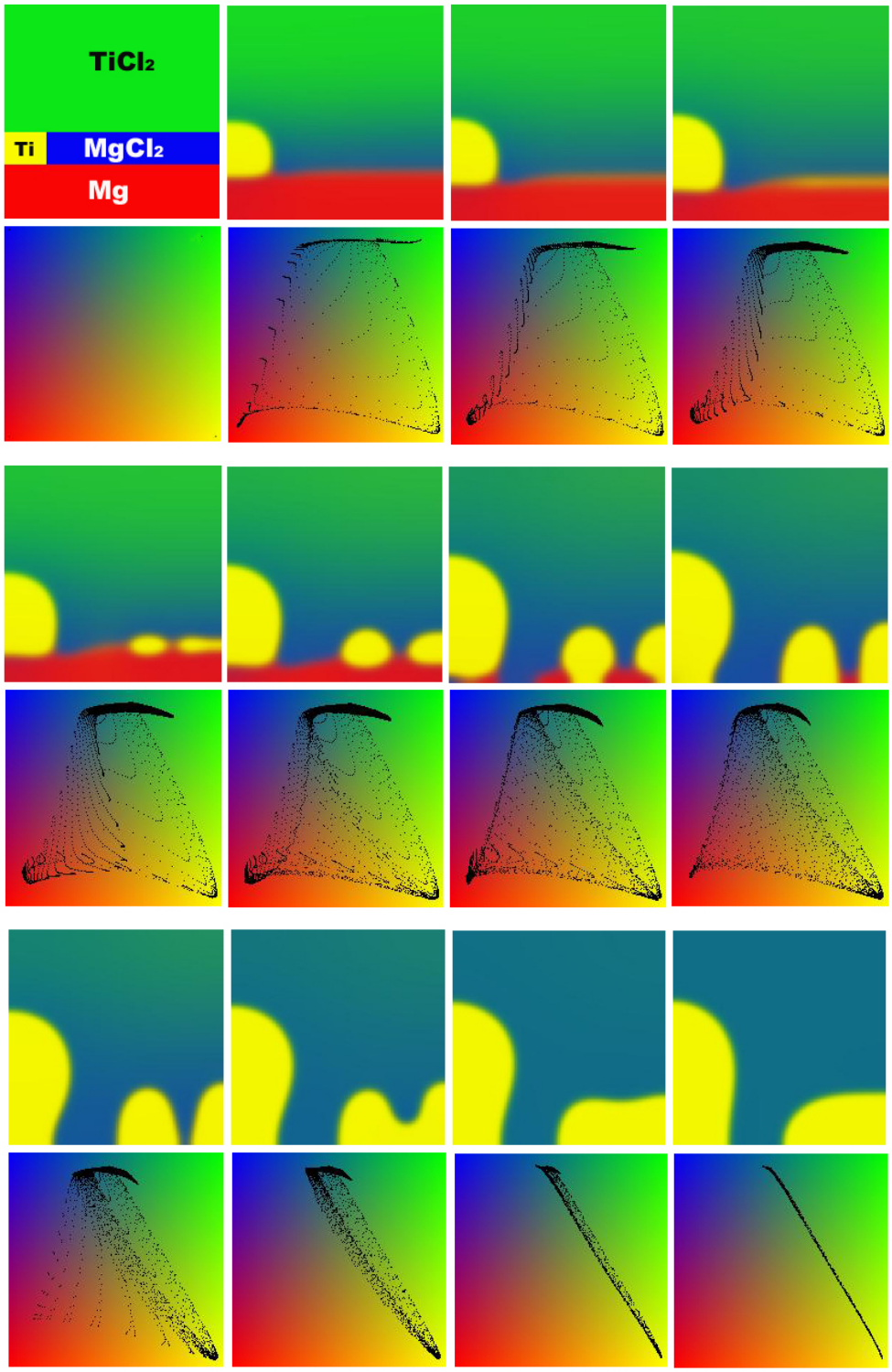

Figure 3-17: Phase contours and diffusion path maps showing formation of titanium by EMR in the early stage, nucleation and growth after $TiCl_2$ diffuse to magnesium, and coarsening after magnesium is completely dissociated. (From left to right and top to bottom)

electrolyte. At a constant applied field, the more supporting electrolyte leads to a more unstable interface due to an increase in the metal ion concentration gradient. At a high Peclet number, the interface is always unstable regardless of spectator ion concentration due to electric field. These behaviors match the linear stability theory reported in the literature.

The second study focuses on the subhalide reduction process. The mechanisms of magnesiothermic reduction of titanium are investigated. The preliminary results in one and two dimensions are in good qualitative agreement with the reaction pathway summarized in the literature. The phase field model depicts the location and the topology of the reaction, such as the voltage gradient and diffusion gradient. This model can be used to explore the initial setup that could lead to better control of the system on the morphology of the cathode deposits.

In summary, these two studies demonstrate the ability of this phase field formulation to automatically describe how the free energy description of a system leads to complex emergent electrochemical behavior in the mass transport-limited regime.

Chapter 4

Transport Phenomena Models in the SOMERC Process

Based on the review of titanium extraction processes in the previous chapter, there are several technical challenges to be solved. A summary of advantages and drawbacks of the processes described above is listed in Table 4.1.

Table 4.1: Comparisons among the emerging reduction technologies reviewed in this chapter

Process	Process-type	Capital cost	Raw material	Product	Harmful reactants/by-products
Kroll	× Batch	× High	× $TiCl_4$ (gas)	× Sponge	×Cl_2 (gas)
FFC	○ Semi-continuous	○ Low	○ TiO_2 (solid)	× Sponge	○ None
OS	○ Semi-continuous	○ Low	○ TiO_2 (solid)	× Sponge	○ None
MER	× Batch	○ Low	○ TiO_2 (solid)	× Sponge	○ None
Ginatta	○ Continuous	× High	× $TiCl_4$ (liq)	○ Liquid	×Cl_2 (gas)

The ideal extraction process for titanium should have the following characteristics:

- The process should be continuous with low capital cost.

- The use of chlorides should be avoided because their volatility make composition control very difficult.

- TiO_2 should be utilized as a raw material to avoid use of chlorine gas and possible dioxin production.

- Electrolysis should be employed instead of metallothermic reduction to avoid requiring a separate process for electrolysis of magnesium or other reductant.

- The process should produce dense solid titanium to avoid both the need for sponge or dendrite consolidation and also problems associated with extremely reactive liquid titanium.

- If possible, the process should allow for supplementing electrical power with carbon-based fuel to reduce energy costs, though care must be taken to avoid carbon contamination of the product.

Based on the above features, electrolytic route has several characteristics that are advantageous. A major drawback is the sponge formation due to electrochemical instability. To improve this aspect of electrolytic processes, the formation of dendrite should be suppressed. In this part of the thesis, we investigate a new electrolytic smelting of titanium proposed together with Pal [24], which has a rotating cathode to create shear flow during the process. The objective of this project is to examine the technical challenges in such a process. Numerical models will be developed to analyze the transport phenomena near the cathode interface. A plan of the phase field model of the titanium solid cathode morphology under shear from liquid electrolyte is outlined for future study.

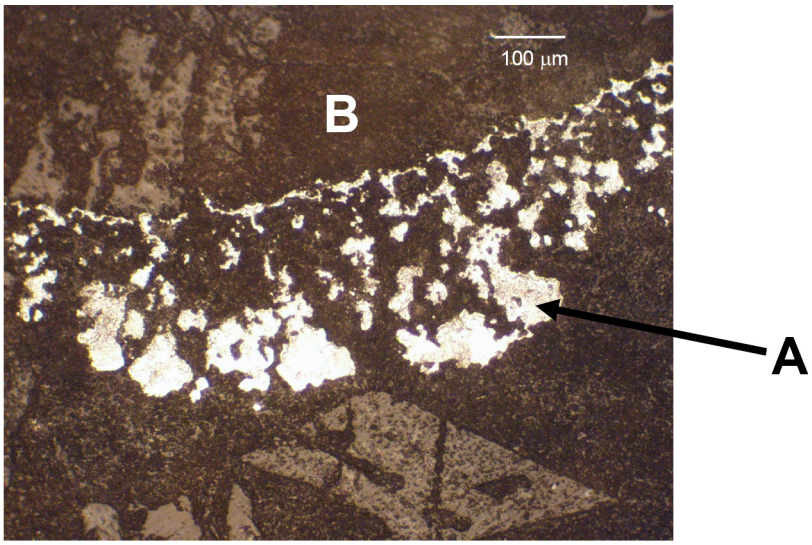

Figure 4-1: Titanium deposit (A) near the cathode (B) from the electrolysis of TiO_2 using SOM tube containing liquid tin anode [24].

4.1 Solid Oxide Membrane Electrolysis with Rotating Cathode Process

Uday Pal at Boston University has developed Solid Oxide Membrane (SOM) technology as an anode for electrolytic processes such as direct reduction of magnesium [45], tantalum [46] from their oxides, and deoxidation of liquid copper [47]. Currently, a single-cell experiment using a SOM anode is being tested for the electrolysis of titanium dioxide [24]. The operating temperature is chosen to be 1150 °C. Molten salt solution contains MgF_2 and CaF_2, which form a eutectic system. Then titanium oxide is added to the electrolyte. The SOM anode is a Yttria-Stabilized-Zirconia (YSZ) tube containing either liquid tin connected to a molybdenum anode or molten salt flux connected to a carbon anode. Titanium deposits at the cathode are observed as shown in Figure 4-1. With this potential technology, it is interesting to develop a new titanium electrolytic process for continuous production of dense ingots directly from low-cost titanium oxides by means of SOM-encased anode.

We propose a new process, called Solid Oxide Membrane Electrolysis with Rotating Cathode (SOMERC). The goal of this proposed design is the production of large

ingots of commercial purity (CP) titanium directly from low-purity TiO_2 in molten salt with oxyide-ion conducting anodes. The system consists of a rotating titanium primary cathode at the center of a crucible, a barrier or secondary cathode at lower potential, several solid oxide membrane-encased anodes around the outer region, and a molten salt electrolyte (flux). The cathode cylinder can be placed vertically as shown in Figure 4-2 or horizontally as shown in Figure 4-3.

At the inner region, the primary cathode is rotated to increase the shear flow around the growing titanium. With this high shear force at the cathode, the higher upwind mass transfer coefficient is expected to cause perturbations to shift along the surface or decay instead of growing into dendrites. This prediction is analogous to the observation discovered by Flemings research group that semi-solid metal nuclei can grow as spheroids without forming dendrites under sufficient shear force at the early stage of the process [48]. Another evidence of dendrite suppression by shear has been observed in electrolytic polymerization of pyrrole where shear force is created by strong magnetic field and ionic current in the electrolyte [49]. In this SOMERC process, shear flow can be produced by a vertical or horizontal rotating cathode. At the same rotating speed, the vertical rotation creates less shear with a uniform boundary layer, whereas, the horizontal rotation produces higher shear with a non-uniform boundary layer.

The inner and outer region are separated by a semi-permeable barrier. This barrier not only shields the fragile SOM anodes from highly turbulent flow at the inner region, but also acts as a secondary cathode. By connecting the barrier at lower potential than the primary cathode, other more electronegative ions (i.e., Fe^{n+} and Ni^{n+}) in the impure TiO_2 would be reduced at the secondary cathode. The less electronegative ions in molten salts and zirconia tube (i.e., Na^{+}, Ca^{2+}, Mg^{2+}, and Zr^{4+}) will not be reduced.

At the outer region, the SOM anodes are placed around the crucible. The cross-section view of an anode is also shown in Figure 4-2. Due to the excellent oxide ions conductivity of YSZ, the reduction from Ti^{4+} to titanium is expected to be achieved in one step without Ti^{2+}, Ti^{3+} ions cycling problem. However, the single-

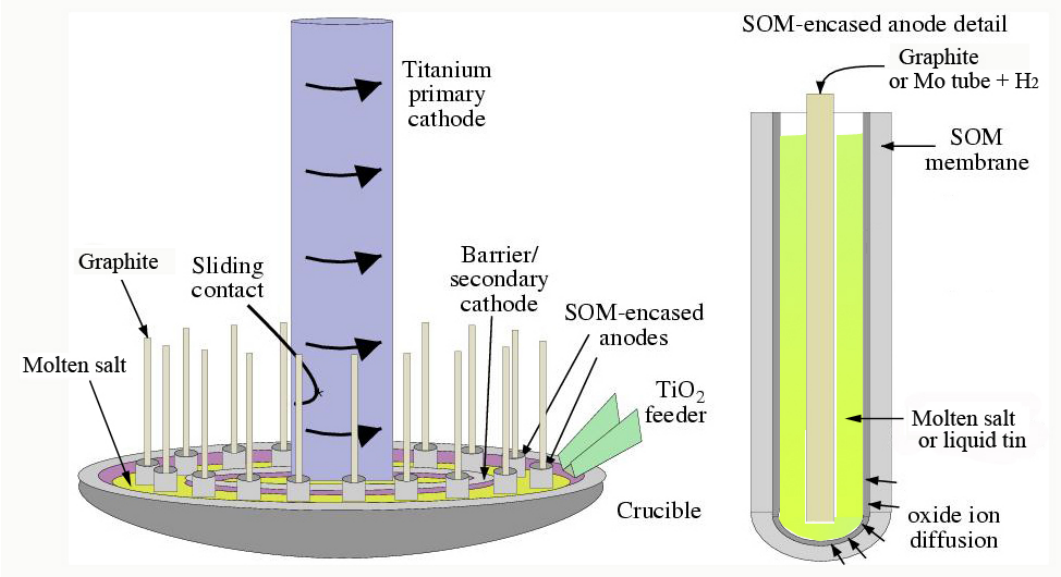

Figure 4-2: A cell design of the SOMERC process. The left figure represents a vertical rotating cathode system. The right figure shows the components of SOM anode.

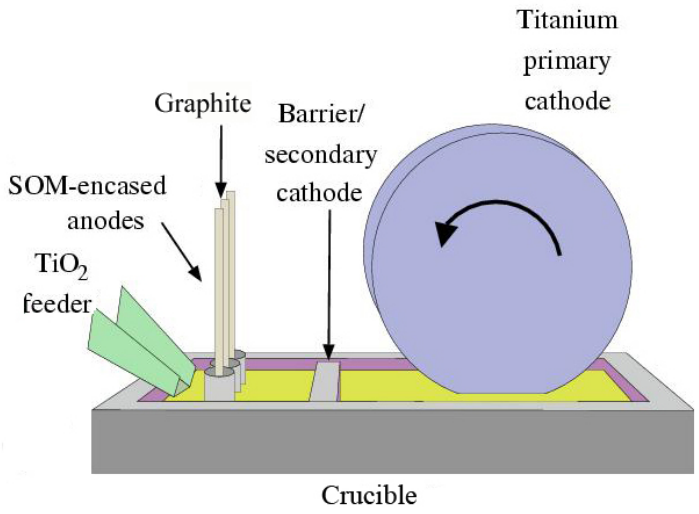

Figure 4-3: A cell design of the SOMERC process with a horizontal rotating cathode.

cell experimental results showed some evidence of lower valence formation [24]. If the inner crucible is made of Ti, it can reduce Ti^{4+} to the lowest valence ion Ti^{2+}, before entering the inner crucible. To further improve the reduction of Ti^{4+}, Fe^{n+} and Ni^{n+}, some titanium scrap can also be added to the outer region. Also at the outer region, titanium dioxide is added to supply the titanium ions in the system making it a continuous process.

Our transport dynamics models are focused on rotational flow near the primary cathode because it is directly related to the morphology of the titanium product. Thus, the simulation domains are located in the inner crucible in this study.

4.2 Transport Phenomena near the Rotating Cathode

This section presents the derivation and results from a the computational flow models that describe different transport phenomena in the SOMERC process. To estimate the shear forces produced by different rotating speeds, two computational flow models were studied. These flow models uses the velocity-vorticity formulation, instead of the velocity-pressure formulation. In the vertical rotating axis case, benchmark tests are performed based on Czochralski crystal growth process, which has a similar configuration consisting of a rotating silicon ingot in the silicon melt. After that, mass transport is included. In the horizontal rotating axis case, a test is performed at low Reynolds number near the Stokes flow regime. Shear forces near the cathode as a function of rotational speed are obtained for each case.

Important assumptions in fluid flow models are listed below:

1. All oxide ions are removed at the anode in the outer region. Thus there is no oxide ions in the inner crucible.

2. All Ti^{4+} ions are reduced by the secondary cathode to Ti^{2+} in the outer region. Only Ti^{2+} ions get into the inner region.

3. Inner crucible contains only MgF_2 and TiF_2.

4. Uniform density, viscosity, and diffusivity are assumed.

5. Gravitational force is neglected.

4.2.1 Vertical Rotational Flow Model

The vertical rotating cathode configuration is similar to that of the Czochralski crystal growth, in which transport of momentum, heat, and solutes is well developed [50, 51, 52]. This flow model is considered as axisymmetric, which can be simulated on a two-dimensional domain.

Transport Phenomena Formulations in Cylindrical Coordinates

The Navier-Stokes equation is usually defined in velocity-pressure form which is complicated to solve numerically because of the need for a staggered grid and the stiffness of the linearized system of equations. To eliminate this complication, the velocity-vorticity formulation is used. Vorticity ω is defined as

$$\omega = \nabla \times \overrightarrow{U} = \frac{\partial u}{\partial z} - \frac{\partial w}{\partial r} \tag{4.1}$$

where $\overrightarrow{U} = (u, v, w)$ which are velocities in r, θ, z directions, respectively. The continuity equation is expressed by

$$\frac{1}{r}\frac{\partial}{\partial r}(ru) + \frac{\partial w}{\partial z} = 0. \tag{4.2}$$

By taking the derivatives of Equation 4.2 with respect to r and z separately and rearranging each equation in terms of vorticity, we can write the vorticity form of continuity equation as:

$$\nabla^2 u - \frac{\partial \omega}{\partial z} - \frac{u}{r^2} = 0 \tag{4.3}$$

$$\nabla^2 w + \frac{1}{r}\frac{\partial}{\partial r}(r\omega) = 0. \tag{4.4}$$

The velocity-pressure momentum equations are normalized by defining nondimen-

sional parameters:

$$(\tilde{r}, \tilde{z}) = \frac{(r, z)}{R}, \tag{4.5}$$

$$(\tilde{u}, \tilde{v}, \tilde{w}) = \frac{(u, v, w)}{(\upsilon/R)}, \tag{4.6}$$

$$\tilde{P} = \left(\frac{\rho\upsilon^2}{R^2}\right) P - \rho R g z, \tag{4.7}$$

$$\tilde{T} = \frac{T - T_{cathode}}{T_{anode} - T_{cathode}}, \tag{4.8}$$

where g is the gravitational acceleration $[m/s^2]$, R is the characteristic length $[m]$, υ is the kinematic viscosity $[m^2/s]$, P is pressure $[N/m^2]$, T is temperature $[K]$.Thus the dimensionless momentums equation are:

$$\frac{\partial\tilde{u}}{\partial\tilde{t}} + \tilde{u}\frac{\partial\tilde{u}}{\partial\tilde{r}} + \tilde{w}\frac{\partial\tilde{u}}{\partial\tilde{z}} - \frac{\tilde{v}^2}{\tilde{r}} = -\frac{\partial\tilde{P}}{\partial\tilde{r}} + \tilde{\nabla}^2\tilde{u} - \frac{\tilde{u}}{\tilde{r}^2}, \tag{4.9}$$

$$\frac{\partial\tilde{w}}{\partial\tilde{t}} + \tilde{u}\frac{\partial\tilde{w}}{\partial\tilde{r}} + \tilde{w}\frac{\partial\tilde{w}}{\partial\tilde{z}} = -\frac{\partial\tilde{P}}{\partial\tilde{z}} + \tilde{\nabla}^2\tilde{w} + Gr\tilde{T}, \tag{4.10}$$

$$\frac{\partial\tilde{v}}{\partial\tilde{t}} + \tilde{u}\frac{\partial\tilde{v}}{\partial\tilde{r}} + \tilde{w}\frac{\partial\tilde{v}}{\partial\tilde{z}} + \frac{\tilde{u}\tilde{v}}{\tilde{r}} = \tilde{\nabla}^2\tilde{v} - \frac{\tilde{v}}{\tilde{r}^2}. \tag{4.11}$$

Gr is the Grashof number which is a ratio of the buoyant force to the viscous force acting on the fluid ($Gr = \frac{g\beta_T\Delta T R^3}{\upsilon^2}$). In this expression, β_T is the coefficient of volumetric thermal expansion of the fluid $[K^{-1}]$. Therefore when $Gr \gg 1$, flow is dominated by natural convection (*i.e.,* convection driven by temperature gradient) and when $Gr \ll 1$ natural convection is negligible.

Then differentiating Equation 4.9 with respect to z and Equation 4.10 with respect to r get

$$\frac{\partial}{\partial\tilde{z}}\left(\frac{\partial\tilde{u}}{\partial\tilde{t}} + \tilde{u}\frac{\partial\tilde{u}}{\partial\tilde{r}} + \tilde{w}\frac{\partial\tilde{u}}{\partial\tilde{z}} - \frac{\tilde{v}^2}{\tilde{r}}\right) = -\frac{\partial^2\tilde{P}}{\partial\tilde{r}\partial\tilde{z}} + \frac{\partial}{\partial\tilde{z}}\left(\tilde{\nabla}^2\tilde{u} - \frac{\tilde{u}}{\tilde{r}^2}\right) \tag{4.12}$$

$$\frac{\partial}{\partial\tilde{r}}\left(\frac{\partial\tilde{w}}{\partial\tilde{t}} + \tilde{u}\frac{\partial\tilde{w}}{\partial\tilde{r}} + \tilde{w}\frac{\partial\tilde{w}}{\partial\tilde{z}}\right) = -\frac{\partial^2\tilde{P}}{\partial\tilde{r}\partial\tilde{z}} + \frac{\partial}{\partial\tilde{r}}\left(\tilde{\nabla}^2\tilde{w} + Gr\tilde{T}\right). \tag{4.13}$$

Next, subtracting Equation 4.13 from Equation 4.12 and then rewriting in terms of

ω yields

$$\frac{\partial\tilde{\omega}}{\partial\tilde{t}} + \overrightarrow{U}\cdot\tilde{\nabla}\tilde{\omega} - \frac{\partial}{\partial\tilde{z}}\left(\frac{\tilde{v}^2}{\tilde{r}}\right) = \nabla^2\tilde{\omega} - \frac{\tilde{\omega}}{\tilde{r}^2} - Gr\frac{\partial\tilde{T}}{\partial\tilde{r}}, \tag{4.14}$$

where $\overrightarrow{U}$ is the velocity vector ($\tilde{u}$, $\tilde{w}$).

Other variables that need to be solved are temperature ($\tilde{T}$), and concentration of diffusing species ($\tilde{C}_i$). The dimensionless energy equation is:

$$\frac{\partial\tilde{T}}{\partial\tilde{t}} + \tilde{u}\frac{\partial\tilde{T}}{\partial\tilde{r}} + \tilde{w}\frac{\partial\tilde{T}}{\partial\tilde{z}} = \frac{1}{Pr}\tilde{\nabla}^2\tilde{T}. \tag{4.15}$$

Pr is the Prandlt number which is a ratio of kinematic viscosity to thermal diffusivity κ_T ($Pr = \frac{\upsilon}{\kappa_T}$)

Dimensionless concentration of diffusing species is in mole fraction such that $\tilde{C}_i = \frac{C_i}{C_t otal}$. Here, only the mixture of chlorides are modeled, thus C_3 is zero. Magnesium and titanium ions can be represented by one parameter, C_2. The dimensionless equations are

$$\frac{\partial\tilde{C}_2}{\partial\tilde{t}} + \tilde{u}\frac{\partial\tilde{C}_2}{\partial\tilde{r}} + \tilde{w}\frac{\partial\tilde{C}_2}{\partial\tilde{z}} = \frac{1}{Sc}\tilde{\nabla}^2\tilde{C}_2, \tag{4.16}$$

$$\tag{4.17}$$

where Sc is the Schmidt number which is analogous to Prandtl number for mass transfer.

Finally, at steady state, the time derivative terms go to zero. Thus, we can solve for each field variable from:

$$0 = \tilde{\nabla}^2\tilde{u} - \frac{\partial\tilde{\omega}}{\partial\tilde{z}} - \frac{\tilde{u}}{\tilde{r}^2} \tag{4.18}$$

$$0 = \tilde{\nabla}^2\tilde{w} + \frac{1}{\tilde{r}}\frac{\partial}{\partial\tilde{r}}(\tilde{r}\tilde{\omega}) \tag{4.19}$$

$$0 = \tilde{\nabla}^2\tilde{v} - \tilde{u}\frac{\partial\tilde{v}}{\partial\tilde{r}} - \tilde{w}\frac{\partial\tilde{v}}{\partial\tilde{z}} - \frac{\tilde{v}}{\tilde{r}^2} - \frac{\tilde{u}\tilde{v}}{\tilde{r}} \tag{4.20}$$

$$0 = \tilde{\nabla}^2\omega - \tilde{u}\frac{\partial\tilde{\omega}}{\partial\tilde{r}} - \tilde{w}\frac{\partial\tilde{\omega}}{\partial\tilde{z}} - \frac{\tilde{\omega}}{\tilde{r}^2} - Gr\frac{\partial\tilde{T}}{\partial\tilde{r}} + \frac{\partial}{\partial\tilde{z}}\left(\frac{\tilde{v}^2}{\tilde{r}}\right) \tag{4.21}$$

$$0 = \tilde{\nabla}^2\tilde{T} - Pr\left(\tilde{u}\frac{\partial\tilde{T}}{\partial\tilde{r}} + \tilde{w}\frac{\partial\tilde{T}}{\partial\tilde{z}}\right) \tag{4.22}$$

$$0 \;=\; \tilde{\nabla}^2 \tilde{C}_2 - Sc\left(\tilde{u}\frac{\partial \tilde{C}_2}{\partial \tilde{r}} + \tilde{w}\frac{\partial \tilde{C}_2}{\partial \tilde{z}}\right) \tag{4.23}$$

where $\tilde{\nabla}^2 = \frac{1}{\tilde{r}}\frac{\partial}{\partial \tilde{r}}\left(\tilde{r}\frac{\partial}{\partial \tilde{r}}\right) + \frac{\partial^2}{\partial \tilde{z}^2}$. These governing equations are converted into finite difference equations. The first and second derivatives are estimated based on central difference scheme. The convective terms are calculated by upwinding finite different scheme.

Boundary Conditions and Initial Conditions

We start with a benchmark problem as presented by Wheeler [53] and compare the numerical results to Xu *et al.* [50]. Then we add ion transport and electrical potential across the electrodes. A schematic drawing of the simulation domain is illustrated in Figure 4-4.

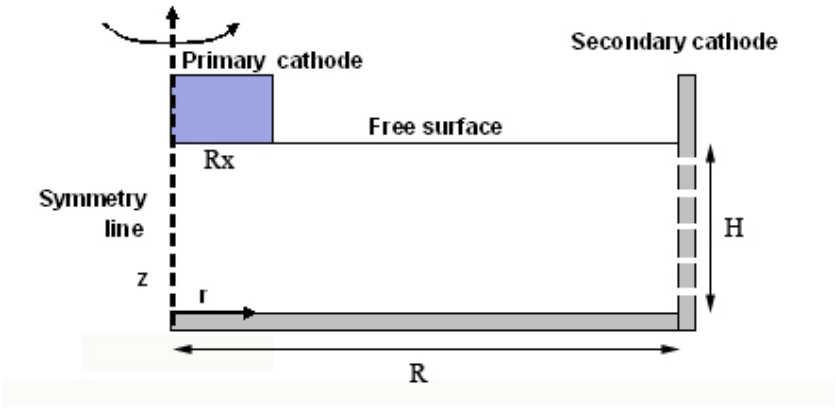

Figure 4-4: Two-dimensional simulation domain for the SOMERC's inner crucible with vertical rotating cathode.

The crucible radius is R, which is the characteristic length of this system. Cathode radius is R_x. The depth of the electrolyte is H. The angular velocity of the cathode is Ω [rad/s].

The mathematical form of boundary conditions can be expressed as follow:

at the crucible wall: $\tilde{r} = 1$, $0 \leq \tilde{z} \leq H/R$

$\tilde{u} = \tilde{w} = \tilde{v} = 0$, $\tilde{\omega} = \frac{\partial \tilde{w}}{\partial \tilde{r}}$, $\tilde{T} = \tilde{C}_2 = 1$,

at the bottom: $0 \leq \tilde{r} \leq 1$, $\tilde{z} = 0$

$\tilde{u} = \tilde{w} = \tilde{v} = \frac{\partial \tilde{T}}{\partial \tilde{z}} = \frac{\partial \tilde{C}_2}{\partial \tilde{z}} = 0,$

at the centerline (symmetric): $\tilde{r} = 0$, $0 \leq \tilde{z} \leq H/R$

$\tilde{u} = \tilde{v} = \frac{\partial \tilde{w}}{\partial \tilde{r}} = \tilde{\omega} = \frac{\partial \tilde{T}}{\partial \tilde{r}} = \frac{\partial \tilde{C}_2}{\partial \tilde{r}} = 0,$

at the cathode surface: $0 \leq \tilde{r} \leq R_x/R$, $\tilde{z} = H/R$

$\tilde{u} = \tilde{w} = \tilde{T} = \tilde{\Phi} = 0$, $\tilde{v} = rRe_x$, $\tilde{\omega} = \frac{\partial \tilde{u}}{\partial \tilde{z}} = C_2 = 0,$

at the free surface: $R_x/R \leq \tilde{r} \leq 1, \tilde{z} = H/R$

$\frac{\partial \tilde{u}}{\partial \tilde{z}} = \frac{\partial \tilde{v}}{\partial \tilde{z}} = \tilde{w} = 0, \tilde{T} = \tilde{C}_2 = \tilde{\Phi} = \frac{(\tilde{r} - R_x/R)}{(1 - R_x/R)}.$

Re_x is the Reynolds number written in terms of dimensionless angular velocity of the rotating cathode ($\frac{\Omega R^2}{\upsilon}$).

At the crucible wall, we assume no-slip condition with constant temperature, inlet flux of anions, and outlet flux of cations. Vorticity depends only on z-velocity. At the bottom, a no-slip, constant temperature, and zero ion fluxes conditions are applied . So vorticity is only the z derivative of r-velocity. At the center line, a symmetric boundary condition is applied to z-velocity, temperature, and ion concentrations. Other fields are zero. On the top in the cathode region, no-slip condition is applied. Consequently, vorticity is only a function of r-velocity. There is zero thermal flux across the cathode surface. The concentration of titanium ion is zero in the cathode vicinity due to ion depletion and production of magnesium ions. Finally, on the free surface, no-shear boundaries are applied to r-velocity and θ-velocity. It is assumed that the fluid surface is flat, leading to zero z-velocity. In addition, linear distributions of temperature and concentration are applied to the free surface.

Newton-Raphson iterations begins with zero momentum, constant ion concentrations, and linear temperature gradient for a steady-state model.

Benchmark Results of Czochralski Fluid and Heat Flow

Benchmark simulations are carried out for three cases (A1, A2, and D2) [53]. Case A1 has forced convection at Re_x=100 and no thermal convection Gr=0. Case A2 also has only forced convection with Re_x=1000. Case D2 includes both forced convection and strong natural convection (Re_x=100 and Gr=10^5). To get better results, finer grid resolutions are used, including 80×80, 160×160, and 320×320. Prandtl number

for simulating silicon melt is 0.05. Table 4.2 shows the results from our model.

Table 4.2: Comparison to the results done by Xu *et al.* [50]

Case	Re	Gr	$\lvert U_{max}\rvert^a$	$\lvert U_{max}\rvert^b$	$\lvert U_{max}\rvert^c$
A1	100	0	4.37	5.22	4.69
A2	1000	0	88.79	183.55	92.31
D2	100	10^5	190.12	231.98	228.33

[a]80×80 (non-uniform grids): Second order upwind QUICK scheme by Xu *et al.*
[b]80×80 (uniform grids): Present model using finite difference.
[c]320×320 (uniform grids): Present model using finite difference.

The magnitudes of the maximum dimensionless velocity in the $r-z$ plane ($|U_{max}|$) from our velocity-vorticity model are larger compared to those reported in the literature. For case A1 with low Re, U_{max} obtained at 320×320 uniform grid differs from the reported value by 0.32 or 7.32%. For case A2 with higher Re, the difference is 3.52 or 3.96%. For case D2 with high Gr, our model indicates 20% higher value compared to the published results. The main reason is because their second order upwind QUICK scheme is more robust. A non-uniform grid also uses less computational resources, while preserves the accuracy. However, solving a steady state equations do not require too long run time on higher uniform grid resolutions. Thus, our simpler velocity-vorticity model is sufficient to simulate a system with no significant thermal convection.

The flow fields can also be compared to the benchmark results done by Ermakov [54]. In his model, the finite volume method is used to solve the velocity-pressure Navier-Stokes equations and energy equation. The simulation used software named COMGA (COvection in MicroGravity and Applications) developed by the author [54]. Figure 4-5 illustrates the contour plots of case A1, A2, and D2. It should be noted that the color conventions are opposite: our model denotes blue as positive or maximum and red as negative or minimum, and vice versa for COMGA. For case A1, there is only forced convection, thus the flow is in the clockwise direction. For case A2, the velocity boundary layer is thinner due to higher rotation speed. For case D2,

natural convection causes the high temperature fluid to flow upward near the heated crucible wall, thereby the flow is counterclockwise.

Based on a comparison of the contour plots, our model correctly represents the flow profile, direction, and location of maximum and minimum for each field variable. This model can thus be used to observe the boundary layer thicknesses of the system in response to different rotation speeds, despite the issue of velocity overestimation.

SOMERC Macroscopic Fluid and Mass Flow Results

After the model has been validated, SOMERC flow simulations are carried out. The temperature in the system is roughly uniform due to vigorous stirring, thus natural convection is not included in this model. The simulation parameters of the Ti-Mg-F system are listed in Table 4.3. When physical properties are not available, the values are approximated from typical molten salt properties. The crucible radius is 0.2 m, filled with molten fluoride salts up to 0.1 m. The cathode radius is 0.05 m.

Table 4.3: Parameters used in Ti-Mg-F system simulations.

Properties	Value	Note
R_x	0.05 m	
$R \times H$	0.2 m×0.1 m	
ρ	2.37×10^3 kg/m^3	[55]
η	2.7×10^{-3} Ns/m^2	[56]
D	10^{-8} m^2/s	Approx.
Sc	114	

Boundary Layer Thicknesses Ratio The diffusion and viscous boundary layer thicknesses are compared. For rotating disk flow, the velocity boundary layer is a function of the rotation rate ($\delta_u \sim \sqrt{\upsilon/\Omega}$ or $\sqrt{R^2/Re}$). An example of flow profiles with $Re = 100$ at 240×120 resolution are shown in Figure 4-6. The boundary layer for velocity can be observed from the vorticity contour. Underneath the cathode,

Our finite difference results

COMGA finite volume method

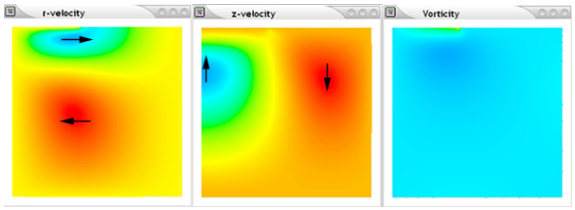

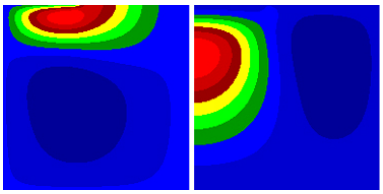

(a) Case A1: Re_x=100, Gr=0

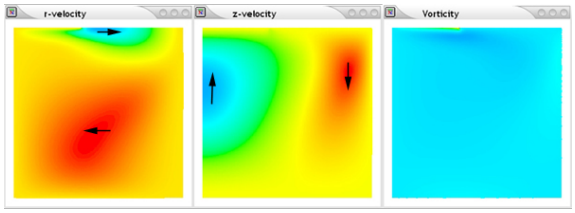

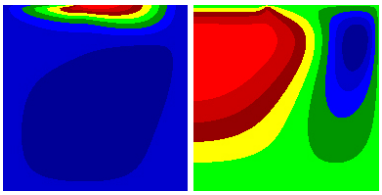

(b) Case A2: Re_x=1000, Gr=0

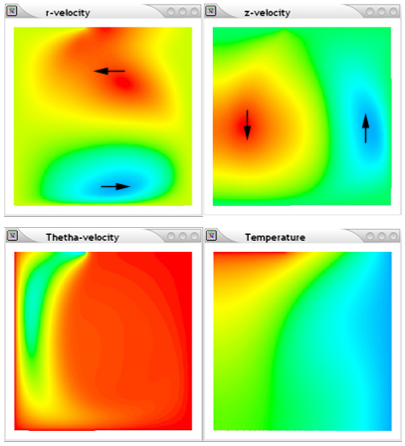

(c) Case D2: Re_x=100, Gr=10^5

Figure 4-5: Benchmark results. Left: Finite difference results (Blue=max). Right: Finite volume scheme results from COMGA (Red=max) [54].

the viscous boundary layer produced by vertical rotation appears to be uniform. The concentration boundary layer is also uniform and extremely small due to high Schmidt number for this test run case.

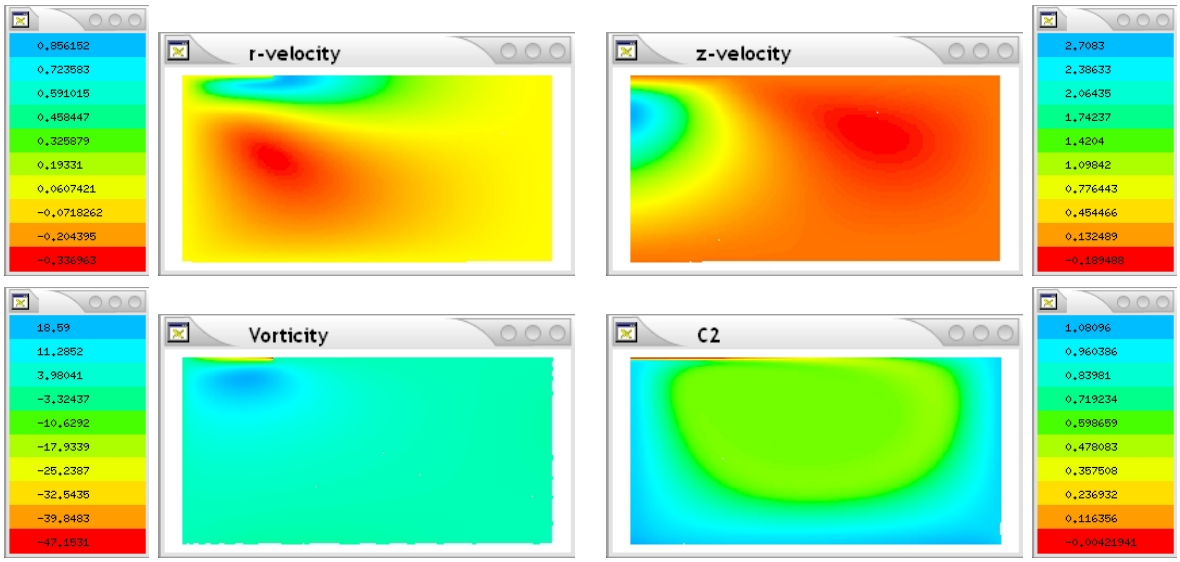

Figure 4-6: Contours for Re=100 and Sc=5000. The viscous boundary layer thickness is 0.022 m. The diffusion boundary layer is 0.004 m. Grid resolution is 240 × 120.

In the limit of high Schmidt number, the relationship between the two boundary layer thicknesses goes as:

$$\frac{\delta_c}{\delta_u} = kSc^{-1/3}, \tag{4.24}$$

where k is the proportionality constant. The result from our model is shown in Figure 4-7. From this model, the viscous or velocity boundary layer thickness is $2.75\sqrt{R^2/Re}$. The ratio of the two boundary layer thicknesses follows Equation 4.2.1 with $k = 21.72$. A thinner mass-transfer boundary layer leads to a higher deposition rate.

Shear Strain Rate as a Function of Reynolds Number The shear strain rate produced by vertical rotation can be calculated from the velocity near the cathode. From the simulation, the shear strain rate ($\frac{\partial u}{\partial z}$) near the edge of the rotating cathode ($r = 0.2R$) is computed and plotted as a function of Re as illustrated in Figure 4-8. The result shows that higher Re number produces higher deformation rate.

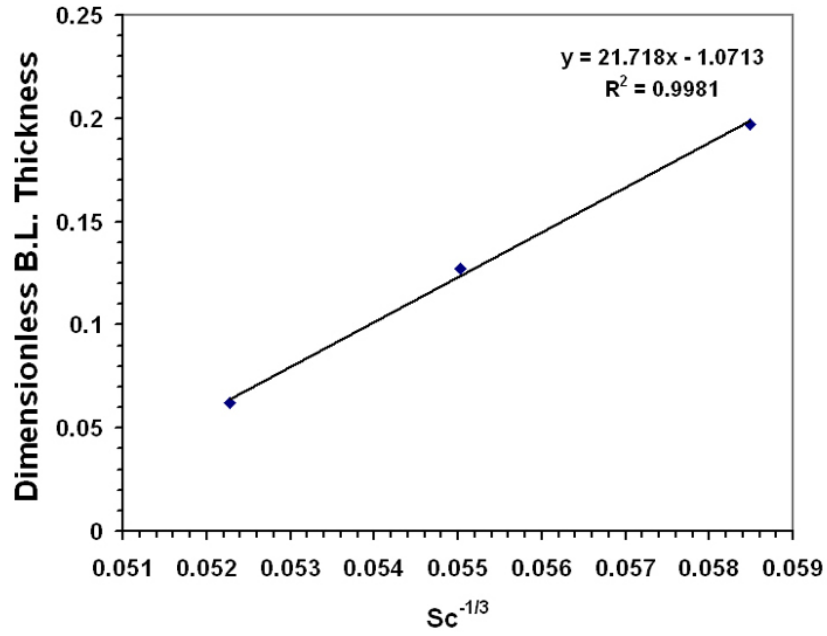

Figure 4-7: Dimensionless boundary layer thickness ($\frac{\delta_c}{\delta_u}$) as a function of $Sc^{-1/3}$.

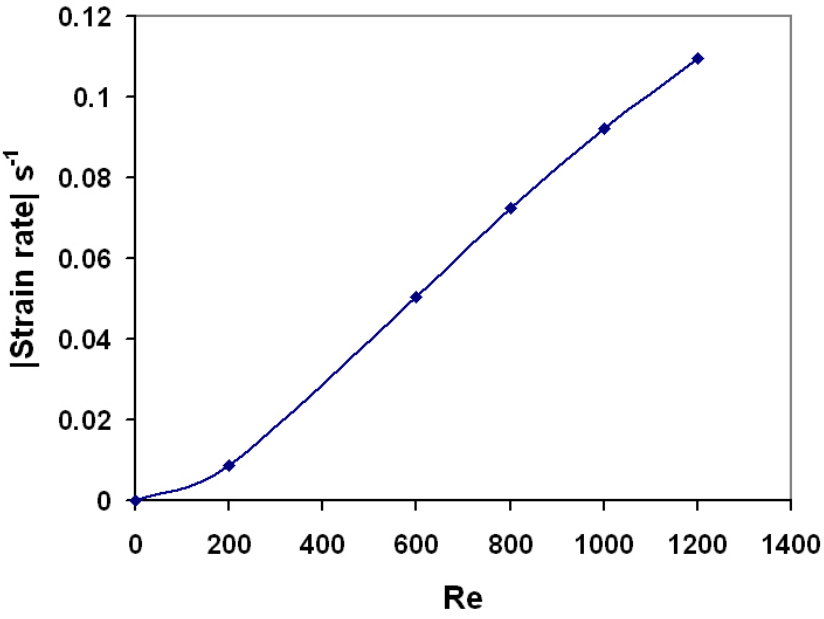

Figure 4-8: Shear strain rate at the cathode ($r = 0.2R$) as a function of Re.

The results from this model are compared to those from the horizontal rotation model to be discussed in the next section.

4.2.2 Horizontal Rotational Flow Model

Another flow model of interest is the flow generated by a rotating cathode around a horizontal axis (see Figure 4-3). It is considered as a two-dimensional model because there is no force acting in the direction parallel to the rotating axis and the rotating cathode width is expected to be much larger than the depth of the fluid below it. Therefore, calculations can be done on cartesian coordinates.

Transport Phenomena Formulations in Cartesian Coordinate

The non-dimensional parameters are slightly different from the vertical rotation case. Here the simulation model is normalized by $(\tilde{x}, \tilde{z}) = \frac{(x,z)}{R_x}, (\tilde{u}, \tilde{w}) = \frac{(u,w)}{(\upsilon/R_x)}$.

Derived in the same way as the equations shown in Section 4.2.1, the dimensionless velocity-vorticity formulation in cartesian coordinates can be written as:

$$0 = \tilde{\nabla}^2\tilde{u} + \frac{\partial\tilde{\omega}}{\partial\tilde{z}}, \tag{4.25}$$

$$0 = \tilde{\nabla}^2\tilde{w} - \frac{\partial\tilde{\omega}}{\partial\tilde{x}}, \tag{4.26}$$

$$0 = \tilde{\nabla}^2\tilde{\omega} - \left(\tilde{u}\frac{\partial\tilde{\omega}}{\partial\tilde{x}} + \tilde{w}\frac{\partial\tilde{\omega}}{\partial\tilde{z}}\right), \tag{4.27}$$

$$0 = \tilde{\nabla}^2\tilde{C}_2 - Sc\left(\tilde{u}\frac{\partial\tilde{C}_2}{\partial\tilde{x}} + \tilde{w}\frac{\partial\tilde{C}_2}{\partial\tilde{z}}\right). \tag{4.28}$$

Boundary Conditions and Initial Conditions

The simulations are carried out on a two-dimensional domain in the $x - z$ plane underneath the rotating cathode. It is noted that our simulations neglect edge effects at the ends of the cathode. Thus, Figure 4-9 illustrates a cross-sectional area of the $x - z$ plane at the middle of y axis, where flows are two dimensional. The dimension of the domain is $X \times H$. The coordinate of cathode center (xc, zc) is not shown on

the figure.

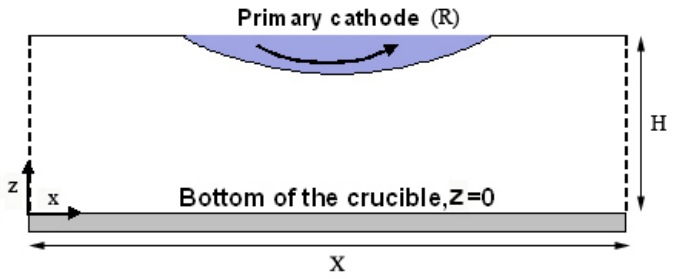

Figure 4-9: Two-dimensional simulation domain for the SOMERC's inner crucible with horizontal rotating cathode.

Boundary conditions are as follows:

at the left and right side of the simulation domain:

$\frac{\partial \tilde{u}}{\partial \tilde{x}} = \frac{\partial \tilde{w}}{\partial \tilde{x}} = \frac{\partial \tilde{\omega}}{\partial \tilde{x}} = \frac{\partial \tilde{C_2}}{\partial \tilde{x}} = 0$ (right), $\tilde{C_2} = 1$ (left),

at the bottom of the crucible: $0 \leq \tilde{x} \leq X/R_x$, $\tilde{z} = 0$

$\tilde{u} = \tilde{w} = \tilde{\omega} = 0$, $\frac{\partial \tilde{C_2}}{\partial \tilde{z}} = 0$,

at the free surface: $\tilde{x} \leq \frac{(0.5X - (R_x^2 - (zc-z)^2))}{R_x}$, $\tilde{z} = H/R_x$

$\frac{\partial \tilde{u}}{\partial \tilde{z}} = \tilde{w} = \tilde{\omega} = 0$, $\frac{\partial C_2}{\partial z} = 0$,

at the cathode region: $\frac{(0.5X - \sqrt{R_x^2 - (zc-z)^2})}{R_x} \leq \tilde{x} \leq \frac{0.5X + \sqrt{(R_x^2 - (zc-z)^2)}}{R}$, $\tilde{z} = H/R$

$\tilde{u} = 0.5\tilde{\Omega}(\tilde{z}c - \tilde{z})$, $\tilde{w} = 0.5\tilde{\Omega}(\tilde{x}c - \tilde{x}), C_2 = 1$,

at the cathode surface: $1 = \frac{(x-xc)^2 + (z-zc)^2}{R^2}$

$\tilde{u} = 0.5\tilde{\Omega}(\tilde{z}c - \tilde{z})$, $\tilde{w} = 0.5\tilde{\Omega}(\tilde{x}c - \tilde{x}), C_2 = 0$.

Symmetric boundary conditions are applied to the side boundaries for velocities and vorticity. On the left, constant inlet flow of C_2 is applied. On the right, symmetric boundary is used. At the bottom of the crucible, no-slip boundary condition and zero flux is applied. On the flat free surface, it is assumed that there is no-shear and no flux in z direction. In the cathode region, velocities and vorticity equal to that of the rotating cathode, whereas C_2 equals to one, representing titanium cathode. Again, at the cathode/electrolyte surface, C_2 is set to zero to indicate the production of magnesium. Table 4.4 lists the physical and characteristic parameters.

All field parameters are set to zero as an initial condition.

Table 4.4: Parameters used in the simulation of horizontal rotating flow

Parameter	Physical value	Characteristic
R	0.2 m	0.2 m
$X \times H$	0.4 m $\times$ 0.05 m	0.2 m
(xc, zc)	(0.2, 0.23)	0.2 m
υ	1.14$\times$ 10^{-6} m^2/s	–

Low Reynolds Number Flow Results

To validate the model, a fluid flow simulation is carried out for low Reynolds number flow (Re=1). With small Re, the flow can be viewed almost as a flow passing around a stationary cylinder. Figure 4-10 presents the contours of the flow fields. The results show that the vorticity profile is symmetric. Velocity in the x direction points from left to right, corresponding to the positive rotation being the counterclockwise direction. Velocity in the z direction directs downward on the left and upward on the right, again following the rotation direction.

SOMERC Fluid and Mass Transport Results

Boundary Layer Thicknesses By coupling the Navier-Stokes equations with the diffusion equation, the fluid dynamics and ion concentration profile in the crucible can be solved. Figure 4-11 shows a representative result of the field contours at $Re = 100$ and $Sc = 5000$. The result shows that the velocity boundary layer thickness observed from vorticity result is thinner on the upwind side (left) and thicker on the downwind side (right) at this $Re > 1$. Similarly, the diffusion boundary layer is thicker on the downwind side. At this high Schmidt number, the diffusion boundary layer is significantly thinner than the viscous boundary layer.

Compared to the results at the same Reynolds number from the previous section, the diffusion boundary layer caused by vertical rotational flow is thinner than

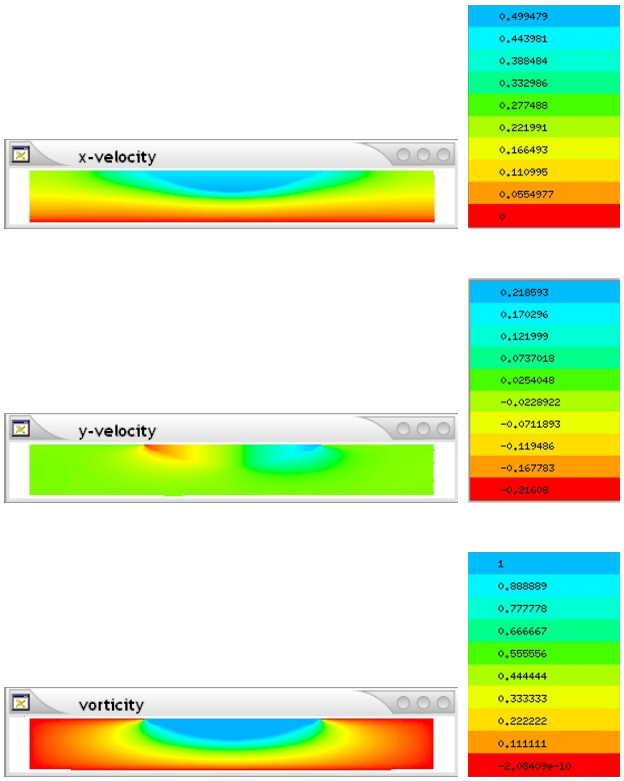

Figure 4-10: Contours of fluid flow produced by horizontal rotating cathode with Re=1.

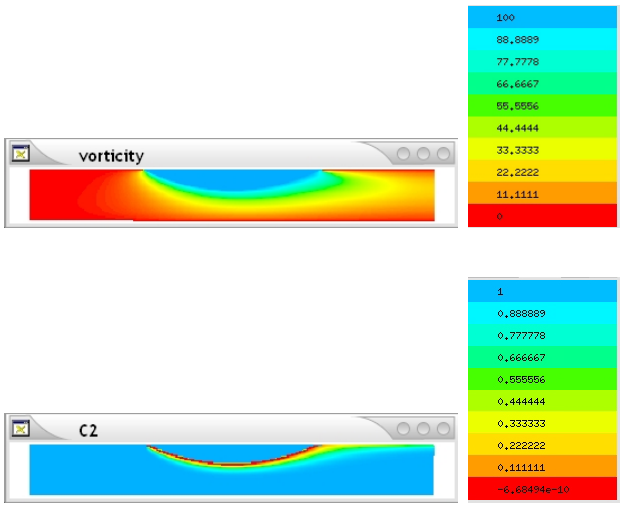

Figure 4-11: Vorticity and C_2 contours produced by horizontal rotating cathode with Re=100 and Sc=5000.

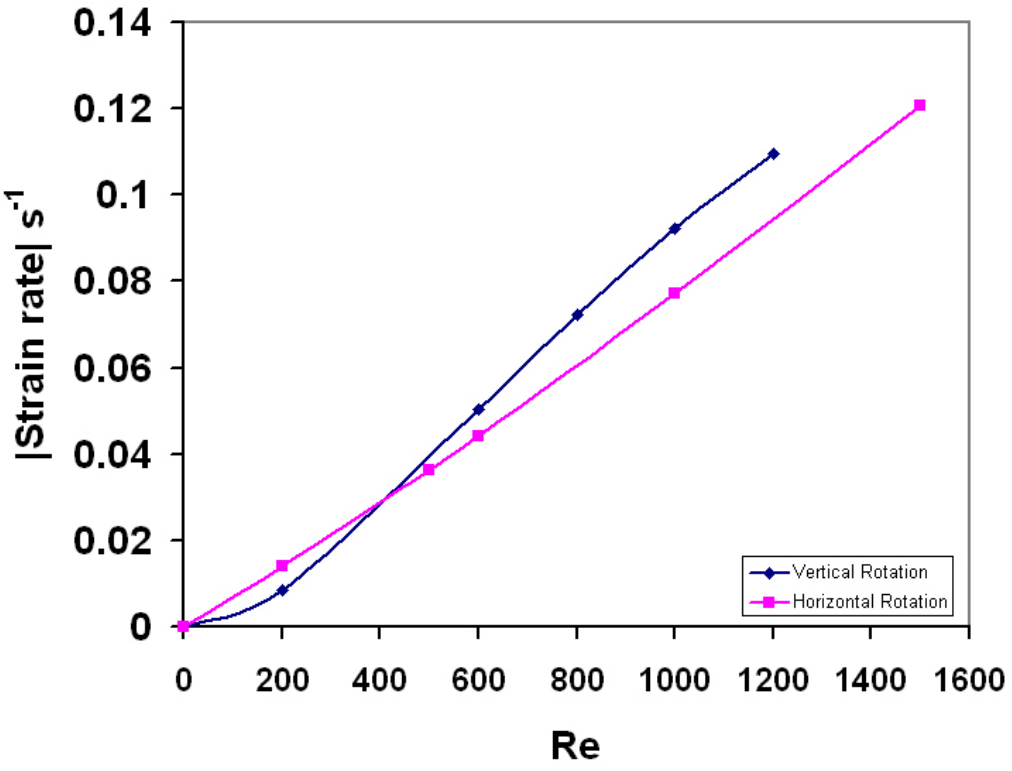

Figure 4-12: Shear strain rate at the mid point underneath the cathode ($x = R_x$) as a function of Re. The shear deformation rate produced by vertical rotation is also shown here again for comparison.

that caused by horizontal rotation. The thinner the concentration boundary layer is advantageous for high deposition rate.

Shear Strain Rate Again, the shear strain rates for different Reynolds numbers are computed and plotted with the results from the vertical rotation. It is noted that the domain dimension are different between these two cases. The height of the domain in horizontal rotation shown here is one fifth of that in the vertical case, whereas the width of the horizontal rotating simulation is twice of that in the vertical rotating model. Shear strain rates turn out to be on the same order of magnitude as depicted in Figure 4-12. Vertical rotation provides a slightly larger deformation rate at these Reynolds number ranges.

Simulations in the range of $Re < 2000$ predict the behaviors of the flow kinematics with presence of diffusing species relatively well. For higher Reynolds number, the

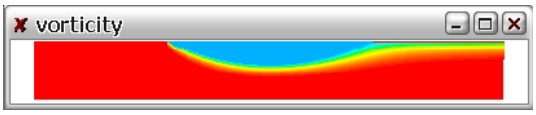

Figure 4-13: Vorticity contours for Re=74800 without mass transfer.

model has some convergence problem when the mass transfer is included. The vorticity contours for higher Reynolds number case (Re=74800) without diffusion coupling is shown in Figure 4-13. It is shown that the momentum boundary layer is extremely thinner as the Reynolds number or the rotational speed increases. In the future, a turbulent flow model may be necessary.

4.3 Phase Field Model of Electrochemical Dendrite Suppression by Cross-Flow

The shear strain rate plots from the preceding macroscopic model are useful for estimating the shear strain rates achievable by these rotation schemes. Microscopically, shear force due to rotational flow can be regarded as shear force due to flow between parallel plates. Thus in the phase field model only a shear force in the x direction is necessary to simulate the shear caused by the cathode rotation. Then the critical shear strain rate $\left|\frac{\partial u}{\partial z}\right|_{crit}$ for different electrolyte compositions can be determined from the stability plot. Finally, the corresponding Reynolds number estimated from the shear strain rate plot Figure 4-12 yields the required rotational speed, $\Omega = \frac{\upsilon Re_{crit}}{R^2}$.

Future phase field model will be focused on the cathode evolution under shear flow. This phase field model represents the solid-liquid interface in the SOMERC process. The current phase field model for ternary system can be used. The key strategies are to stop the flow as it enters solid phase and to introduce a shear flow in the x direction. To model a solid-liquid interface, two methods are suggested for future investigation.

Approach 1: Interfacial Stress Term in Velocity-Pressure Function At a solid-liquid interface, the dissipative interfacial stress must be considered. This

dissipative interfacial stress term has been approximated by Beckermann *et al.* [57] in phase field modeling of solidification. Analogous to the friction term in flow through porous media [58], this term is proportional to the kinematic viscosity (υ), velocity ($\overrightarrow{U}$), and solid phase (C) as follows:

$$F_{solid-liquid} = -\frac{h\upsilon\overrightarrow{U}}{\varepsilon^2}C^2(1-C), \tag{4.29}$$

where h is a constant and ε is the interface thickness. The proportionality constant, h, can be viewed as the friction coefficient and approximated by asymptotic analysis. For Couette flow, a value of 2.757 [57] leads to an extrapolated velocity of zero at the $C = 0.5$ contour.

In a ternary system, phase fraction is written as C_2 and C_3. We adjust the function accordingly to make the drag term vanish in the liquid and solid. Within the diffuse interface, the dissipative interfacial term reduces the velocity to zero toward the solid phase. In addition, a uniform force, F_{max}, in the x direction is added to the liquid phase. Finally, the velocity-pressure Navier-Stokes equations can be expressed as:

$$\begin{aligned}
\tfrac{\partial u}{\partial t} + u\tfrac{\partial u}{\partial x} + v\tfrac{\partial u}{\partial y} &= -\tfrac{1}{\rho}\nabla P_x + \nu\nabla^2 u - \tfrac{2.757\nu u}{\varepsilon^2}C_2^2C_3^2(1-C_3) + F_{max}(1-C_3) \\
\tfrac{\partial v}{\partial t} + u\tfrac{\partial v}{\partial x} + v\tfrac{\partial v}{\partial y} &= -\tfrac{1}{\rho}\nabla P_y + \nu\nabla^2 v - \tfrac{2.757\nu v}{\varepsilon^2}C_2^2C_3^2(1-C_3) \\
\tfrac{\partial u}{\partial x} + \tfrac{\partial v}{\partial y} &= 0.
\end{aligned} \tag{4.30}$$

With this approach, the velocity falls to zero over a distance of 6ε.

Approach 2: Variable Viscosity A more simple idea is to vary the viscosity to treat the solid as if it were a very viscous fluid. This has been applied to the phase-field model of solidification with convection by Anderson *et al.* [59]. In their model, velocity-pressure formulation was used for the Navier-Stokes equation. For our model, we choose to work with the velocity-vorticity function which is more robust. The kinematic viscosity function can be written as:

$$\eta = \eta_{XF_2}(1-C_3) + \eta_{Mg}C_3(1-C_2) + \eta_{Ti}C_2C_3 \tag{4.31}$$

Thus viscosity is equal to liquid viscosity in the electrolyte ($C_3 = 0$) and to solid viscosity in the solid metal ($C_3 = 1$). The viscosity ratio between solid and liquid is chosen to be $\eta_s/\eta_l \geq 500$ as used by Anderson *et al.* [59] as these values result in velocity approximately equal to zero in the solid phase. Next, the uniform force term is added to create shear flow. In this case, the curl of shear force per unit volume ($\nabla \times (F_{max}(1-C_3))$) replaces the curvature body force term in the vorticity equation 2.25. Thus the momentum equation with variable viscosity is:

$$\frac{\partial \widetilde{\omega}}{\partial \widetilde{t}} + \overrightarrow{u} \cdot \widetilde{\nabla}\widetilde{\omega} = Sc\widetilde{\nabla}^2\widetilde{\omega} + \widetilde{\omega}\nabla^2\widetilde{\eta} + \frac{\partial^2\widetilde{\eta}}{\partial\widetilde{x}\partial\widetilde{y}}\left(\frac{\partial\widetilde{v}}{\partial\widetilde{y}} - \frac{\partial\widetilde{u}}{\partial\widetilde{x}}\right) + F_s\tilde{F}_{max}\tilde{\nabla} \times (1 - C_3), \quad (4.32)$$

where $\tilde{\eta} = \frac{\eta}{\rho D}$ and $F_s = \frac{F_{max}\lambda^3}{\rho D^2}$.

The main advantages of this method are the ability to handle any system with concentration-dependent viscosity and the change from liquid to solid across the diffuse interface as ε rather than the 6ε distance required for the interfacial stress treatment.

Figure 4-14 shows the schematic drawing of the velocity profile across the interface.

Stability Criteria The solid-liquid system can be parameterized using the Peclet numbers of the interface and the liquid. These Peclet numbers are expressed as:

$$\begin{aligned} Pe_{int} &= \frac{u_{int}\lambda}{D} \\ Pe_{liq} &= \frac{|\frac{\partial u}{\partial z}|\lambda^2}{D} \end{aligned} \quad (4.33)$$

The Peclet number of the interface is a function of the interface growth velocity as in Chapter 2 and 3, whereas the Peclet number of the liquid is a a function of the strain rate caused by the shear flow. It is expected that shear flow across the dendrites should decrease the concentration boundary layer thickness, thus more titanium deposition will occur on the upwind side. Consequently, the interface would shifted in the x direction due to shear, competing with the growth in the z-direction due to electric field. The critical Peclet number for different values of the applied field and electrolyte composition will be determined using this model.

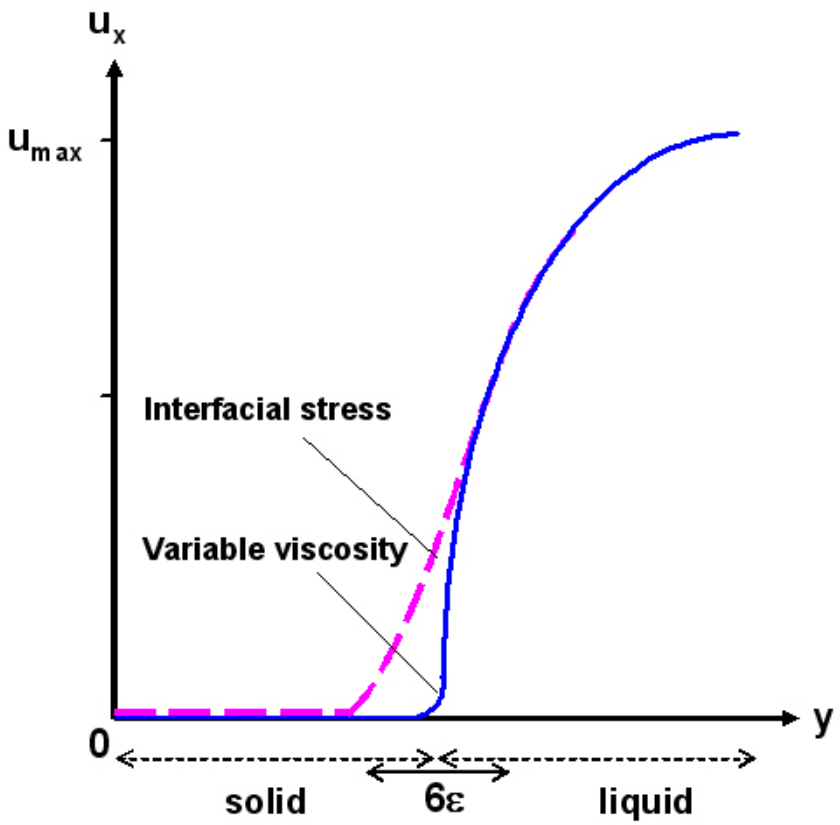

Figure 4-14: Schematic velocity plot across the solid-liquid interface. The interfacial stress method captures the diffuse interface with 6ε thick region. The variable viscosity method approaches the sharp interface model.

4.4 Summary

Macroscopic transport phenomena in the SOMERC process was simulated by solving the velocity-vorticity form of the Navier-Stokes equations and ion transport equation. The vertical rotating cathode results were verified by using Czochralski results in the literature. Our model overestimates the maximum velocity, especially for high Gr number case. For the SOMERC process, natural convection is not dominant, thus this model can be applied without coupling with heat conduction.

After incorporating ion diffusion, we explored the effect of rotational flow on the viscous and diffusion boundary layer thicknesses, and the shear strain rate at the cathode. The ratio of boundary layer thicknesses follows the boundary layer theory ($\frac{\delta_c}{\delta_u} = 22Sc^{-1/3}$). And the shear strain rate increases with Reynolds number (rotation

speed).

The horizontal rotating cathode model reproduced correct low Reynolds number flow behavior. As expected, the results at higher rotation rate show more non-uniform boundary layer thicknesses compared to the vertical rotational case: on the upwind side, the boundary layers are thinner than the downwind side. The diffusion boundary layer thickness from this case is significantly thicker than that from vertical rotation case.

Experimentalists can use these flow models to estimate the appropriate rotation rate for producing the critical shear strain rate for dendrite suppression, which can be determined using the solid-liquid phase field model outlined here.

Chapter 5

Concluding Remarks and Future Work

This chapter summarizes the major contributions of this thesis and recommendations for further development.

5.1 Contributions

The phase field method, a diffuse interface model based on thermodynamic of the system, is modified to model transport-limited electrolytic processes. The mass transport mechanisms in the electrolytic processes (diffusion, electromigration, and convection) are explored to illustrate their roles in morphological instability on the cathode. The present phase field model can represent complex topology evolution in the regime much more effectively than that of Guyer *et al.* [20], and more completely than the previous models or linear stability analysis.

The rapid charge redistribution assumption is valid in high-temperature electrochemical reaction such as the electrolytic smelting processes and other molten salt processes where field changes more slowly than the charge transfer timescale, 10^{-12} seconds [25]. Because of this mass transfer limitation, the double layer for charge is not required in this model. As a result, our model is the first phase field model for electrochemistry that demonstrates the morphological contours at high resolution on

two and three dimensional domains.

For an unsupported electrolyte system, we apply this model to the Electric-Field Enhanced Smelting and Refining Process (EFESR). Stability maps are plotted and compared to the sharp interface model. As expected, the cathode stabilization at interface is more stable at low current density, high surface tension, low electrode/electrolyte conductivity ratio, and low viscosity, though small electrode separation requires further explanation. In the comparison with the experimental observation in the EFESR, our model gives a good prediction of the critical perturbation wavelength.

In addition to the EFESR process for iron, this model can be applied to magnesium or aluminum reduction, both of which are two-phase liquid-liquid systems with transport-limited electrochemical reactions. This phase field model can serve as a tool to study cathode shape and topology evolution: for magnesium, this would help to innovate an efficient cathode design; for aluminum, it could help to determine conditions for suppression of harmful streamers.

For a supported electrolyte system, the phase field model is developed and applied to the electrolytic extraction of titanium without convection. The model results represent the topological evolution of the cathode at high resolution and display the concentration gradient in the electrolyte. Based on the plot of critical Peclet number generated by our phase field model, the interface is more unstable for high spectator ion concentration and more stable for low spectator ion concentration, under the critical Peclet number. Above this value, the interface is always unstable at any spectator ion concentration. The results agree with the linear stability analysis.

The ternary phase field model is also applied to the Subhalide Reduction Process, which also satisfies the transport-limited and rapid charge redistribution assumptions. The results demonstrate that our present phase field model can capture the titanium formation mechanisms in this system. In this Subhalide reduction Process, magnesiothermic reduction and electronically mediated reaction (EMR) are the main pathways for titanium formation. EMR occurs whenever there is a close circuit configuration in the system such that electrons can transfer from the anode to the cathode via

conduction in the metal phases. The phase field model illustrates this phenomenon through the presence of an electrical potential gradient across the metal phases.

Transport phenomena models for vertical and horizontal rotating flows are constructed to investigate flow near the rotating cathode in Solid-Oxide Membrane Electrolysis with Rotating Cathode (SOMERC). The two rotational flow models reveal flow contours showing the diffusion boundary and momentum boundary layer thicknesses, which are important for cathode design. The shear strain rates at different rotation speeds are calculated. These models are useful for the experimentalists to estimate the cathode rotation speed that is sufficient to help stabilize the cathode deposits.

5.2 Limitations and Recommendations for Future Work

The electrochemical reaction in this model is in the mass transport limited regime. Under this condition, the mass transfer resistance is much greater than the charge transfer resistance. As a result, cations recombine with electrons as soon as the ions arrive at the cathode interface. At high temperature such as in metal smelting processes, the mass transport limited condition is valid. However low temperature process such as aqueous electrolysis are in the charge transfer limited or mixed limitation regimes. Accumulation of cations in front of the cathode leads to a non-ohmic voltage drop across the interface, which can not be captured by this model.

This phase field model can simulate solid-solid and liquid-liquid interfaces as discussed in this thesis. Further investigations for solid-liquid and multi-phase (solid/liquid/gas) systems are necessary to better represent the physical features of any processes. In particular, the phase field model for solid-liquid case will be very useful for SOMERC process in order to develop the stability criteria of the solid interface under shear. As discussed in Section 4.3, two approaches are suggested for such a model: interfacial stress and variable viscosity. In addition, the mixed stress method of Powell

and Dussault [60] can also be employed to account for the solid structure interaction. Solids also introduce complexity associated with anisotropy, leading to crystal faceting or proffered directions for dendrite growth. Modeling such systems will require keeping track of crystal orientation, such as the models of Warren *et al.* [61]. A model incorporating these effects would be a powerful tool for efficiently predicting polycrystalline microstructure produced by transport-limited electrolysis process.

Moreover, the transport of chemical species is assumed to be independent of temperature. Scaling analysis is required to confirm that the thermal gradient has no significant effect on mass and charge transports for the isothermal model here to be valid. Alternatively, a heat conduction model could be coupled with this model to capture this effect: with high electrical current and high electrical resistivity. Joule heating needs to be taken into account as another heat source for such a model.

Some of the transport-limited systems exhibit significant electrocapillarity effects where interfacial energy is a fraction of the perpendicular component of electric field. This phenomenon can be captured by a straightforward extension of the present model without double layer discretization, by making the interfacial energy (determined by free energy of mixing β and gradient penalty coefficient α in the binary case) depend on the dot product of electric field and composition gradient:

$$\gamma = f(\nabla\Phi \cdot \nabla C) \, or \, f(\nabla\Phi \cdot \nabla C_3) \tag{5.1}$$

Finally, the transport model of the SOMERC process should be extended in several ways. Design features of that process such as the flow barrier and scrap feed should be studied using additional models. A 3D model of transport in the outer crucible might also determine whether the process can be self-heating.

In conclusion, the phase field model can be extended to represent more complex multi-component systems with electrocapillarity or solid-liquid interaction. The interfacial double layer need not be modeled to use this approach for many applications satisfying the assumptions of transport-limited operation and rapid charge redistribution. These enhancements should make this phase field method a valuable tool

for designing many electrolysis processes, such as those outlined here for titanium production.

Appendix A

List of Symbols

a	constant in the anodic potential term
A	perturbation amplitude, m
α	phase field gradient penalty coefficient, J/m
β	homogeneous free energy coefficient, J/m^3
β_T	thermal expansion coefficent, 1/K
$\mathcal{B}$	electromigration constant
c	molar concentration, mol/m^3
C	dimensionless concentration
D	diffusivity, m^2/s
δ	boundary layer thickness, m
ε	interface thickness, m
ϵ	permittivity
η	viscosity, Pa$\cdot$ s
F	Faraday's constant, 96480 C/mol
F_s	dimensionless force parameter
$\mathcal{F}$	free energy functional
Gr	Grashof number
γ	interfacial energy, J/m^2
H	crucible height, m

J	flux, mol/m^{2}s, m/s for dimensionless C
K_{ii}	gradient energy penalty coefficient for ternary, J/m
κ	mobility, m^5/J·s
L	separation between electrodes, m
L_{diff}	diffusion length scale, m
λ	domain width, perturbation wavelength, m
M_{ij}	mobility, m^5/J·s
μ	chemical potential, J/m^3
N	force parameter
ω	vorticity, s^{-2}
Ω	rotational speed, rad/s
Pe	Peclet number
Φ	electrical potential, J/C
Pr	Prandlt number
Ψ	homogeneous free energy, J/m^3
R	gas constant, J/mol K, crucible radius, m
R_x	cathode radius, m
ρ_f	charge density, C/m^3
$\frac{\rho}{M}, \rho_M$	molar density, mol/m^3
Sc	Schmidt number
σ	ionic conductivity, Ω^{-1}m^{-1}
σ_e	electronic conductivity, Ω^{-1}m^{-1}
σ_{eff}	effective conductivity, Ω^{-1}m^{-1}
t	time, s
T	temperature, K
τ	shear stress, N/m^2
$\overrightarrow{U}$	velocity vector, m/s
V	volume, m^3
X	mole fraction
z	number of electrons transferred per mole, mol e$^-$/mol

Appendix B

RheoPlast

The phase-field model software used in this thesis is named RheoPlast: Phase Field Multi-Physic Code. It has been developed by Powell research group [28]. RheoPlast 0.5 has been released in 2004 as a free open-source software under the terms of GNU General Public Software. RheoPlast is consisted of several flexible modules each of which includes specific physics required in the phase field calculation. Currently, RheoPlast allows users to choose the phase field free energy functions: binary and ternary metal or polymer systems, the transport coupling terms: momentum and heat flow, the fluid-structure interaction, the crystal orientation, and the electrochemical reactions. In addition, system specific features are implemented such as functional initial and boundary conditions, variable mobility and variable viscosity. Thus, it is applicable to various systems ranging from solidification of moving solid in fluid flow [62], to polymer membrane structure formation [63], to cathode/electrolyte interface evolution in transport-limited electrolytic processes as shown in this thesis.

B.1 Numerical Solvers

RheoPlast package is coded in C language. Semi-implicit timestepping method is used for the time-dependent functions. There are also constraint equations (i.e., continuity equations and Poisson's equation). Our timestepping algorithm is able to handle mixed constraint equations simultaneously. The non-linear equations are solved by

SNES solver in PETSc (Portable, Extensible Toolkit for Scientific Computation) [64]. PETSc is a powerful scientific computation library developed by Argonne National Laboratories, which handles distributed storage of the discretized field variables, vectors and matrices, and distributed solution of the resulting system of nonlinear equations. In PETSc, parallel computing is conveniently utilized through MPI (Message Passing Interface).

B.2 Visualization

Illuminator [65], also developed by the Powell research group, is a distributed visualization library that enables rapid saving and loading data on Beowulf cluster (scalable cluster). Solution data from the simulation can be saved at every n timesteps specified by users through the command line. Time series data from multiple processors or a single processor can then be viewed on Geomview in 2D or 3D via tsview or tsview-ng which are parts of Illuminator package. The binary system results and are from tsview. The ternary system results are from tsview-ng that has more detail color map representing multiple phases.

B.3 Automatic Analysis Tools

Two programs are implemented as add-on tools to RheoPlast for automatic analyses. The first program called poster is for determining the interface growth rate. The second program called secant allows continuous runs of RheoPlast and poster until the critical point (surface tension or electric field) is reached based on secant method.

Interface Growth Rate Calculation (poster.c)

For sinusoidal perturbation simulations, this program calculates the change in the amplitudes over time. The cathode/electrolyte interface is defined by $C = 0.5$ (C_3 for ternary case). The program tracks for the maximum and minimum points where C>0.5. Then these locations are approximated to the point where C=0.5 by linear

interpolation. After maximum and minimum points are obtained, the final data and the tenth previous data are analyzed.
The change in amplitude for n data points is:

$$\frac{dA}{dt} = \frac{(A_n^{max} - A_n^{min}) - (A_{n-10}^{max} - A_{n-10}^{min})}{t_n - t_{n-10}} \tag{B.1}$$

This program can also be modified to suit any computational purpose such as calculating the interface velocity of a flat interface.

Critical Point Evaluation (secant.c)

On the stability plots, we can change either the surface tension (γ) or the applied electric field ($\frac{\triangle\Phi}{\triangle y}$). For each point on the plots (Figure 2-8 and 2-10), the simulations are carried out as follows:

1. Run RheoPlast with γ or Φ for time t
2. Run poster to determine $\frac{dA}{dt}$
3. If $\frac{dA}{dt} > 0$, the interface is unstable: γ=$\gamma + \triangle\gamma$ or Φ=$\Phi - \triangle\Phi$.
   if $\frac{dA}{dt} < 0$, the interface is stable: γ=$\gamma - \triangle\gamma$ or Φ=$\Phi + \triangle\Phi$.
4. Repeat 1-3 until $\frac{dA}{dt} < 10^{-4}$

An add-on program is coded to run RheoPlast and poster automatically, as well as to determine the next input for γ or Φ by secant method. The basic secant method is:

$$x_n = x_{n-1} - \frac{f(x_{n-1})(x_{n-1} - x_{n-2})}{f(x_{n-1}) - f(x_{n-2})} \tag{B.2}$$

where $f(x)$ is $\frac{dA}{dt}$ and x is γ or Φ.

Bibliography

[1] R. Selim and P. Bro. Rechargeable lithium electrodes in a propylene carbonate electrolyte. *J. Electrochem. Soc.*, 121:1457–1459, 1974.

[2] I. Epelboin. *J. Electrochem. Soc.*, 127:2100–2104, 1980.

[3] C. Brissot, M. Rosso, J.-N. Chazalviel, and S. Lascaud. In Situ concentration cartography in the neighborhood of dendrite growing in lithium/polymer-electrolyte/lithium cells. *J. Electrochem. Soc.*, 146:4393–4400, 1999.

[4] P. P. Trigueros, F. Saques, and J. Claret. Influence of an inert electrolyte on the morphology of quasi-two- dimensional electrodeposits. *Phys. Rev. E.*, 49(5):4328–4340, 1994.

[5] U. B. Pal, S. A. MacDonald, D. W. Woolley, and A. C. Powell. Results demonstrating techniques for enhancing electrochemical reactions involving iron oxide in slags and C in liquid iron. *Metall. Mater. Trans. B.*, 36B:209–218, 2005.

[6] W. W. Mullins and R. F. Sekerka. Morphological stability of a partical growing by diffusion heat flow. *J. Appl. Phys.*, 34:323, 1963.

[7] J.-N. Chazalviel. Electrochemical aspects of the generation of ramified mettalic electrodeposits. *Phys. Rev. A.*, 42(12):7355–7367, 1990.

[8] R. Aogaki, K. Kitazawa, Y. Kose, and K. Fukei. Theory of powdered crystal formation in electrocrystallization-occurence of morphological instability at the electrode surface. *Electrochim Acta*, 25:965–972, 1980.

[9] R. Cuerno and M. Castro. Transient due to instabilities hinder Kardar-Parisi-Zhang scaling: A unified derivation for surface growth by electrochemical and chemical vapor deposition. *Phys. Rev. Lett.*, 87(236103), 2001.

[10] M. Haataja, D. J. Srolovitz, and A. B. Bocarsly. Morphological stability during electrodeposition: I. Steady states and stability analysis. *J. Electrochem. Soc.*, 150:C699–C707, 2003.

[11] U. Landau. EPRI Report EM-2393, 1982.

[12] J. Elezgaray, C. Leger, and F. Argoul. Three-additive model of superfilling of copper. *J. Electrochem. Soc.*, 145:2016–2024, 1998.

[13] C. P. Chen and J. Jorne. The dynamics of morphological instability during electrodeposition. *J. Electrochem. Soc.*, 138:3305–3302, 1991.

[14] Y. Cao, P. Taephaisitphongse, R. Chalupa, and A. C. West. Linear stability analysis of unsteady galvanostatic electrodeposition in the two-dimensional diffusion-limited regime. *J. Electrochem. Soc.*, 148:C466–C472, 2001.

[15] M. Martin. Materials in thermodynamic potential gradients. *Pure Appl. Chem.*, 75:889–903, 2003.

[16] T. J. Pricer, M. J. Kushner, and R. C. Alkire. Monte-Carlo simulation of the electrodeposition of copper. *J. Electrochem. Soc.*, 149:406–412, 2002.

[17] S. Osher and J. A. Sethian. Fronts propagating with curvature-dependent speed: Algorithms based on Hamilton-Jacobi formulations. *J. Comput. Phys.*, 79:12–19, 1988.

[18] D. Wheeler, D. Josell, and T. P. Moffat. Modeling superconformal electrodeposition using the Level Set Method. *J. Electrochem. Soc.*, 150:C302–C310, 2003.

[19] D. Wheeler, D. Josell, and T. P. Moffat. Influence of catalytic surfactant of roughness evolution during film growth. *J. Electrochem. Soc.*, 151:C538–C544, 2004.

[20] J. E. Guyer, W. J. Boettinger, J. A. Warren, and G. B. McFadden. Phase field modeling of electrochemistry. II. Kinetics. *Phys. Rev. E.*, 69(021604), 2004.

[21] D. Dussault and A. C. Powell. Phase field modeling of electrolysis in a slag or molten salt. In *Proc. Mills Symp.*, pages 359–371. The Institute of Materials, London, UK, August 2002.

[22] D. Jacqmin. Calculation of two-phase Navier-Stokes flows using phase-field modeling. *J. Comput. Phys.*, 155(1):96–121, 1999.

[23] T. H. Okabe and O. Takeda. A new high speed titanium production by subhalide reduction process. In *Proc. Light Metals, San Francisco, CA, TMS Annual Meeting*, pages 1139–1144. TMS, March 2005.

[24] M. Suput, R. DeLucas, S. Pati, G. Ye, U. Pal, and A. C. Powell. Solid oxide membrane (SOM) technology for environmentally sound production of titanium. In *Sohn Symposium, San Diego, CA*. TMS. to appear in Aug 2006.

[25] D. Dussault. A diffuse interface model of transport limited electrochemistry in two-phase fluid systems with application to steelmaking. Mechanical engineering s.m. thesis, Massachusetts Institute of Technology, January 2002.

[26] Adam C. Powell and David Dussault. Detailed mathematical modeling of liquid metal streamer formation and breakup. In *Metallurgical and Materials Processing Principles and Technologies (Yazawa International Symposium)–Vol. 3: Aqueous and Electrochemical Processing*, pages 235–250, San Diego, March 2003. TMS.

[27] J. E. Guyer, W. J. Boettinger, J. A. Warren, and G. B. McFadden. Phase field modeling of electrochemistry. I. Equilibrium. *Phys. Rev. E.*, 69(021603), 2004.

[28] A. C. Powell, D. Dussault, B. Zhou, J. Vieyra, and W. Pongsaksawad. RheoPlast: Marrying phase field and fluid-structure interactions, 2004. `http://lyre.mit.edu/~powell/rheoplast.html`.

[29] M.-O. Bernard, M. Plapp, and J.-F. Gouyet. A mean-field kinetic lattice gas model of electrochemical cells. *Phys. Rev. E*, 68(011604), 2003.

[30] D. P. Barkey, R. H. Muller, and C. W. Tobias. Roughness development in metal electrodeposition: II. Stability theory. *J. Electrochem. Soc.*, 136:2207–2214, 1989.

[31] G. Urbain and M. Boiret. *Ironmaking and steelmaking*. National Institute of Standards and Technology, 1990.

[32] Y. Li, J. A. Lucas, R. J. Fruehan, and G. R. Belton. The chemical diffusivity of oxygen in liquid iron oxide and a calcium ferrite. *Metall. Mater. Trans. B.*, 31B:1059–1068, 2000.

[33] K. C. Mills and B. J. Keene. Physical properties of BOS slags. *Int. Mater. Rev.*, 32:1–120, 1987.

[34] W. J. Kroll. The production of ductile titanium. *Trans. Met. Soc. AIME*, 215:546–553, 1959.

[35] B. E. Hurless and F. H. Froes. Lowering the cost of titanium, 2001.

[36] G. Z. Chen, D. J. Fray, and T. W. Farthing. Direct electrochemical reduction of titanium dioxide to titanium in molten calcium chloride. *Nature*, 407:361–364, 2000.

[37] J. C. Withers and R. O. Loutfy. A new novel electrolytic process to produce titanium, 2003. The 19th Annual Titanium Conference of the International Titanium Association, Monterey, CA.

[38] M. Ginatta. Process for the electrolysis production of metals. No. 6,074,545.

[39] K. Ono and R. Suzuki. A new concept for producing Ti sponge: Calciothermic reduction. *JOM*, 54(2):59–61, 2002.

[40] K. Dring, R. Dashwood, and D. Inman. Predominance diagrams for electrochemical reduction of titanium oxides in molten $CaCl_2$. *J. Electrochem. Soc.*, 152:D184–D190, 2005.

[41] P. Kar and J. W. Evan. Mathemathical modeling of the reduction of pallets of titanium dioxide during the FFC process, MS&T Meeting 2005, Pittsburgh, PA.

[42] E. Kraft. Summary of emerging low cost titanium technologies. Technical report, US Department of Enery and Oak Ridge National Laboratory, EHKT Technologies 10917 SE Burlington Dr., Vancouver, WA 98664, January 2004.

[43] T. H. Okabe and D. R. Sadoway. Metallothermic reduction as an electronically mediated reaction. *J. Mater. Res.*, 13(12):3372–3377, 1998.

[44] T. Uda, T. H. Okabe, Y. Waseda, and K. T. Jacob. Contactless electrochemical reduction of titanium (II) chloride by aluminum. *Metall. Mater. Trans. B.*, 31B:713–721, 2000.

[45] D. E. Woolley, U. B. Pal, and G. B. Kenney. SOM technology for direct reduction of magnesium from its oxide. In *Proc. Symp. Magnesium, Nashville, TN, TMS Annual Meeting*, page 405. TMS, March 2000.

[46] U.B. Pal. Private communication. September 2002.

[47] S. Yuan, U. B. Pal, and K. C. Chou. Modeling scalup of galvanic deoxidation of molten metals using solid electrolyte cells. *J. American Ceramic Society*, 79(3):641–650, 1996.

[48] M. Flemings. Behavior of metal alloys in the semisolid state. *Metall. Mater. Trans. B.*, 22B:269–293, 1991.

[49] I. Mogi and M. Kamiko. Suppression of growth instability in electropolymerization of pyrrole. *Bull. Chem. Soc. Jpn.*, 69:1889–1892, 1996.

[50] D. Xu, C. Shu, and B. C. Khoo. Numerical simulation of flows in Czchralski crystal growth by second order upwind QUICK scheme. *J. Cryst. Growth*, 173(1):123–131, 1997.

[51] C. Shu, Y. T. Chew, and Y. Liu. An efficient approach for numerical simulation of flows in Czhchralski crystal growth. *J. Cryst. Growth*, 181(1):427–436, 1997.

[52] A. Lipchin and R. A Brown. Comparison of three turbulence models for simulation of melt convection in Czchralski crystal growth of silicon. *J. Cryst. Growth*, 205(1):71–91, 1999.

[53] A. A. Wheeler. Four test problems for the numerical simulation of flow in Czochralski crystal growth. *J. Crystal Growth*, 102:691–695, 1990.

[54] M. K. Ermakov. CFD software COMGA COnvection in MicroGravity and Applications: The analysis of hydrodynamics, heat and mass transfer problems. `http://www.ipmnet.ru/~ermakov/comga/crystal_growth_e.php`.

[55] G. J. Janz. *Molten Salts Handbook*. Academic Press, NY, 1967.

[56] G. J. Janz and R. P. T Tomkins. *J. Phys. Chem. Ref. Data*, 12, 1983.

[57] C. Beckermann, H.-J. Diepers, I. Steinbach, A. Karma, and X. Tong. Modeling melt convection in phase-field simulations of solidification. *J. Comp. Phys.*, 154:468–496, 1999.

[58] C. Beckermann and J. Ni. A volume-averaged two-phase model for transport phenomena during solidification. *Metall. Trans. B.*, 22:349–361, 1991.

[59] D. M. Anderson, G. B. McFadden, and A. A.Wheeler. A phase-field model of solidification with convection. *Physica D.*, 135, 2000.

[60] A. C. Powell and D. Dussault. Floating solids: Combining phase field and fluid-structure interactions. *Appl. Numer. Anal. Comp. Math*, 2:157–166, 2005.

[61] J. A. Warren, R. Kobayashi, A. E. Lobkovsky, and W. C. Carter. Extending phase field models of solidification to polycrystalline materials. *Acta. Metall.*, 51:6035–6058, 2003.

[62] J. Vieyra. Phase-field simulation of solidification with moving solids. Materials science and engineering s.m. thesis, Massachusetts Institute of Technology, May 2005.

[63] B. Zhou and A. C. Powell. Phase field simulations of early stage structure formation during immersion precipitation of polymeric membranes in 2D and 3D. *J. Membr. Sci.*, 268(2), 2006.

[64] S. Balay, K. Buschelman, W. D. Gropp, D. Kaushik, M. G. Knepley, L. C.McInnes, B. F. Smith, and H. Zhang. PETSc Web page, 2001. `http://www.mcs.anl.gov/petsc`.

[65] A. C. Powell, B. Zhou, J. Vieyra, W. Pongsaksawad, and O. Ocholi. Illuminator, 2006. `http://lyre.mit.edu/~powell/illuminator.html`.